A Study of Earthquake Source Characteristics from High-Frequency Strong Ground Motions(Dissertation_全文)

AUTHOR(S):

Iwata, Tomotaka

学位申請論文

岩田知孝

A Study of

Earthquake Source Characteristics

from High-Frequency Strong Ground Motions

Tomotaka Iwata

ACKNOWLEDGMENTS

This study was performed under the direction of Dr. Soji Yoshikawa, Professor Emeritus of Kyoto University and under the supervision of Dr. Kojiro Irikura, Professor of Kyoto University. The author wishes to express his gratitude to Professor Soji Yoshikawa for his encouragement, and Professor Kojiro Irikura for his valuable help and discussions throughout this investigation. The author is indebted to Dr. Yoshimasa Kobayashi of Kyoto University, Dr. Masanori Horike of Osaka Institute of Technology, Mr. Eiichi Fukuyama of the National Research Center for Disaster Prevention and other colleagues for their discussions and encouragements during the preparation of this dissertation.

The author is grateful to Dr. Ikuei Muramatu of Gifu University, Drs. Akio Kuroiso and Yoshihisa Iio of Kyoto University, Dr. Tamao Sato of Hirosaki University, Dr. Kazuyoshi Kudo of the Earthquake Research Institute of the University of Tokyo, Dr. Hajime Tsuchida of the Port and Harbour Research Institute, and Drs. Yoshihiro Sawada and Katsuhiko Ishida of the Central Research Institute of the Electric Power Industry for providing the seismic records. Sincere thanks are also expressed for cooperation in our observations to Mrs. Shigeru Kasuga, Toshiaki Yokoi, Eiichi Fukuyama and Hirohito Ohnuma.

Profs. Takeshi Mikumo, Yoshimasa Kobayashi, and Junpei Akamatsu kindly read the manuscript and greatly aided in revision of the manuscript. Dr. B. Geller of the Earthquake Research Institute of the University of Tokyo also sincerely reviewed of a part of this manuscript.

Abstract

The generations of high-frequency (> 1 Hz) strong ground motions from earthquakes are extremely important for seismology and engineering seismology. In this study, though propagation path effects of seismic waves (such as intrinsic and/or scattering attenuation, reflection or refraction), and local site effects (such as site effects of surface geology on ground motion and non-linear responses) play important roles in generating high-frequency strong motions, we focus mainly on source effects. Gross studies have been suggesting that high-frequency ground motions may be induced by the heterogeneities of the rupture, for example, spatial variation of stress drop (asperity model) or an irregular rupture velocity on the fault (barrier model). Therefore, to determine source characteristics in the high-frequency range is important for examining the aspects of earthquake rupture in short space-and-time scales. The similarity between source characteristics of small events and those of large events is also important to study the physics of earthquake sources and to predict strong ground motions, because source characteristics of small events may represent local heterogeneity of faulting during large earthquakes.

We developed a methodology to estimate source characteristics in connection with high-frequency strong ground motions. In Chapter 1, the source parameters of the mainshock and the aftershocks of the 1983 Japan Sea earthquake $M_{JMA}7.7$ are determined by using seismic records obtained at stations with the hypocentral distances from 70 to 250km. First, we attempt to

separate the source spectra, the propagation-path effect, and the local site effect by applying a linear inversion method to the logarithms of the observed spectra. Using the propagation path and local site effects determined by the inversion, we can estimate the source spectra of events which are recorded at even a single station, by removing the propagation-path and site effects from the observed spectra. Next, we estimate the source parameters and examine the relation between those parameters. Also we test the applicability of the ω^{-2} model expected from a simple crack model to the source spectra with two methods, the first of which is comparing the dynamic stress drop to the static stress drop, and the second of which is comparing the seismic moment and the corner frequency determined from Andrews' automated objective method based on the ω^{-2} model to those from the hand-reading method. Most of the events obey the ω^{-2} model, but several events with seismic moment greater than 3×10^{22} dyn*cm, especially the largest aftershock (M=7.1) and the aftershock with M=6.0, cannot be explained by the ω^{-2} model, but should be explained by complex source models such as the multi-crack model or the asperity model, because the dynamic stress drop of these earthquakes is larger than the static stress drop.

In Chapter 2, we develop an inverse Radon-transform method to reconstruct the distribution of slip velocity intensity (SVI) or stress drop on the fault plane during a large earthquake. Based on the dynamic crack model and the idea of the isochrone, we demonstrate that the observed source time function can be represented by a line integration along the isochrone of the

product of SVI and the velocity of the isochrone, the shape of which depends on the fault-observation point geometry and the rupture and wave velocities. The reconstruction of slip velocity on the fault plane is made by a direct back-projection method with a windowing procedure. The window size is determined mainly from the distribution of observation points. Our method has the advantage of not requiring a priori assumption of faulting area over the previous inversion studies of seismic source processes. Some simulation models used to test the applicability of our method show that it can recover well the distribution of SVI. Our method is applied to the records of the 1980 Izu-Hanto-Toho-Oki earthquake. The result shows a heterogeneous SVI distribution over the fault plane. Relatively large values of SVI are found in the center areas to the north on the fault plane inferred from the aftershock distribution, where less aftershocks occurred. The heterogeneous rupture effectively emitting high-frequency seismic waves is restricted to a smaller region than the inferred fault plane.

Chapter 1

Source Parameters of the 1983 Japan Sea Earthquake Sequence

1. Introduction

The source spectral scaling law of earthquakes is an important subject in studying the rupture mechanics of earthquakes and in predicting strong ground motions due to future earthquakes. Studies of the source parameters of the events of an earthquake sequence based on seismograms obtained at close distances have been reported by Frankel(1981) and Archuleta et al.(1982) for the 1980 Mammoth Lakes earthquake; Fletcher et al.(1984) for the 1975 Oroville earthquake; Muller and Cranswick(1985) for the 1982 Miramichi earthquake; and Boatwright(1985) for the 1983 Borah Peak earthquake.

Our purpose of the present paper is to examine the source spectral scaling of events in the 1983 Japan Sea earthquake sequence. Source spectral models such as the ω^{-2} model (Aki,1967; Brune,1970), the multi-crack model (Papageorgiou and Aki,1983a), and the single asperity model (Lay and Kanamori,1981; Das and Kostrov,1983) are used to classify the source spectra obtained from the observed seismograms.

The 1983 Japan Sea earthquake An earthquake of M_{JMA} 7.7 occurred at 11:59 on the 26th of May in 1983 on the east margin of the bed of the Japan Sea, about 80km west off the coast of Aomori and Akita prefectures in Northern Japan. The hypocenter of the earthquake was located at 40.35°N, 139.08°E and 14km in depth by the J.M.A. (Japan Meteorological Agency). The J.M.A. named the event the "1983 Nihon-Kai-Chubu earthquake", but we call it the 1983 Japan Sea earthquake in the present paper. The aftershocks in the first 14 days after the mainshock were distributed over an area of about 100x35km^2. On June 9, two large aftershocks (M_{JMA}=

6.1 and 6.0) occurred at the southern end of this aftershock region, and on June 21, the largest aftershock (M_{JMA}=7.1) occurred at the northern end of the mainshock area, and was accompanied by many smaller aftershocks .

From analyses of teleseismic body waves, Ishikawa et al.(1984) and Shimazaki and Mori (1984) concluded that the mainshock was a multiple event. From the analysis of accelerograms at epicentral distances from 80 to 280km, Sato(1985) found that the rupture process of the mainshock was composed of three major events: the first and the second events were identified on the basis of high-amplitude envelopes on the accelerograms and radiated high frequency seismic energies, whereas the third event did not emit significant high frequency seismic waves. From the waveform records at the telemetered stations of the Abuyama Seismological Observatory with epicentral distances from 630 to 810km, Kuroiso et al.(1986) found that the aftershock area could be divided into three parts on the basis of the frequency-content of the aftershocks, and that the aftershocks emitting high-frequency waves occurred only in the central part of the aftershock area, where the second sub-event of the mainshock began. Figure 1(a) shows the fault plane solution estimated by Ishikawa et al.(1984) based on waveform inversion of body waves. Figure 1(b) shows the source areas of the three major events in Sato's(1985) rupture model. The shaded areas in the southern and the central parts correspond to the source areas of the first and the second events, respectively. The unshaded area in the northern part indicates the source area

of the third event, which radiated relatively little high-frequency energy. The star symbol indicates the epicenter of the mainshock. Kuroiso et al.(1986) classified the epicentral distribution of the aftershocks into three types, based on the frequency content of the seismograms, as shown in Figure 1(c).

In the first part of this paper, we attempt to obtain the source spectra from the observed spectra by using an inversion method to remove propagation and site effects. The data sets are composed of the seismograms from the 1983 Japan Sea earthquake and its aftershocks at stations with hypocentral distance from 70km to 250km. For the inversion procedure, we assumed that each seismic spectrum is expressed as the product of the source spectrum of the event, the propagation path effects, the geometrical spreading, and the local site amplification effects near the station. The equations are linearized by taking the logarithms. Using the spectrum of the propagation effects and the site effects obtained by the above method, we can estimate the source spectra of smaller events even if they are recorded only at a single station.

In the second part of this paper, we determine the source parameters such as seismic moment, crack radius, and static and dynamic stress drops of each event from the source spectrum estimated using the above method. We discuss the dependence of the stress drops on seismic moment, and the relation between the dynamic stress drop and the static stress drop. Further, we examine the applicability of the ω^{-2} spectral model to the source spectrum by two methods. First, we compare the dynamic stress drop with the static stress drop, and second, we compare the

seismic moment and the corner frequency obtained from Andrews'(1986) automated objective method based on the ω^{-2} model with those from a hand-reading method. Other source models such as the multi-crack model or the asperity model are also used to model the source spectrum of each event.

2. Separation of source, path and local site effects on seismic spectra

2-1 Formulation of inversion

Several authors have tried to analyze observed seismograms to separate source and path effects. Papageorgiou and Aki (1983b) estimated the source power spectra of some large earthquakes by analyzing the observed power spectra (p_{ij}) at various stations. Assuming that the earthquake source is a point source, they modeled the predicted value of the power spectrum $P(f_i, r_j)$ at frequency f_i and at distance r_j by

$$P(f_i, r_j) = S(f_i)\, r_j^{-2} \exp(-2\pi f_i r_j / Q V_s) \qquad (1)$$

where $S(f_i)$: source power spectrum

Q_i : average quality factor of the path for S-wave

V_s : average S-wave velocity.

They also defined the factor

$$K^p{}_{ij} = p_{ij} / P(f_i, r_j) \qquad (2)$$

Using the property that the distribution of $\ln(K^p{}_{ij})$ is approximately Gaussian, they determined the parameters $S(f_i)$ and $Q_i = Q(f_i)$ by using the maximum likelihood method to minimize $(\ln K^p{}_{ij})^2$ for a set of m discrete frequencies and 2n records (radial and transverse components recorded at each of n stations).

On the other hand, Andrews(1982) assumed that the observed power spectrum could be expressed in the simple form

$$S_i(f)\, P_j(f) = O_{ij}(f) \qquad (3)$$

where $S_i(f)$: source power spectrum of the i-th earthquake

$P_j(f)$: local site effect near the j-th station

$O_{ij}(f)$: observed velocity spectrum of the i-th earthquake at the j-th station. Equation (3) is linearized by taking logarithms,

$$\log S_i + \log P_j = \log O_{ij}. \qquad (4)$$

Using I events, J stations and K(=IxJ) records, there are K equations to determine the I+J unknown parameters for each frequency. Andrews solved the matrix equation having K rows and I+J columns by using the singular value decomposition method.

In the present paper, we extend Andrews' equation (3) to consider both S-wave attenuation throughout the propagation path and the local site effect at each station (Iwata and Irikura,1986). We assume the quality factor of the wave attenuation is independent of the path and only depends on frequency (i.e., Q = Q(f)). Then the observed value of the S-wave Fourier amplitude spectrum is expressed by

$$o_{ij}(f) = s_i(f)\, g_j(f)\, R_{ij}^{-1} \exp(-\pi f R_{ij} / Q_s(f) V_s) \qquad (5)$$

where $s_i(f)$: source amplitude spectrum of the i-th earthquake

$g_j(f)$: local site effect near the j-th station

$o_{ij}(f)$: observed S-wave amplitude spectrum of the i-th earthquake at the j-th station

R_{ij} : hypocentral distance between the i-th earthquak and the j-th station. In order to obtain a linear equation, we take the logarithm of equation (5)

$$\log(o'_{ij}) = -\log R_{ref} + \log(s_i) + \log(g_j) - \log e\, (\pi f R_{ij} / Q_s V_s) \qquad (6)$$

where e is Napier's number, $o'_{ij} = (R_{ij}/R_{ref}) o_{ij}$, and R_{ref} is the arbitrary normalized distance (in this study, we use that the normalized distance is 1km). We shall determine I (source

amplitude spectra) + J (local site effects) + 1 (Q-value) parameters from the IxJ data sets at each frequency using the least square method.

As indicated by Andrews(1982,1986), there is one unconstrained degree of freedom in this system of equation: at each frequency all of the propagation spectra may be divided by a constant value and all of the source spectra may be multiplied by the same value without affecting the fit. Andrews(1982) used the additional constraint that the logarithms of the propagation spectra sum to zero, i.e.

$$\sum_{j=1}^{N} \log (P_j) = 0 \qquad (7)$$

This constraint has no clear physical meaning. Therefore, we use the constraint that the factor for the local site effect must be at least 2, due to the free surface amplification effect.

$$g_j (f) \geqq 2 \qquad (8)$$

The validity of this constraint is discussed in the next section. We solved the resulting linear least squares problem with linear inequality constraints using the singular value decomposition method (Lawson and Hanson,1974).

The above inversion procedure allows us to separate the source spectrum, the Q-values of the propagation media, and the local site effect. Then we can estimate the source parameters for other events from the source spectrum even at only one station, by removing the propagation path and site effects.

2-2 Data

Figure 2 and Table 1 show the hypocentral locations determined by the J.M.A. and the stations used in our study. We used two independent data sets of the records for the 1983 Japan Sea earthquake sequence. The one data set was made up of the records of the mainshock and the largest aftershock obtained at six three-component stations: HRD (Hirosaki University), MUR (Muroran), HAK (Hakodate), AOM (Aomori), TUC (Tsuchizaki) and FRF (Furoufushi). Stations HAK, AOM and TUC were equipped with SMAC-B2 type and MUR with ERS type strong motion accelerometers by the P.H.R.I.(the Port & Harbour Research Institute). The acceleration records at HRD were obtained by the Earthquake and Volcanic Observatory, Hirosaki University with force-balance type accelerometers. The mainshock record at FRF was obtained by the Central Research Institute of the Electric Power Industry with an SMA-1 type strong motion accelerometer. The largest aftershock record at FRF was obtained with a force-balance type accelerometer. The instrumental response of the SMAC-B type seismometer was corrected to be a flat acceleration response in the frequency domain (Iai et al.,1978). The other accelerometers have a flat acceleration response in the frequency range less than 10Hz. Because the acceleration record of the largest aftershock at TUC was not be available, we used the velocity records of the largest aftershock obtained with the strong velocity seismometer (Muramatu,1977) temporarily set up near the accelerometer after the mainshock. The ground motions of the mainshock were clearly divided into two wave groups, which indicates that the mainshock was a multiple event (e.g. Sato,

1985). Thus we regard the mainshock as two events: the 1st main event and the 2nd main event. In summary, the first data set consists of the 18 records of the 3 events (the 1st and the 2nd main events of the mainshock and the largest aftershock) observed at 6 stations.

The other data set consists of the records of several aftershocks observed by the research groups of Gifu University and Kyoto University with the strong velocity seismometers at 3 stations, TUC, TEG, and FKR. Station TUC was set up about 40m south of the accelerometer site of the P.H.R.I. At these stations we observed the ground motion from aftershocks ranging in magnitudes (M_{JMA}) from 3.8 to 7.1. This seismometer has a flat amplitude response in velocity in the range from about 0.03 to 20Hz. This data set consists of 30 records of 10 aftershocks ranging in magnitude from 4.0 to 6.1. In the following, we will call the former data set Set I and the latter Set II.

The procedure of our inversion is as follows. We analyzed the S-wave portions of the two horizontal components (NS and EW components). [1] Data length for analysis For Set I, we used the first 20 seconds after the onset of the S-waves, with a sine tapered window (10 percent at each end of the time window). The onset of the S-waves from the 2nd main event was detected with the complex envelope method (Fernbach, 1975). Figure 3 shows an example of the acceleration seismogram of the NS-component observed at HRD and its envelope. Arrows show the S-wave onset from the 1st main event and the 2nd main event, respectively. For Set II, we used a length of 4 seconds with a modified Hanning

window beginning after the onset of the S-waves. [2] Fourier amplitude spectra The Fourier amplitude spectra of the two horizontal components were computed with Maximum Entropy Method(Saito,1978). The velocity amplitude spectra of Set I for the records of the largest aftershock at TUC and Set II were post-multiplied by $2\pi f$ (f:frequency) to produce acceleration amplitude spectra. The observed Fourier amplitude spectrum of the earthquake observed at each station for the inversion was obtained by the energy summation of the two horizontal components. [3] Standard deviation By applying formula (5) to the spectral data set, we chose 10 frequencies in the frequency range from 0.5Hz to 8.0Hz. The observed spectral value and standard deviation at a frequency (say f_1) were estimated by taking the average and standard deviation of the amplitude spectrum in the frequency band from $0.8f_1$ to $1.2f_1$. Figure 4(a) shows an example of the velocity seismograms of the NS and EW components observed at FKR from the onset of S-waves and the windowed seismograms, Figure 4(b) shows the Fourier acceleration amplitude spectra, and Figure 4(c) shows an example of the inversion data set: the observed acceleration spectra of an earthquake observed at three stations.

2-3 Results of inversion

Q_S-value Figure 5 shows the Q_S-values obtained by the inversion as a function of frequency. Open circles indicate the Q_S-values obtained from Set I (the two main events of the mainshock and the largest aftershock) and the cross marks indicate the values obtained from Set II (the aftershocks). The hatched region indicates the estimated standard deviations of the

Q_s-values. The Q_s-values clearly tend to increase with frequency, being roughly proportional to (frequency)$^{0.7}$ in the frequency range from 0.5 to 8.0Hz (thus, $Q_s \sim 100f^{0.7}$). In Figure 5, we also plotted the Q-values obtained by other authors. Open squares indicate the Q_s-values obtained by Sato(1985) using the mainshock records and closed squares indicate the Q_c-values obtained by Idei(1983) using the S-wave coda parts of aftershock records. Their results are in good agreement with those in this study in the frequency range from 0.5Hz to 8.0Hz.

Local site effect Figure 6 (a) shows the site responses obtained from Set I and (b) shows those obtained from Set II with error bars (standard deviation). The site effects at TUC(Tsuchizaki), which may be regarded as the same station in Set I and II, from the two independent data sets agree within one standard deviation, which supports the validity of this inversion result. We compare our estimated site effects with another observational result for the local site amplification effects. Kitsunezaki(1985) observed the ground motion from the aftershocks at many temporary stations in Akita City. In his report, the amplitude spectra of the ground motions at TEG (Tegata) were about 5 times as large as those at a bed rock site in the frequency range from 4Hz to 6Hz. Our inversion result is consistent with his result for TEG in Figure 6(b).

Shallow boring and S-wave logging near TUC were conducted by Watanabe et al.(1984). They obtained the S-wave velocities and the densities up to 25m as shown in Table 2. Yoshii and Asano (1972) determined a P-wave structural model along a line passing

near TUC from the explosion seismic data. We assume the subsurface structure at TUC based on the shallow well-logging data and the P-waves exploration data for deeper layers. The S-wave velocities in the deeper layers are obtained from the P-wave velocities with assuming Poisson's condition (V_p=1.73V_s). The Q_s-values are obtained from the empirical relation between the Q_s-values and the S-wave velocities given by Kudo and Shima(1970). Table 2 shows the structure parameters for the theoretical calculation. We calculated the site amplifications for SH-waves using Silva's(1976) formulation of the Thomson-Haskell's matrix method including the effects of inelastic attenuation. Figure 7 shows the theoretical site amplification at TUC with the normal incidence of plane-wave. This theoretical site response agrees well with the observed ones inverted from Sets I and II in the frequency range from 0.5Hz to 5Hz. However, there are some discrepancies between the theoretical and observed site responses at frequencies higher than 5Hz. This might be due to the constraint that the site amplification factor is greater than 2 in account with the free surface amplification. In Figure 7, we can see that the site amplification factor is less than 2 at higher frequencies because of the unelastic attenuation effect within the near surface layers. Therefore we consider the result from the inversion for the site amplification factor in the frequency range only between 0.5Hz and 5.0Hz to be reliable. The site response at FKR is 2 in the frequency range 0.5-8.0Hz and that at FRF is 2 from 0.5 to 4.0Hz (see Figures 6(a) and (b)). These results may be explained that these stations are on Tertiary sandstone that is stiffer than the subsoils at the other

stations.

Source spectra Acceleration source spectra of the 1st and 2nd events of the mainshock, the largest aftershock, and several other aftershocks are plotted in Figure 8. The standard deviations are shown by the error bars on the spectral curves. All of the spectra decrease rapidly in the frequencies higher than 5Hz. These results may have been influenced by the overestimation of the site amplification due to the constraint discussed above. The acceleration spectra of the larger events, such as the two events of the mainshock and the largest aftershock, show rapid decay beyond 3Hz. The upper bound frequency of 3Hz agrees well with the value of f_{max} determined by Sato(1985).

3. Scaling relation of source parameters of the 1983 Japan Sea Earthquake

3-1 Source parameters

We estimate the source parameters of aftershocks from the source spectra. In order to obtain the source spectra, we need to remove the propagation and site effects from the observed spectra. We rewrite (5) as follows,

$$s_i(f) = R_{ij} \exp(\pi f R_{ij} / Q_s(f) V_s) o_{ij}(f) / g_j(f)$$

$$= C_{ij}(f) o_{ij}(f) \qquad (9)$$

In (9) we introduce a correction function $C_{ij}(f)$ to estimate the source spectra. $C_{ij}(f)$ is determined from the total path effects, i.e., the Q_s-values of the propagation path, Q_s, the site amplification, g_j, and the hypocentral distance, R_{ij}. In the previous section, we estimated Q_s in the frequency range from 0.5Hz to 8.0Hz and g_j in the range from 0.5Hz to 5.0Hz. The site amplification in the range greater than 5.0Hz is given so that the value of site amplification at TUC agrees with the theoretical value in the previous section. $C_{ij}(f)$ at frequencies lower than 0.5Hz are much important for evaluating the seismic moment and the corner frequency of each event. However, we have no knowledge about the total path effects in that frequency range. Almost all authors in the scaling law of source spectra have treated the spectral levels of displacement as flat up to the corner frequency (e.g. Brune,1970; Aki,1967,1972; Hanks,1979; Joyner,1983). Using the above property, we can estimate the total path effects due to the propagation path and the local site effects at frequencies lower than 0.5Hz by using smaller aftershocks as described in the following.

We select several earthquakes whose corner frequencies(f_0) are higher than 0.5Hz. We calculate the source displacement amplitude spectra of these earthquakes in the frequency range from 0.5Hz to 8.0Hz using (9). These source displacement amplitude spectra are roughly flat in the frequency range from 0.5Hz to each corner frequency. The source spectra at frequencies lower than 0.5Hz is extrapolated using the average level between 0.5Hz and the corner frequency. The correction function in the frequency range lower than 0.5Hz is defined to be the difference between the flat level and the observed spectra. Figure 9 shows this procedure. In Figure 9(a), the solid line indicates the observed displacement spectrum and the dotted line indicates the source displacement amplitude spectrum corrected by effects of Q-values and local site in the frequency range from 0.5Hz to 8.0Hz. In Figure 9(b), solid line indicate the displacement spectra of the aftershocks observed at FKR, which are corrected to coincide with the evaluated source spectral level at 0.5Hz, and the dotted line indicates the flat level of the evaluated source spectra in the frequency range between 0.5Hz and each corner frequency. In Figure 9(c), we show the correction function for FKR at frequencies lower than 8.0Hz for an hypocentral distance of 50, 100, and 200km, respectively. The correction functions for TUC and TEG are also determined using the same procedure.

Using the appropriate correction function for the observed source spectra of records from the aftershocks at each station (FKR, TUC, and TEG), we obtain the source spectra from equation (9) and determine the flat level of the source displacement

spectrum (Ω_0), that of source acceleration spectrum (a_0), and the corner frequency (f_0). For the Brune's(1970,1971) scaling law for far-field shear wave spectra, the seismic moment (M_0) is defined by

$$M_0 = 4\pi\rho r V_s^3 \Omega_0 / R(\theta, \phi) \qquad (10)$$

where $R(\theta,\varphi)$ is the radiation coefficient for S-waves and r is the hypocentral distance. Following Brune(1970), we determine the corner frequency as the frequency at the intersection of the low- and high-frequency asymptotes in each source displacement spectrum. In Figure 10, we show an example of using the source displacement amplitude spectrum to determine the seismic moment and the corner frequency. The relation between the corner frequency (f_0) and the crack radius (r_0) used here is

$$r_0 = 0.21 V_s / f_0 \quad (\text{rupture velocity } V_r = 0.9 V_s) \qquad (11)$$

from Madariaga(1976), assuming a dynamic crack model and that the fault size (the circular crack radius) is given by $S = \pi r_0^2$. Figure 11 shows the relationship between the seismic moment and the corner frequency of each event. We find that the events in this earthquake sequence are roughly governed by the scaling relation that Mo is proportional to fo^{-3}. The oblique lines proportional to f^{-3} indicate a constant static stress drop if a constant rupture velocity is assumed.

Another important source parameter is the stress drop, which can indicate the tectonic stress as long as the frictional stress of material in the faulting region is given. Many authors have used various scaling laws to estimate stress drops, as summarized by Boatwright (1984) and Hanks et al.(1985). In this study, we estimate the static stress drop obtained from the flat

level of the displacement spectrum (the seismic moment), and the dynamic stress drop obtained from the flat level of the acceleration spectrum. The static stress drop ($\Delta\sigma_S$) is defined by Keilis-Borok(1959):

$$\Delta\sigma_S = \frac{7}{16}\frac{M_0}{r_0^3} \qquad (12)$$

This is the same as the stress drop for the circular crack model by Brune(1970,1971). The dynamic stress drop ($\Delta\sigma_D$) is defined by Madariaga (1977) from the flat level of the source acceleration spectrum in the high frequency range. Boatwright (1982) rewrote Madariaga's result to express the dynamic stress drop as

$$\Delta\sigma_D = \frac{\rho V_s^2}{V_r \underline{R}_c(\theta,\phi)\, r_0} a_0 \qquad (13)$$

where $R_c(\theta,\varphi)$ is the radiation coefficient defined by Boatwright (1982), ρ is medium density, and a_0 is the flat level of the source acceleration spectrum in the high frequency range. Also, the local stress drop ($\Delta\sigma_L$) is defined by Papageorgiou and Aki (1983a,1983c,1984,1985) for the specific barrier (multi-crack) model:

$$\Delta\sigma_L = \frac{4\rho V_s^2}{(\text{factor})(24/7\pi) V_r \underline{R}(\theta,\phi)\sqrt{S}} a_0 \qquad (14)$$

where (factor) is a function of V_r/V_s. Papageorgiou and Aki(1983a,1985) used Sato and Hirasawa's kinematic circular crack model (1973) as circular sub-cracks on the fault plane for the specific barrier model. If we apply Madariaga's dynamic circular crack model instead of Sato and Hirasawa's model to the sub-cracks of the specific barrier model, equation (14) for the local stress drop gives almost the same value as equation (13) for the dynamic stress drop.

The parameters (the seismic moment, the corner frequency,

the crack radius, the static stress drop, and the dynamic stress drop) shown in Table 3 are estimated using the following values of the above constants: ρ = 2.7 g/cm^3, V_S = 3.7 km/s, $R(\theta,\varphi)$= 0.63 (average radiation coefficient as given by Boore and Boatwright,1984), and $R_c(\theta,\varphi)$= 0.40 (Boatwright,1982). The seismic moment of the two main events was determined by Ishikawa et al.(1984) and those of the largest aftershock and the aftershocks with M_{JMA} = 6.1 and 6.0 are from the centroid moment tensor table of Dziewonski et al.(1983) and the crack radii (half of the fault length) of these events were based on the aftershock region determined by Tohoku University and Hirosaki University(1984). The total seismic moment of the main event found by Ishikawa et al. is two-thirds of that found by Dziewonski et al. This discrepancy controls the upper bound of the estimated error for the static stress drop of the mainshock. The parameters expressed as figures with bracket in Table 3 are estimated using the seismic moment and crack radius reported by these authors.

3-2 Scaling relation of source parameters.

In the following figures, we classify the area of this earthquake sequence into three regions: the A-region, the aftershock region of the events with M=6.1 and 6.0; the B-region, that of the mainshock; and the C-region, that of the largest aftershock with M=7.1. Figure 12 shows the relation between the seismic moment and the stress drops. Figure 12(a) shows the logarithm of seismic moment versus the logarithm of static stress drop and Figure12 (b) shows the logarithm of seismic moment versus the logarithm of dynamic stress drop. The cross at the

bottom left of Figures 12(a) and (b) indicates the estimated error bar. In the seismic moment range from $3x10^{21}$-$2x10^{25}$ dyn*cm, the stress drops seem to show neither any systematic variation nor any dependence on seismic moment. The upper bound of the stress drops appears to be several hundreds bars.

Figure 13 shows the relationship between the dynamic stress drop and the static stress drop of events. Points lying on the solid line in this figure imply events whose dynamic stress drop and static stress drop are equal. The ω^{-2} models such as a single crack rupture predict that two kinds of stress drops should have the same value. When the rupture process of an event is more complex, higher frequency seismic waves are more strongly excited, and consequently, the dynamic stress drop is higher than the static stress drop. There are several aftershocks with a complex rupture history in regions A and C. The aftershock with M=6.1 has a dynamic stress drop almost equal to the static stress drop. Therefore, the aftershock with M=6.1 is interpreted as having had a simple rupture process. In contrast, the aftershocks with M=7.1 and 6.0, whose dynamic stress drops are higher than their static stress drops , have more complex rupture processes.

Figure 14 shows the relationship between the seismic moment and the ratio of the dynamic stress drop to the static stress drop. We find that the ratios are independent of the seismic moment although they scatter to some extent. We find further that the static stress drops are generally a lower bound of the dynamic stress drops. Since the estimated errors become generally larger when we take a ratio between two estimated values, we cannot infer the detail of the source process of this earthquake

sequence on the basis of Figure 14. A further test of the applicability of the ω^{-2} model will be made in Discussion.

Figure 15 shows the spatial distribution of the aftershocks analyzed here, with the dynamic stress drops indicated by the size of the open circles. The aftershocks with relatively higher dynamic stress drop mainly occur in the A- and C-regions. On the contrary, in the B-region, i.e., the mainshock region, the aftershocks have lower dynamic stress drops than in the other regions, but there are some aftershocks with relatively higher dynamic stress drops in the center of this mainshock region. This area corresponds to the barrier between the first event and the second event during the mainshock. Unfortunately, the aftershocks analyzed in the present paper are not distributed uniformly in the B-region. Thus it is hard to discuss in detail the spatial distribution of heterogeneity in the mainshock region.

4. Discussion

In this section, we discuss the type of source models that can explain the source characteristics of the events in the previous section. Andrews(1986) proposed an automated objective method to determine the corner frequency and the flat level of the source displacement spectrum assuming that the source spectrum is prescribed by the ω^{-2}-model. The ω^{-2}-source displacement spectrum (D(f)) is given by the following formula,

$$D(f) = \frac{\Omega_0}{1 + (f / f_0)^2} \qquad (15)$$

where omega is the flat level of the source displacement spectrum and f_0 is the corner frequency. For simplicity, he used V(f) = D(f)/2πf : velocity spectrum,

$$SD = 2 \int_0^\infty D^2(f)\, df \qquad (16)$$

and

$$SV = 2 \int_0^\infty V^2(f)\, df \qquad (17)$$

Then, the corner frequency and the flat level of the displacement spectrum are described by

$$f_0 = 1/2\pi\, (SV/SD)^{1/2} \qquad (18)$$

and

$$\Omega_0 = (2SD/\pi f_0)^{1/2} \qquad (19)$$

The seismic moment is calculated by substituting omega given by (19) into (10). The corner frequency and the seismic moment obtained using the above method are compared with those obtained from hand-reading in the previous section. For example, if the corner frequency and the seismic moment of one event obtained from this automatic method are equal to those determined by hand-reading, that event is interpreted as having an ω^{-2}-source spectral structure. This is not a sufficient condition, but is a necessary condition. If the spectral structure is not the ω^{-2} model, we will obtain incorrect values for the corner frequency

and the seismic moment. In the Appendix, we show the difference between the estimated values of the seismic moment and the corner frequency by Andrews' automated objective method and those by the hand-reading method for several source spectral models numerically.

The corner frequency and the seismic moment determined by Andrews' automated method are also shown in Table 3. In Figure 16, we compare the corner frequency and the seismic moment determined by Andrews' method with those determined by the hand-reading method. Figure 16(a) and (b) show a comparison of the the corner frequency and the seismic moment determined by the two methods. In Figure 16(a), we find that Andrews' method and the hand-reading method give almost the same values of the seismic moment in the seismic moment range from $2x10^{21}$ to $3x10^{22}$ dyn*cm. However, for several events with a seismic moment greater than $3x10^{22}$ dyn*cm, a smaller seismic moment is obtained from Andrews' method than from the hand-reading method. The second largest aftershock with M=6.1(seismic moment is about 10^{25}dyn*cm) has the same values for the two methods, but the first and the third largest aftershocks, with M=7.1 and M=6.0, respectively, have a smaller seismic moment from Andrews' method than from the hand-reading method. The difference between the corner frequencies from both methods is also shown in Figure 16(b). The first and the third largest aftershocks have a higher corner frequency from Andrews' method than from the hand-reading method.

From the above results, the rupture process of this earthquake is summarized as follows. The events in the seismic

moment range $2x10^{21}$-$3x10^{22}$ dyn*cm have a simple source process described by the ω^{-2} model, but there are several events with a seismic moment greater than $3x10^{22}$dyn*cm which have a rather complex rupture process which cannot be described by the ω^{-2} model. The static and dynamic stress drops of the former events are equal, whereas the latter events have higher dynamic than static stress drops.

We can consider two models which can explain the complex rupture process described above; one model is the multi-crack model based on strength heterogeneity in the fault plane (Papageorgiou and Aki,1983) and the other is the asperity model based on stress heterogeneity (Lay and Kanamori,1981; Das and Kostrov,1985). These models are characterized by parameters such as the number of cracks for the multi-crack model or the stress drop heterogeneities for the asperity model. These parameters can be determined from the ratio of the dynamic stress drop ($\Delta\sigma_D$) to the static stress drop ($\Delta\sigma_S$) of each event. Returning to the definitions of these stress drops,(12) and (13), we can express the ratio of $\Delta\sigma_D$ to $\Delta\sigma_S$ as follows,

$$\frac{\Delta\sigma_D}{\Delta\sigma_S} \sim \frac{a_0}{\Omega_0 r_0^2} \qquad (20)$$

For the simple ω^{-2} model, ao = $(2\pi * fo)^2 * \Omega o$ and the above ratio is equal to unity. For the multi-crack model, this ratio is equivalent to $N^{\frac{1}{2}}$, where N is the number of cracks (Irikura and Aki,1988). On the other hand, for the asperity model, the dynamic stress drop corresponds to the stress drop in the asperity, while the static stress drop is the average stress drop over the source area. The ratio of the dynamic to the static stress drops is an important parameter to explain the complex

source processes such as the multi-crack or the asperity model. We cannot distinguish between these models from analyzing source spectra alone for events with source characteristics different from the ω^{-2} model. Distinguishing between those models clearly requires analysis of the source function of space and time, and cannot be done only on the basis of spectral data.

5. Conclusion

We determine the source characteristics of the events of the 1983 Japan Sea earthquake sequence. We attempt to separate the source, the propagation path, and the site effects by using the inversion procedure we developed.

From the inversion results, Q_s-values are proportional to $f^{0.7}$, in the frequency range from 0.5 to 8.0Hz. The site effects at the same station (TUC) estimated from two independent data sets agree within one standard deviation, which supports the validity of our inversion results. By using the propagation path and the site effects obtained from the inversion, we determined the source spectra of the events. The rupture process of each event is examined by comparing the corner frequency determined by the hand-reading method to that determined by Andrews' automated objective method based on the ω^{-2} model and the ratio of the static stress drop to the dynamic stress drop. These results show that the events in the seismic moment range from 2×10^{21} to 3×10^{22} dyn*cm fit the ω^{-2}-source spectral model, but there are some events which do not fit the ω^{-2} model with a seismic moment greater than 3×10^{22} dyn*cm. The source characteristics of the large aftershocks with M=7.1(the largest aftershock) and M=6.0 show significant departures from the ω^{-2} model.

These events may have complex rupture processes, which can be explained, using models such as the multi-crack model or the asperity model. To parameterize the complex rupture process, we evaluate the parameters such as the number of cracks for the multi-crack model or the stress drop heterogeneities for the asperity model. We cannot distinguish between the multi-crack

model and the asperity model from only analyses of the spectral characteristics of the events.

Appendix

Here we show the difference between the estimated values of the seismic moment and the corner frequency by Andrews' automated objective method(1986) and those by the hand-reading method for several source spectral models numerically. We check for the following three source spectral models [1] ω^{-2} model(Aki,1967), [2] ω^{-3} model(Haskell,1966), and [3] the multi-crack model (Irikura,1986) and their formulae are as follows.

[1] ω^{-2} model: $S(f)=Mo/(1+(f/fo)^2)$ (A1)

[2] ω^{-3} model: $S(f)=Mo/(1+(f/fo)^3)$ (A2)

[3] multi-crack model: $S(f)=(N(1+(N-1)(\sin X/X)^2))^{1/2}*Se(f)$ (A3)

where fo is the corner frequency, N is the crack number, and $X=\pi*f/fo$. Se(f) is the subevent source spectrum which obeys the ω^{-2} model. Then,

$Se(f)=Me/(1+(f/fe)^2)$, (A4)

where Me=Mo/N, and the corner frequency of the subevent (fe) is given by

$fe=fo*N^{1/2}$. (A5)

Figure A1 shows the spectra of these three source spectral models. In the multi crack model, we choose the crack number is 10. Each spectrum is normalized to the low frequency level. We determined the seismic moment and the corner frequency by Andrews' method shown in Table A1. In ω^{-3} model, the estimated seismic moment is greater than the given one and the estimated corner frequency is smaller than the given one. On the other hand, in the multi-crack model the estimated seismic moment is smaller than the given one and the estimated corner frequency is

greater than the given one. Of course, as the seismic moment is estimated from the flat level of the source displacement spectrum, it is hardly understood why the different seismic moment value of automated objective method are obtained from that of hand-reading method. Because Andrews' seismic moment is estimated from Andrews' corner frequency defined by formula (19). These tendencies come from the different decay of source spectrum in the high frequency range between the ω^{-3} model and the multi-crack model. The reverse is also true and we can infer the source spectral model if we have different values between the estimated values of the seismic moment or the corner frequency by Andrews' method and those of hand-reading method.

Figure Captions

Fig.1 (a) Fault plane solution of the 1983 Japan-Sea earthquake estimated by Ishikawa et al.(1984) with the body waveform inversion method represented by Kikuchi and Kanamori (1982).

(b) The division of the fault surface of this event according to different excitation of high-frequency seismic energy determined by Sato(1985) from the accelerograms with the hypocentral distances from 80 to 280km. The shaded areas in the southern and the central parts correspond to the source areas of the first and the second events emitting high frequency seismic waves. The unshaded area in the northern part indicates the source area of the third event radiated relatively little high frequency seismic waves. The star symbol indicates the epicenter of the mainshock.

(c) Epicenter distribution of the aftershocks classified into three types with the frequency characteristics by Kuroiso et al.(1986) Open circle, plus sign, and solid circle indicate type L(emitting lower frequency seismic wave), M(intermediate frequency), and H(higher frequency), respectively.

Fig.2 Map of the epicentral locations used in the inversion determined by the J.M.A.

Fig.3 An example of acceleration seismogram of NS-component observed at HRD and its envelope. Arrows show the S-wave onset from the 1st and 2nd main events.

Fig.4 (a) Left: An example of the velocity seismograms of NS and

EW components observed at FKR from the onset of S-waves. Right: these records multiplied by a modified Hanning window function with the duration 4-sec from the onset S-waves.

(b) Fourier amplitude acceleration spectra of NS and EW components shown in (a). The acceleration spectra were obtained by differenciating the velocity spectra in the frequency domain.

(c) An example of the observed acceleration spectra at three stations (FKR,TEG, and TUC) as an inversion data corrected the geometrical spreading effect at the focal distance of 1km.

Fig.5 Q_s-values determined by the inversion as a function of frequency. Open circles indicate the Q_s-values obtained from Set I and crosses from Set II. Open squares indicate those from the mainshock by Sato(1985) and closed squares indicate Q_c-values from the coda-waves of aftershocks by Idei(personal communication,1983).

Fig.6 Site amplification effects determined by the inversion. (a) is for Set I and (b) for Set II, respectively.

Fig.7 Theoretical site amplifications at TUC. The site amplifications of SH-waves are calculated by Thomson-Haskell's matrix method including the effect of the inelastic attenuation (Silva,1976).

Fig.8 Some examples of results for the source acceleration amplitude spectra. The error bar indicates each standard deviation.

Fig.9 Procedure of estimating the source spectra from the

observed seismic spectra.

(a) The observed seismic displacement spectra (solid line) and the evaluated seismic displacement spectra (dotted line) from removing the propagation path and site effects obtained from the inversion in the frequency range higher than 0.5Hz.

(b) Solid lines indicate the displacement spectra corrected in the frequency range higher than 0.5Hz of some aftershocks observed at FKR with arranging these flat levels. The dotted line indicates the average flat level of these spectra in the range from 0.5Hz to each corner frequency.

(c) The correction function of the propagation path and the site amplification effects for FKR in the range lower than 8.0Hz with hypocentral distances 50, 100, and 200km, respectively.

Fig.10 Corrected displacement amplitude spectra for determining the flat level of source displacement spectrum and the corner frequency. The arrow shows the corner frequency obtained from the intersection of the low frequency asymptote and the high frequency asymptote.

Fig.11 Logarithm of seismic moment versus the logarithm of corner frequency. Lines of constant static stress drop are indicated. The cross at the bottom indicates the estimated error bar.

Fig.12 (a) Logarithm of seismic moment versus the logarithm of static stress drop. The cross at the bottom indicates the estimated error bar.

(b) Logarithm of seismic moment versus the logarithm of dynamic stress drop.

Fig.13 Relationship between the dynamic stress drop and the static stress drop. Points lying on the solid line denote events whose dynamic stress drop and static stress drop are equal.

Fig.14 Relationship between the seismic moment and the ratio of dynamic stress drop to static stress drop.

Fig.15 Spatial distribution of the aftershocks analyzed here, with the dynamic stress drops indicated by the size of the open circle.

Fig.16 (a) Seismic moment determined by the hand-reading method versus that of Andrews' automated objective method. The cross at the bottom indicates the estimated error bar.
(b) Corner frequency determined by the hand-reading method versus that of Andrews' automated objective method.

Table 1 Epicenters determined by the J.M.A. and observation stations used in the inversion.

Table 2 Parameters of subsurface structures at TUC from Watanabe et. al.(1984).

Table 3 List of source parameters obtained in this study.

Fig. A1 Displacement amplitude spectra of three spectral models, [1] ω^{-2} model, [2] ω^{-3} model, [3]the multi-crack model.

Table A1 Values of relative seismic moments and corner frequencies for each source spectral models estimated from Andrews' automated objective method.

REFERENCES

AKI,K., Scaling relation of seismic spectrum, J. Geophys. Res., 72, 1217-1231, 1967.

AKI,K., Earthquake mechanism, Tectonophysics, 13, 423-446, 1972.

ANDREWS,D.J., Separation of source and propagation spectra of seven Mammoth Lakes aftershocks, Proceedings of Workshop 16, Dynamic characteristics of faulting,1981,U.S.Geol.Sur. Open File Rep., 82-591, 437, 1982.

ANDREWS,D.J., Objective determination oof source parameters and similarity of earthquakes of different size, Earthquake Source Mechanics, Maurice Ewing Series 6, edited by S.Das, J.Boatwright and C.H.Scholz, Am.Geophys.Union, Washinton,D.C., , 259-267, 1986.

ARCHULETA,R.J., E.CRANSWICK, C.MUELLER and P.SPUDICH, Source parameters of the 1980 Mammoth Lakes, California, earthquake sequence, J. Geophys. Res., 87, 4594-4607, 1982.

BOATWRIGHT,J., A dynamic model for far-field acceleration, Bull. Seism. Soc. Am., 72, 1049-1068, 1982.

BOATWRIGHT,J., Seismic estimates of stress release, J. Geophys. Res., 89, 6961-6968, 1984.

BOATWRIGHT,J., Characteristics of the aftershock sequence of the Borah Peak, Idaho, earthquake determined from digital recordings of the events, Bull. Seism. Soc. Am., 75, 1265-1284, 1985.

BOORE,D.M. and J.BOATWRIGHT, Average body-wave radiation coefficient, Bull. Seism. Soc. Am., 74, 1615-1621, 1984.

BRUNE,J.N., Tectonic stress and the spectra of seismic shear waves from earthquakes, J. Geophys. Res., 75, 4997-5009, 1970.

BRUNE,J.N., Correction, J. Geophys. Res., 76, 5002, 1971.

DAS,S. and B.V.KOSTROV, Breaking single asperity: Rupture process and seismic radiation, J. Geophys. Res., 88, 4277-4288, 1983.

DZIEWONSKI,A.M., J.E.FRANSEN, and J.H.WOODHOUSE, Centroid-moment tensor solution for April-June,1983, Phys. Earth Planet. Interiors, 33, 243-249, 1983.

FERNBACH,J.S., The complex envelope in seismic signal analysis, Bull. Seism. Soc. Am., 65, 952-962, 1975.

FRANKEL,A., Source parameters and scaling relationships of small earthquakes in the northeastern Caribbean, Bull. Seism. Soc. Am., 71, 1173-1190, 1981.

FLETCHER,J., J.BOATWRIGHT, L.HARR, T.HANKS, and A.McGARR, Source parameters for aftershocks of the Oroville, California,

earthquake, Bull. Seism. Soc. Am., 74, 1101-1124, 1984.

HANKS,T.C., b values and w^{-r} seismic source models: implications for tectonic stress variations along active crustal fault zones and the estimation of high-frequency strong ground motion, J. Geophys. Res., 84, 2235-2242, 1979.

HANKS,T.C., M.C.ANDREWS, J.L.BOATWRIGHT, J.B.FLETCHER, Earthquake stress drops, Proceedings of the 5th Maurice Ewing symposium on earthquake source mechanics, , AGU, 1985.

HASKELL,N.A., Total energy and energy spectral density of elastic wave radiation from propagation faults. II., Bull. Seism. Soc. Am., 56, 125-140, 1966.

IAI,S., E.KURATA and H.TSUCHIDA, Digitization and corrections of strong-motion accelerograms, Tech. Note Port Harbour Res. Inst., 286, 1-56(in Japanese), 1978.

ISHIKAWA,Y., M.TAKEO, N.HAMADA, M.KATSUMATA, K.SUDO, M.TAKAHASHI, S.KASHIWABARA and N.MIKAMI, Source process of the 1983 Japan Sea earthquake, Chikyu, 6, 11-17(in Japanese), 1984.

IRIKURA,K., Prediction of strong ground motions using empirical Green's function, Proceedings of the 7th Japan earthquake engineering symposium, , 151-156, 1986.

IRIKURA,K. and K.AKI, Scaling law of seismic source spectra and empirical Green's function for predicting strong ground motions, submitted in Bull. Seismol. Soc. Am., , , 1988.

IWATA, T., and K.IRIKURA, Separation of source, propagation and site effects from observed S-waves, Zisin II, 39, 579-593(in Japanese), 1986.

JOYNER,W.B. and D.M.BOORE, Peak horizontal acceleration and velocity from strong ground motion records including records from the 1979 Imperial valley, California, earthquake, Bull. Seism. Soc. Am., 71, 2011-2038, 1981.

KEILIS-BOROK,V.I., On estimation of the displacement in an earthquake source and of source dimensions, Ann. Geofis, 12, 205-214, 1959.

KIKUCHI,M. and H. KANAMORI, Inversion of complex body waves, Bull. Seism. Soc. Am., 72, 491-506, 1982.

KITSUNEZAKI,C., Ground characteristics in marginal area of dune in Akita city with respect to earthquake disaster, Scientific and Technical reports of the Mining Collage, Akita University, 6, 43-60(in Japanese), 1985.

KUDO,K. and E.SHIMA, Attenuation of shear wave in soil, Bull. Earthq. Res. Inst., 48, 145-158, 1970.

KUROISO, A., K.ITO, Y.UMEDA, Y.IIO, and H.MURAKAMI, Anomalously high frequency aftershocks and source characteristics of the Mid-Japan Sea earthquake, Zisin II, 39, 419-430(in Japanese), 1986.

LAY,T. and H.KANAMORI, An asperity model for great earthquake sequences, Earthquake Prediction -An International Review-, Maurice Ewing Series, edited by D.W.Shimpson and P.G.Richards, Am. Geophys. Union, Washinton, D.C., 4, 579-592, 1981.

LAWSON,C.L. and R.J.HANSON, Solving least squares problems, , , Prentice-Hall,Inc.,Englewood Cliffs, New Jersey, 1974.

MADARIAGA,R., Dynamics of an expanding circular fault, Bull. Seism. Soc. Am., 66, 639-666, 1976.

MADARIAGA,R., High-frequency radiation from crack (stress-drop) models of earthquake faulting, Geophys. J. R. astr. Soc., 51, 625-652, 1977.

MUELLER,C.S. and E.CRANSWICK, Source parameters from locally recorded aftershocks of the 9 January Miramichi, New Brunswick, earthquake, Bull. Seism. Soc. Am., 75, 337-360, 1985.

MURAMATU,I., A velocity type strong motion seismograph with wide frequency range, Zisin II, 30, 317-338(in Japanese), 1977.

PAPAGEORGIOU,A.S. and K.AKI, A specific barrier model for the quantitative description of inhomogeneous faulting and the prediction of strong ground motion. I. Description of the model, Bull. Seism. Soc. Am., 73, 693-722, 1983a.

PAPAGEORGIOU,A.S. and K.AKI, A specific barrier model for the quantitative description of inhomogeneous faulting and the prediction of strong ground motion. II. Application of the model, Bull. Seism. Soc. Am., 73, 953-978, 1983b.

PAPAGEORGIOU,A.S. and K.AKI, A specific barrier model for the quantitative description of inhomogeneous faulting and the prediction of strong ground motion. I. Description of the model, Erratum, Bull. Seism. Soc. Am., 74, 794-795, 1984.

PAPAGEORGIOU,A.S. and K.AKI, Scaling law of far-field spectra based on observed parameters of the specific barrier model, Pure and Applied Geophysics, 123, 353-374, 1985.

SAITO,M., Possible instability in the Burg maximum entropy method, J. Phys. Earth., 26, 123-128, 1978.

SATO,T., Rupture characteristics of the 1983 Nihonkai-Chubu (Japan Sea) earthquake as inferred from strong motion accelerograms, J. Phys. Earth., 33, 525-557, 1985.

SILVA,W., Body waves in a layered anelastic field, Bull. Seism. Soc. Am., 66, 1539-1554, 1976.

TOHOKU UNIVERSITY and HIROSAKI UNIVERSITY, Foreshock and aftershock activities of the 1983 central Japan Sea earthquake, Rep. Coord. Comm. Earthq. Predict., 31, 22-33(in Japanese), 1984.

YOSHII,T. and S.ASANO, Time-term analysis of explosion seismic data, J. Phys. Earth., 20, 46-58, 1972.

WATANABE,S. ,T.HARYU, S.KUTSUZAWA, and Y.KAJI, The relationship between the phenomenon of liquefaction and the soil condition in the 1983 Nihonkai-Chubu earthquake, Tsuchi-to-Kiso, 320, 35-41(in Japanese), 1984.

Fig. 1(a)

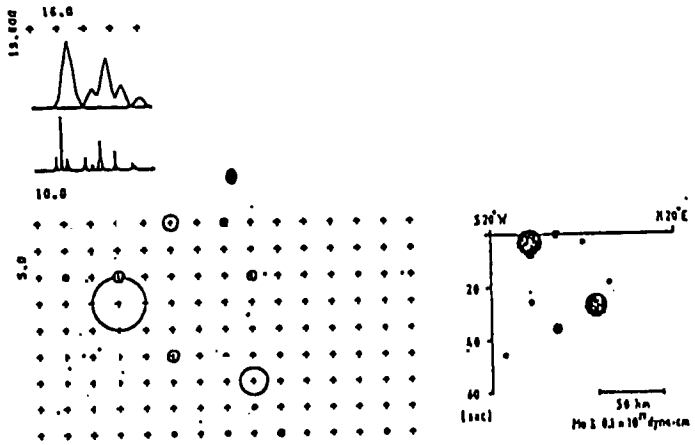

after ISHIKAWA et al.(1984)

Fig. 1(b)

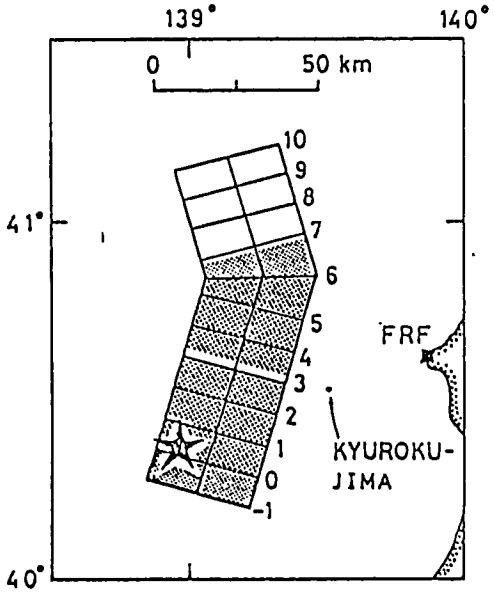

after SATO(1985)

Fig. 1(c)

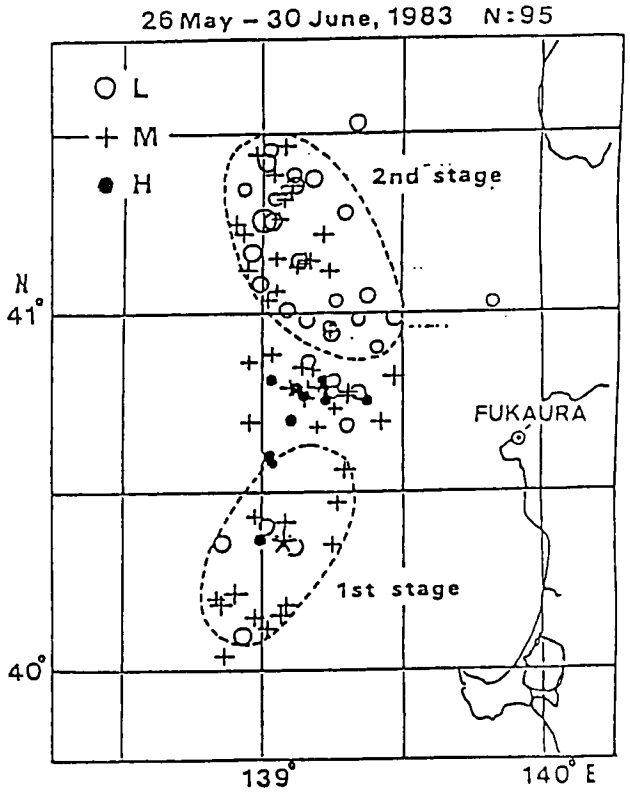

after KUROISO et al.(1986)

Fig. 2

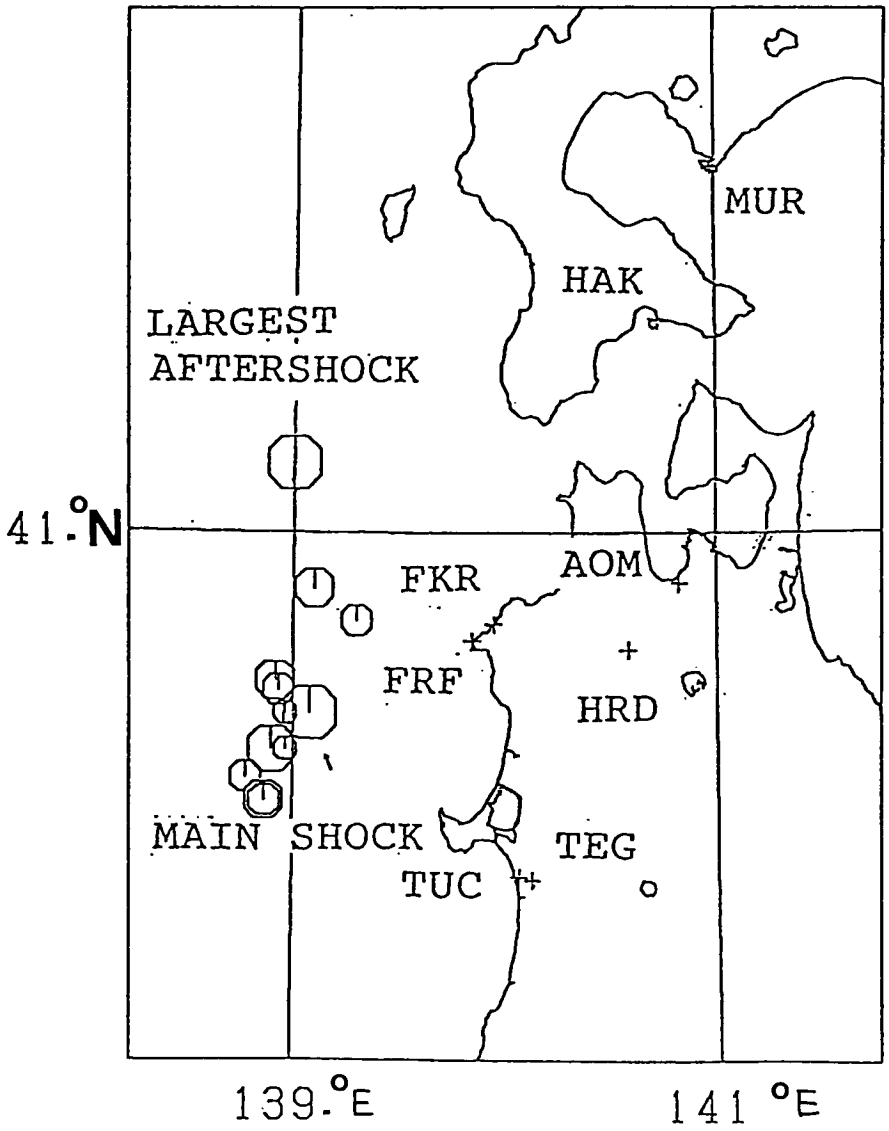
MUR
HAK
LARGEST
AFTERSHOCK
41.°N
FKR
AOM
FRF
HRD
MAIN SHOCK
TEG
TUC
139.°E
141 °E

HIROSAKI UNIV. NS-COMPONENT

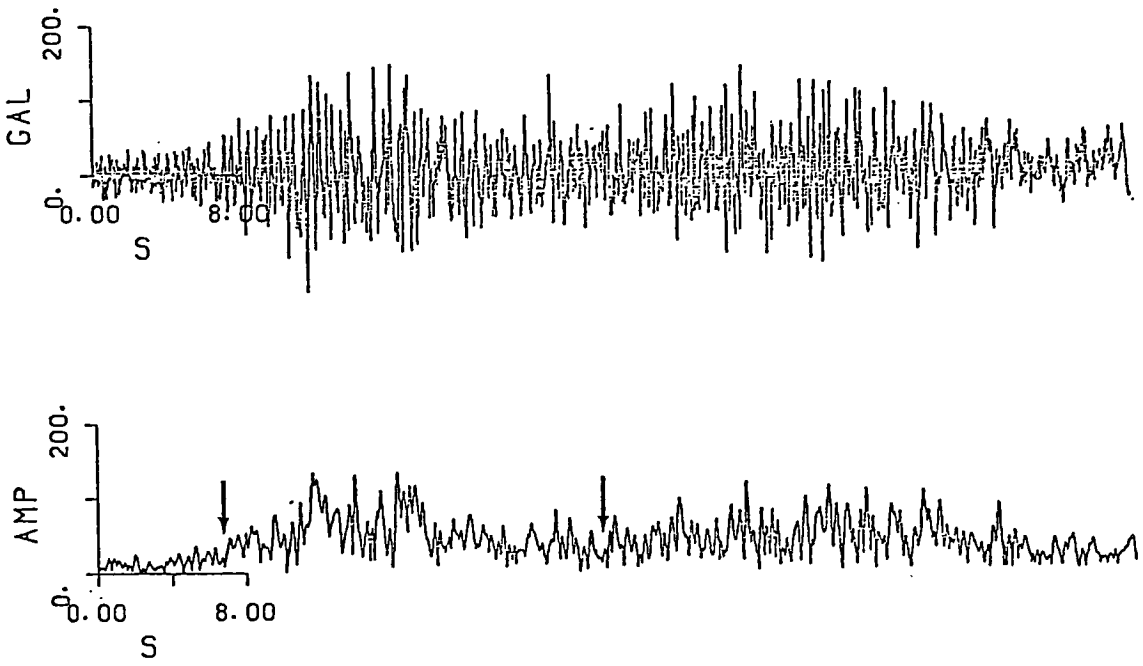

Fig. 3

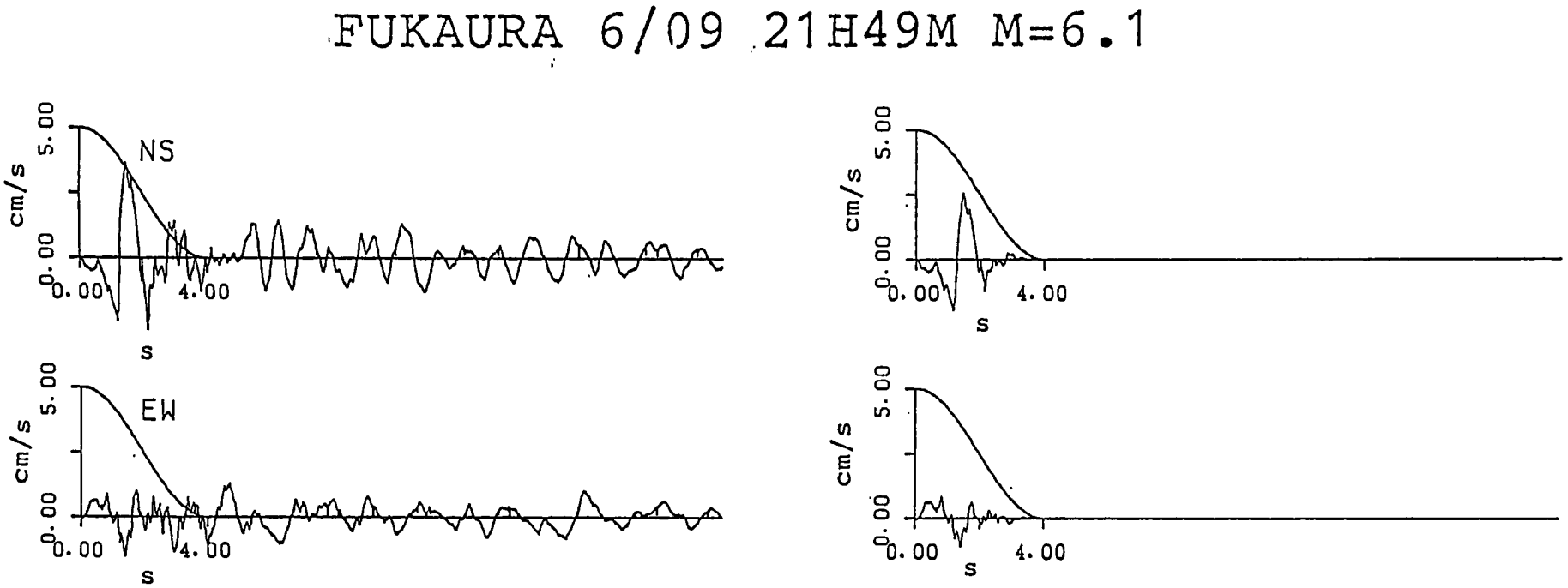

(a)

Fig 4(a)

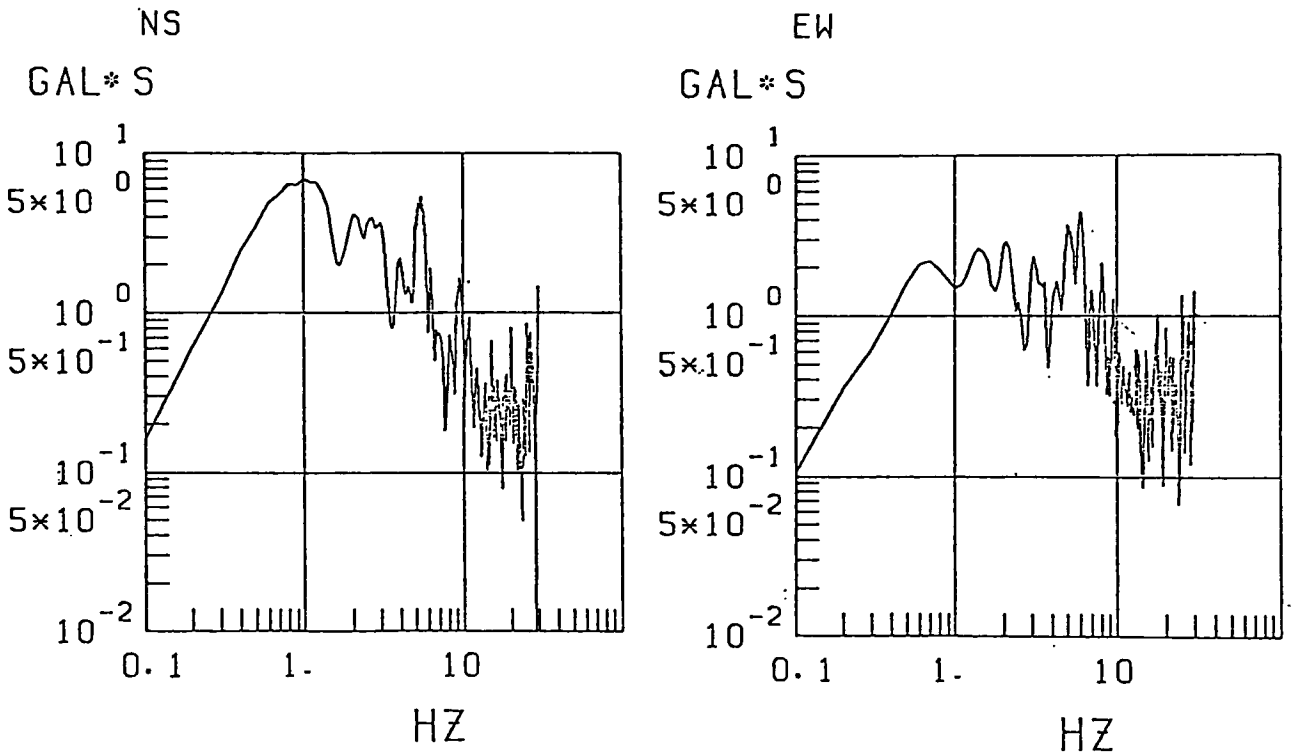
NS
GAL*S
10 1
5×10 0
10 0
5×10⁻¹
10⁻¹
5×10⁻²
10⁻²
0.1
1.
10
HZ
EW
GAL*S
10 1
5×10 0
10 0
5×10⁻¹
10⁻¹
5×10⁻²
10⁻²
0.1
1.
10
HZ

(b)

Fig. 4(b)

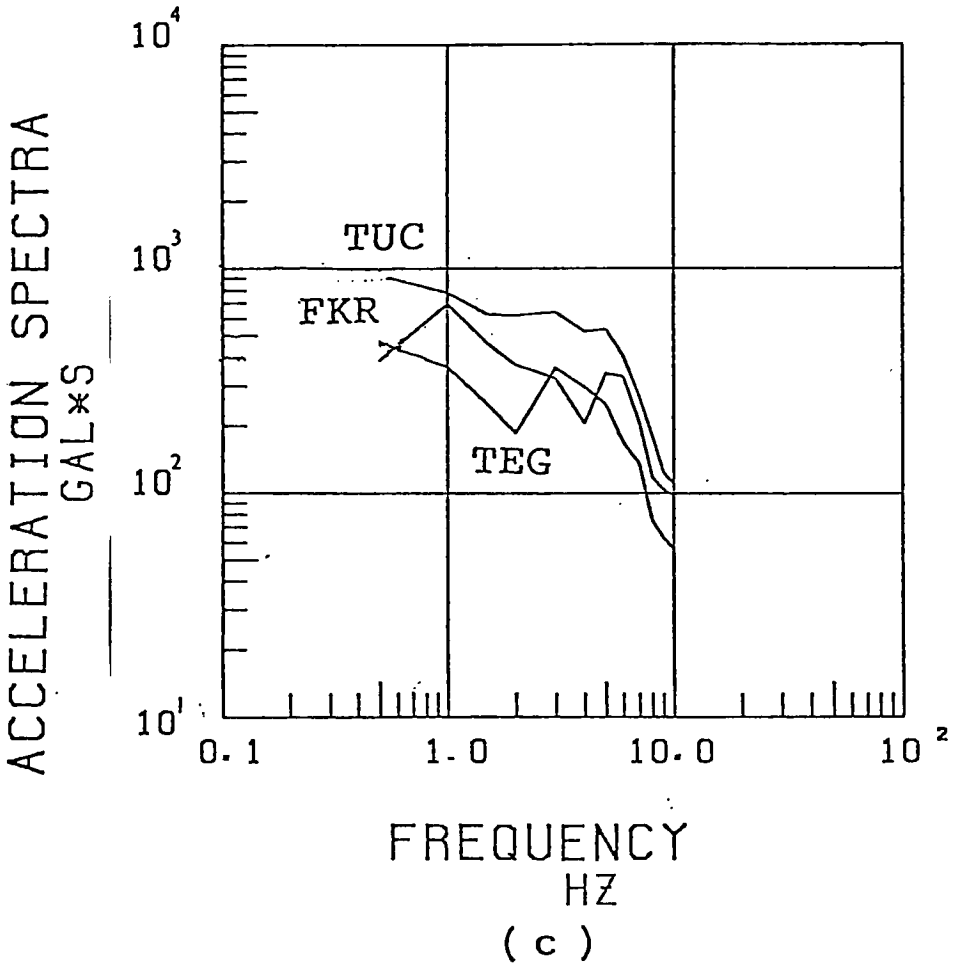
ACCELERATION SPECTRA
GAL*S
10^4
10^3
10^2
10^1
TUC
FKR
TEG
0.1
1.0
10.0
10^2
FREQUENCY
HZ
(c)

Fig 4(c)

Fig. 5

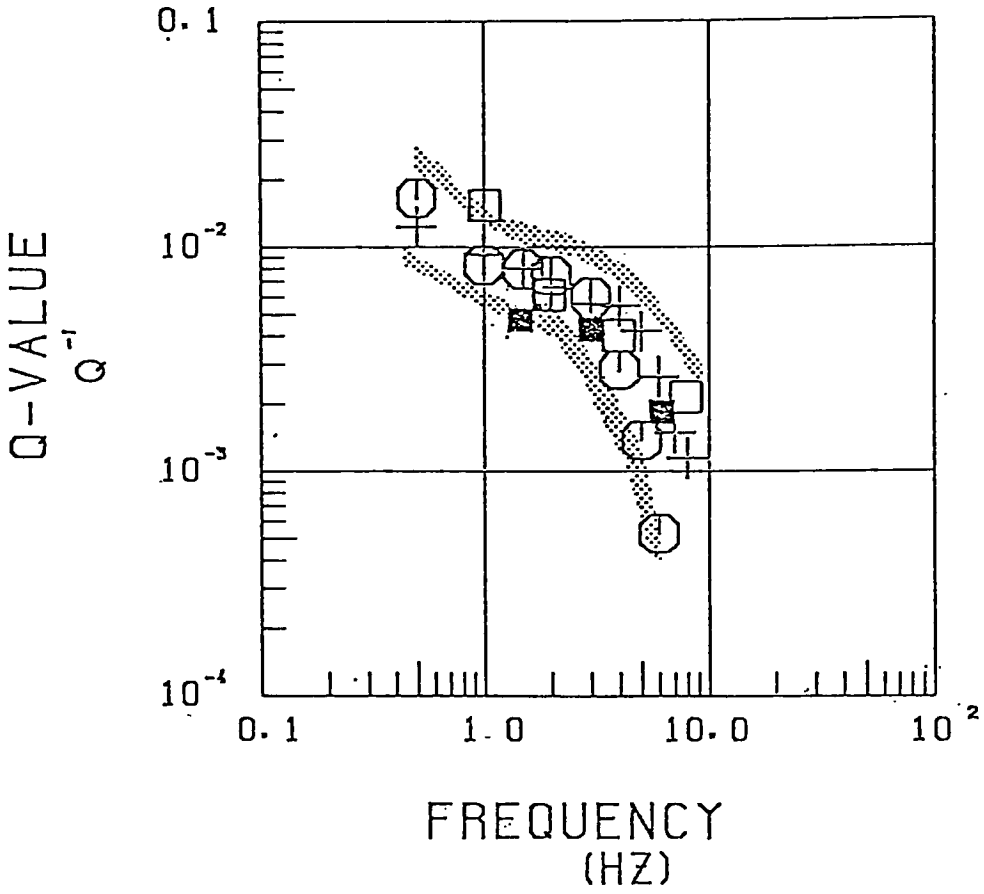

○ S-wave of the main-shock and the largest aftershock
+ S-wave of aftershocks
□ SATO (1983) from the S-wave of the main-shock
■ IDEI (1983) from S-coda wave of aftershocks

Fig. 6

(a)

HAKODATE

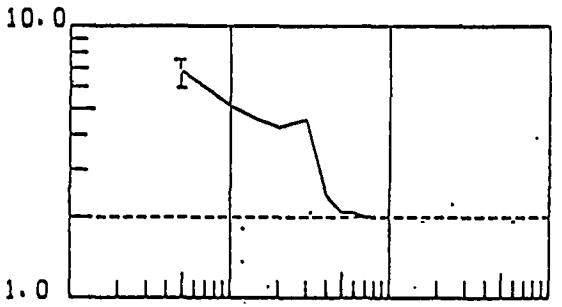

MURORAN

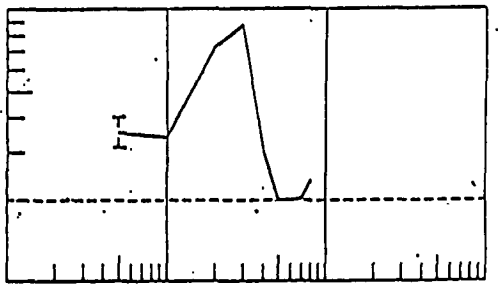

(b)

TSUCHIZAKI

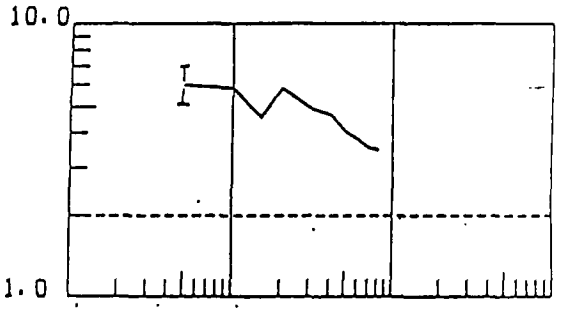

HIROSAKI UNIV.

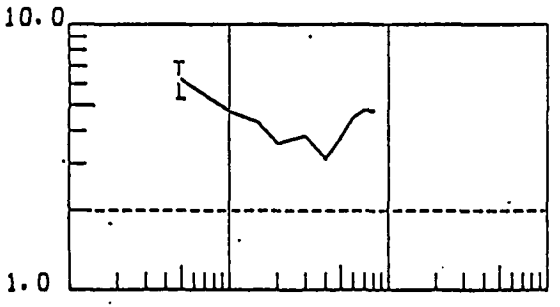

AOMORI.

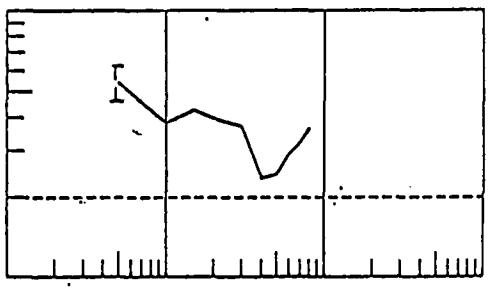

TEGATA

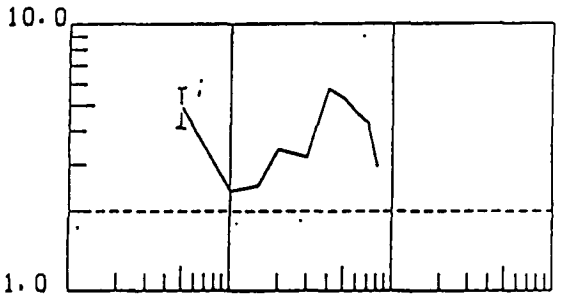

FUROUFUSHI

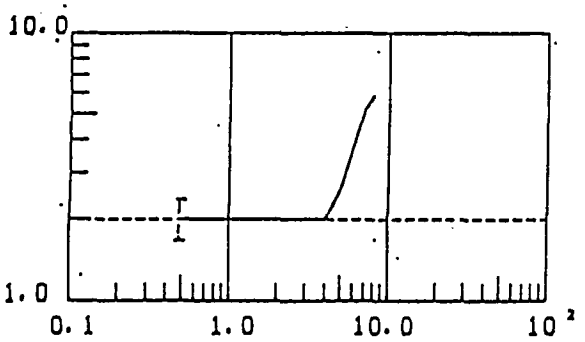

TSUCHIZAKI

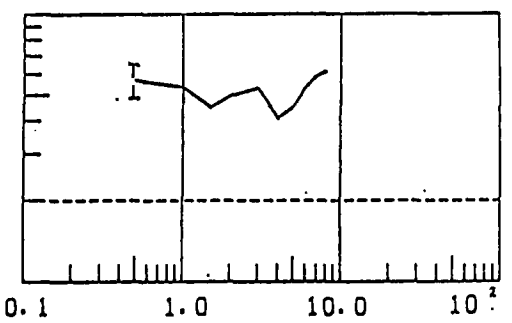

FUKAURA

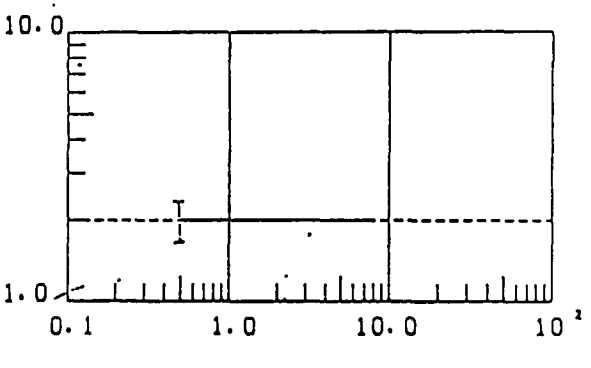

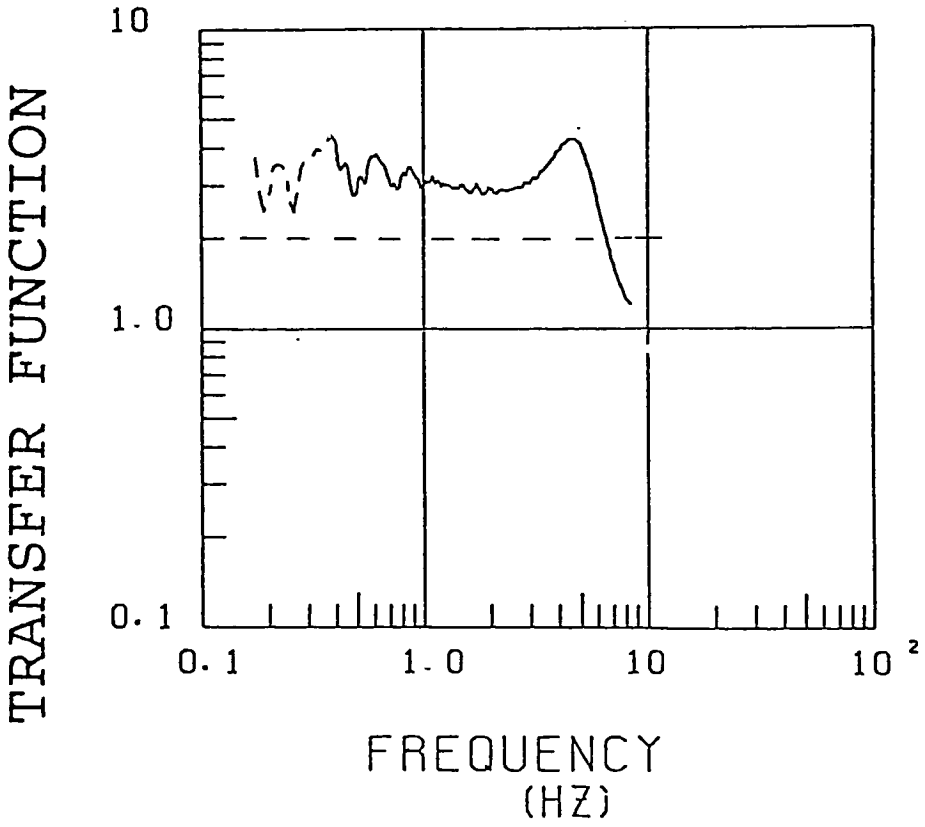

Fig. 7

Fig. 8

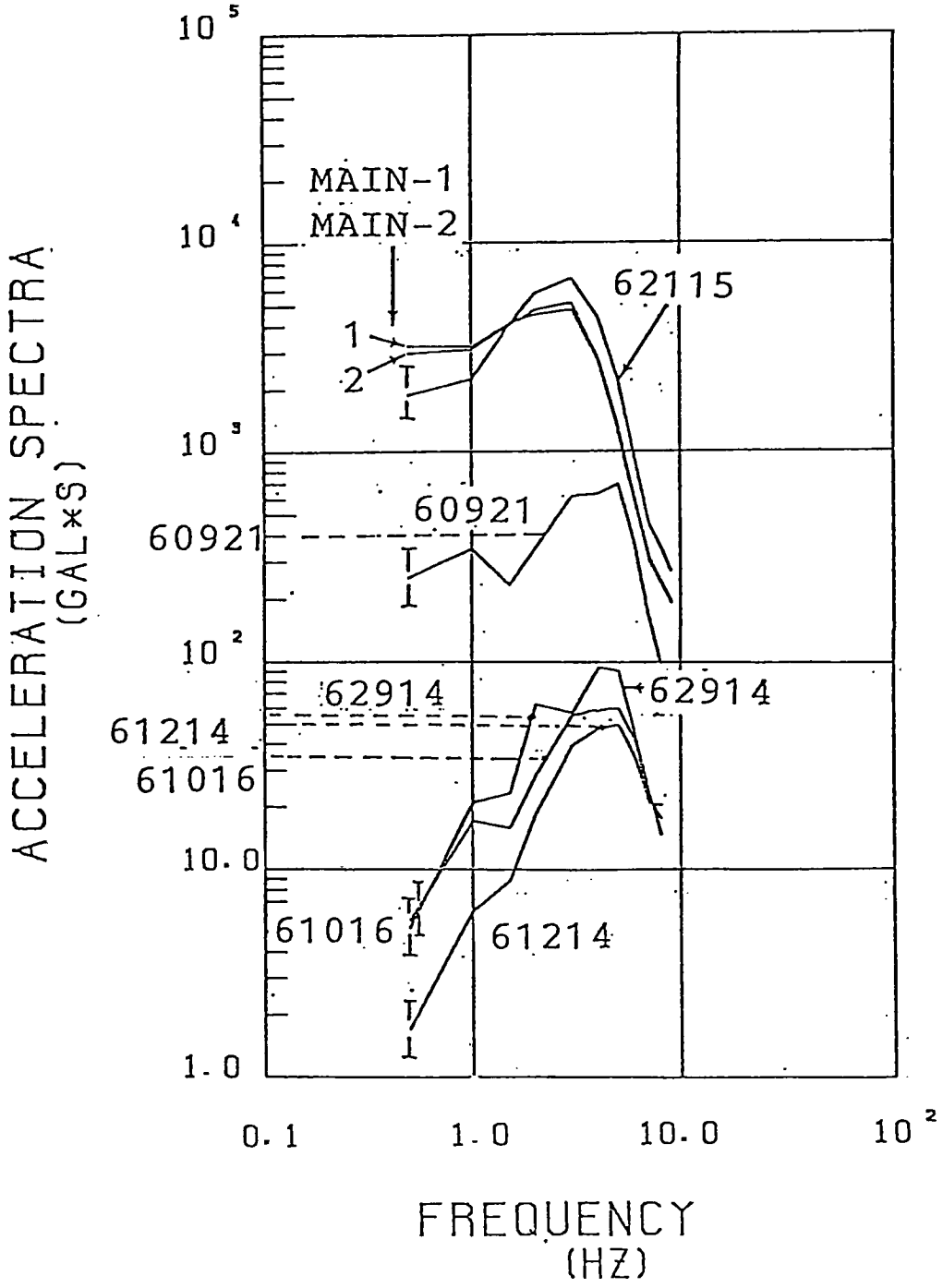
ACCELERATION SPECTRA
(GAL*S)
10 5
10 4
10 3
10 2
10.0
1.0
MAIN-1
MAIN-2
1
2
62115
60921
60921
62914
62914
61214
61016
61016
61214
0.1
1.0
10.0
10 2
FREQUENCY
(HZ)

Fig. 8

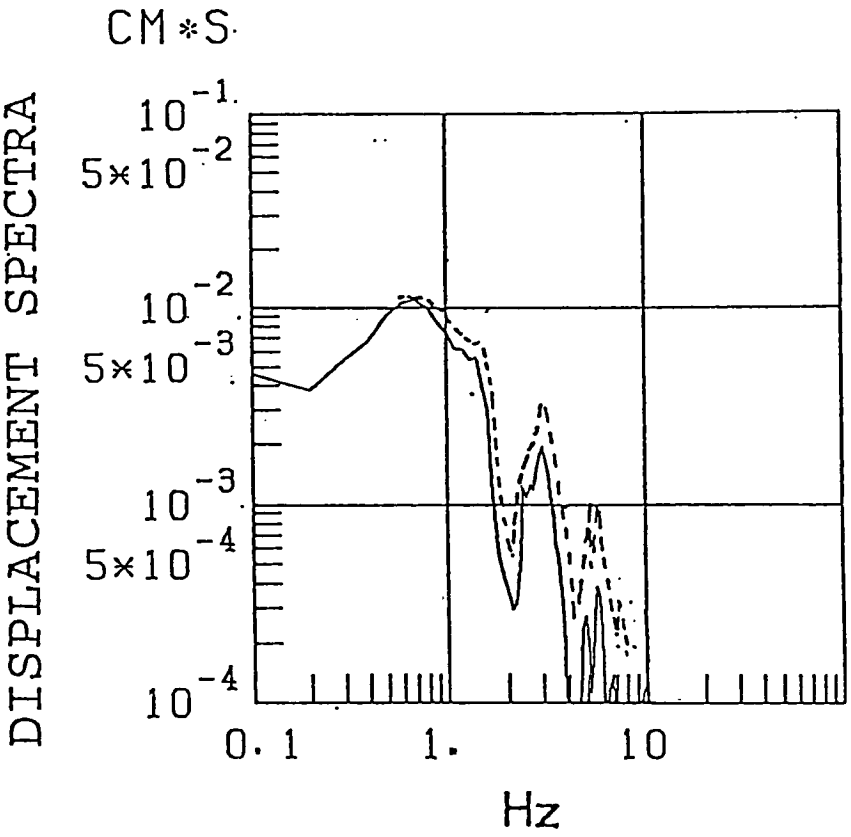
CM*S
DISPLACEMENT SPECTRA
10^-1
5*10^-2
10^-2
5*10^-3
10^-3
5*10^-4
10^-4
0.1
1.
10
Hz

Fig 9 (a)

DISPLACEMENT SPECTRA

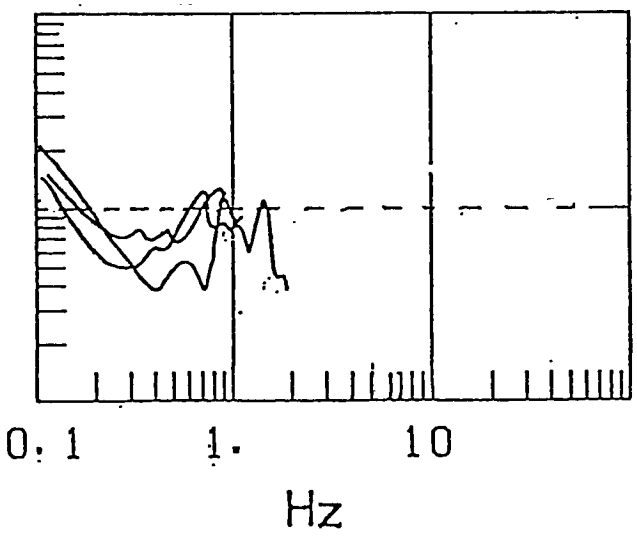

Fig 9(b)

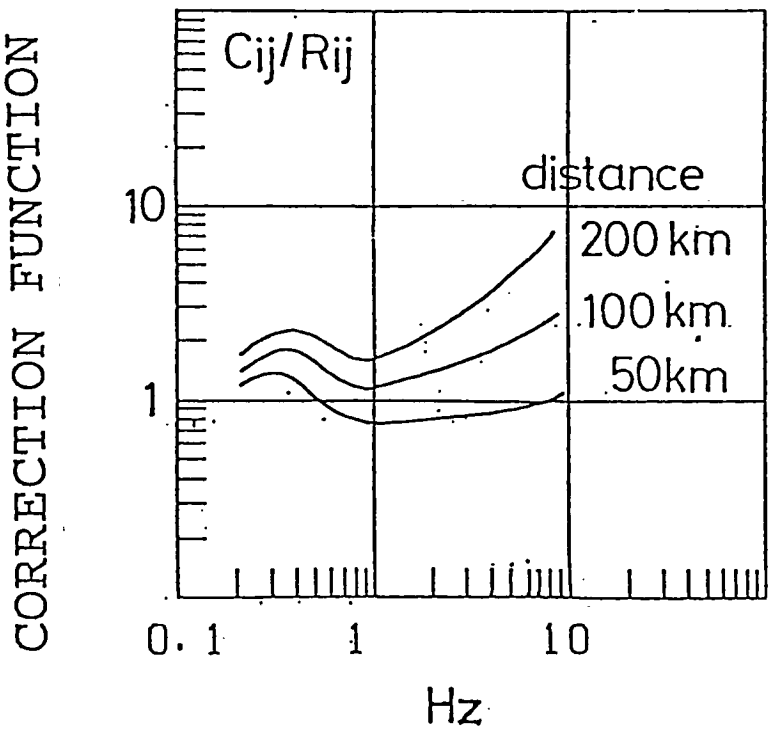
CORRECTION FUNCTION
Cij/Rij
distance
200 km
100 km
50km
10
1
0.1
1
10
Hz

Fig 9(c)

FUKAURA 6/10 16H20M M=5.0

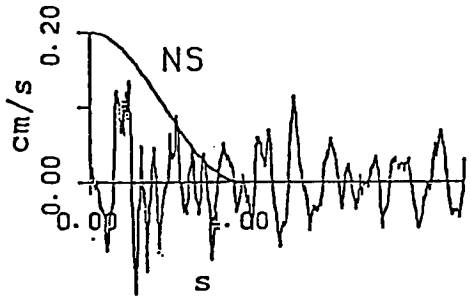

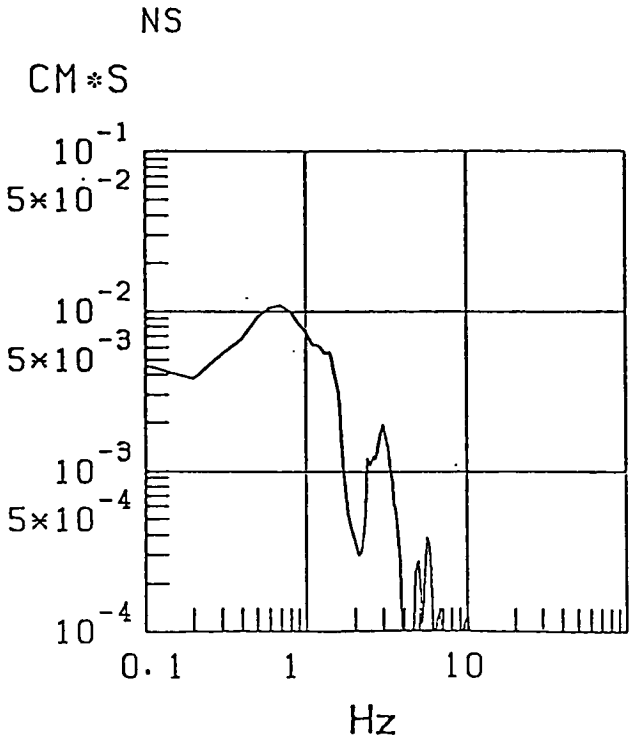

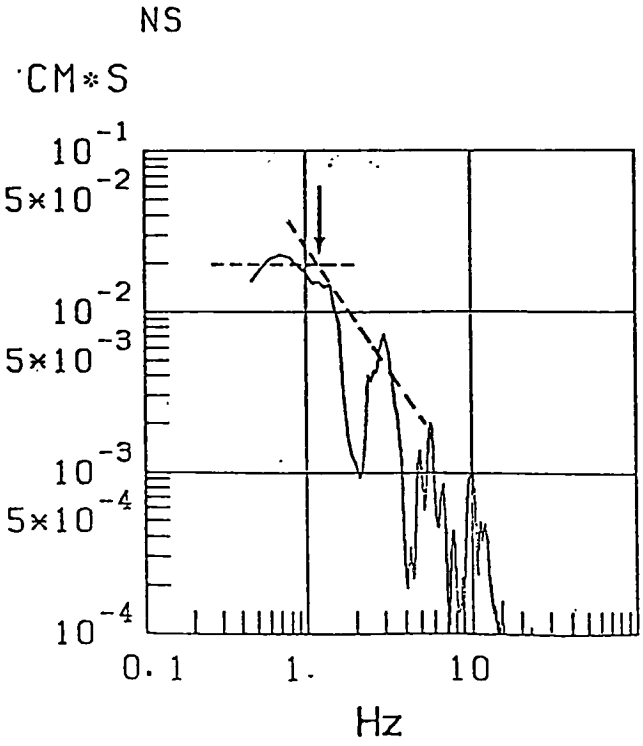

Fig. 10

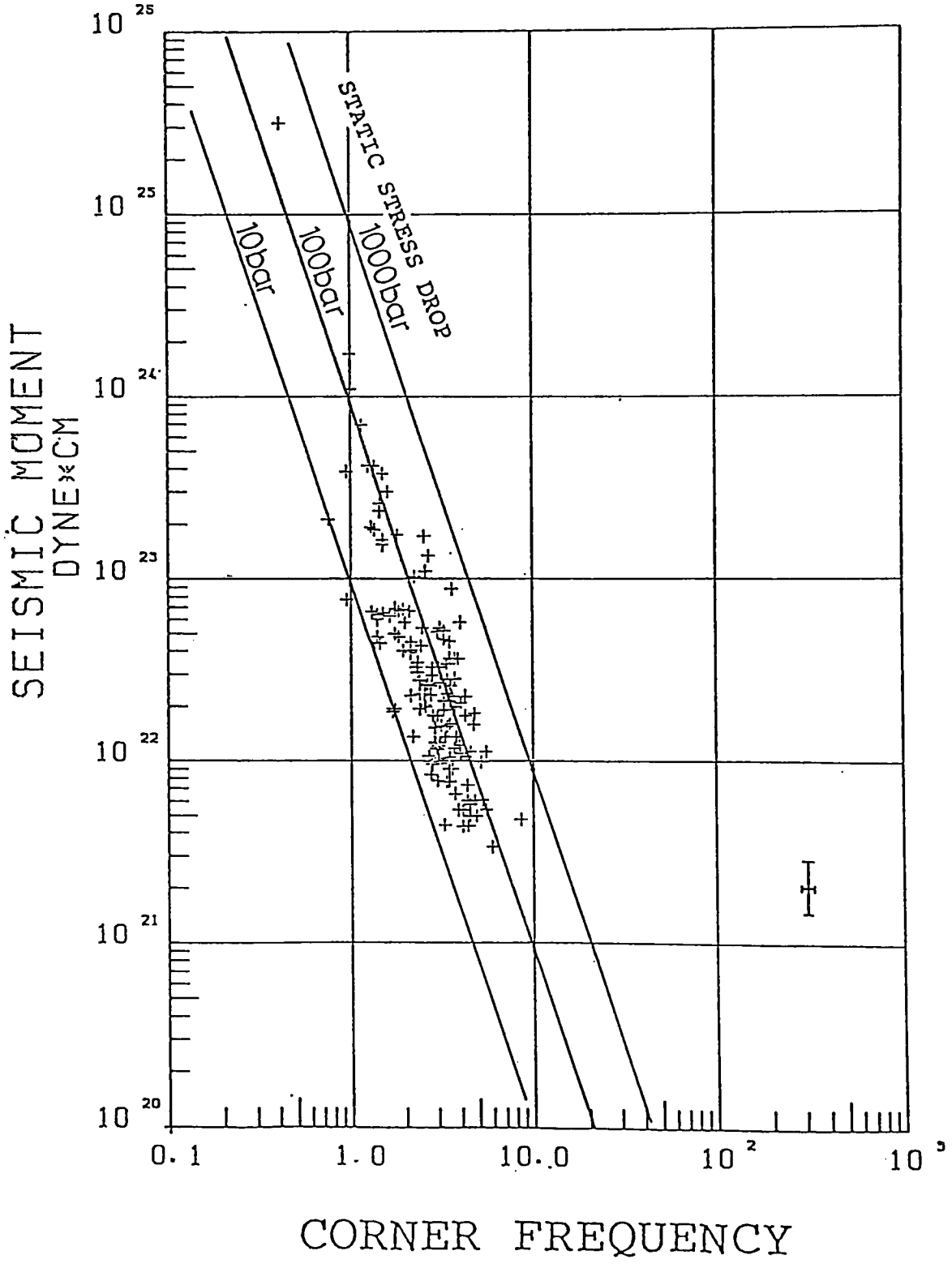
SEISMIC MOMENT
DYNE×CM
10 25
10 25
10 24
10 23
10 22
10 21
10 20
STATIC STRESS DROP
1000bar
100bar
10bar
0.1
1.0
10.0
10 2
10 3
CORNER FREQUENCY

Fig. 11

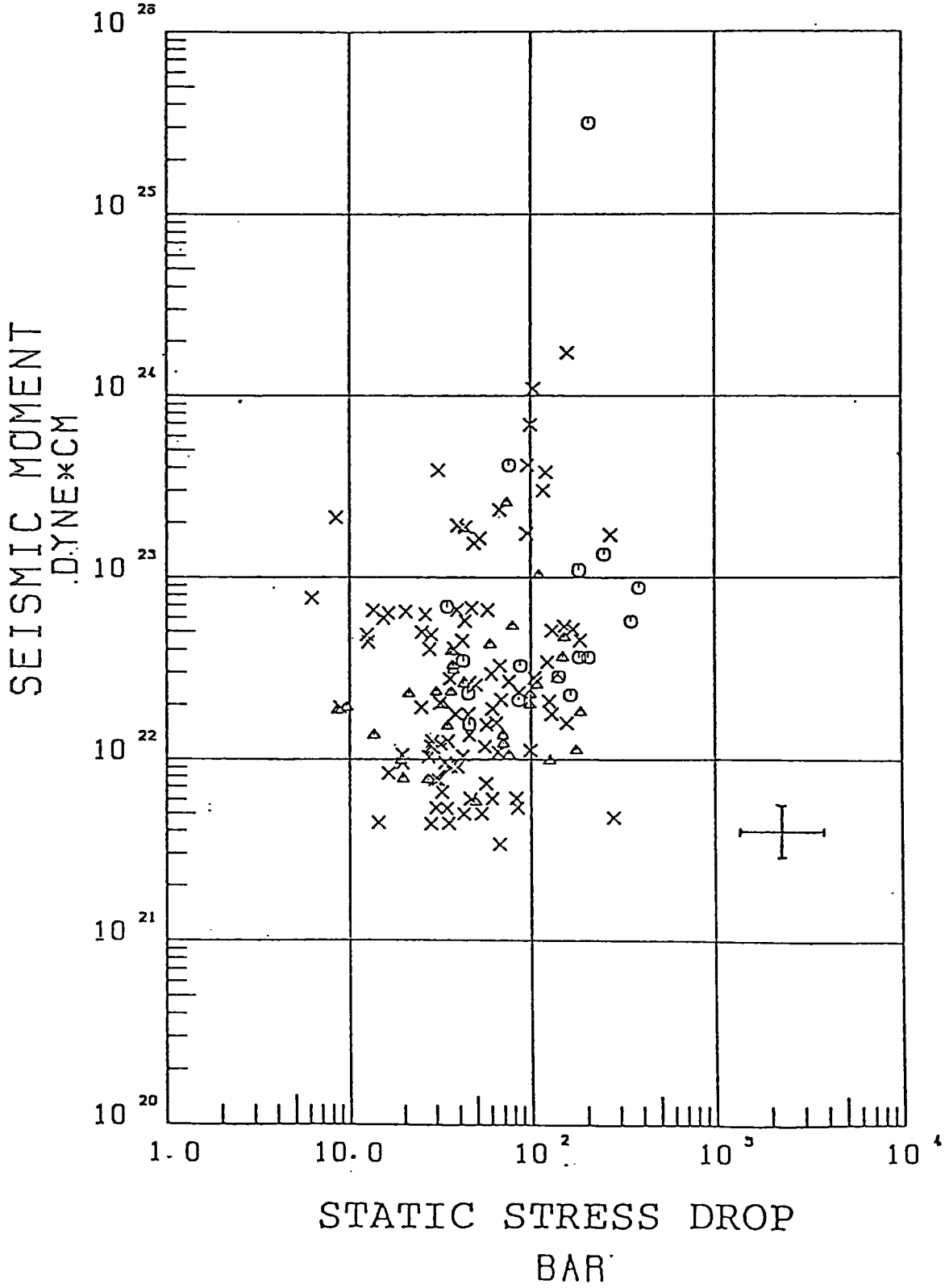
SEISMIC MOMENT
DYNE*CM
10 28
10 25
10 24
10 23
10 22
10 21
10 20
1.0
10.0
10 2
10 3
10 4
STATIC STRESS DROP
BAR

Fig 12 (a)

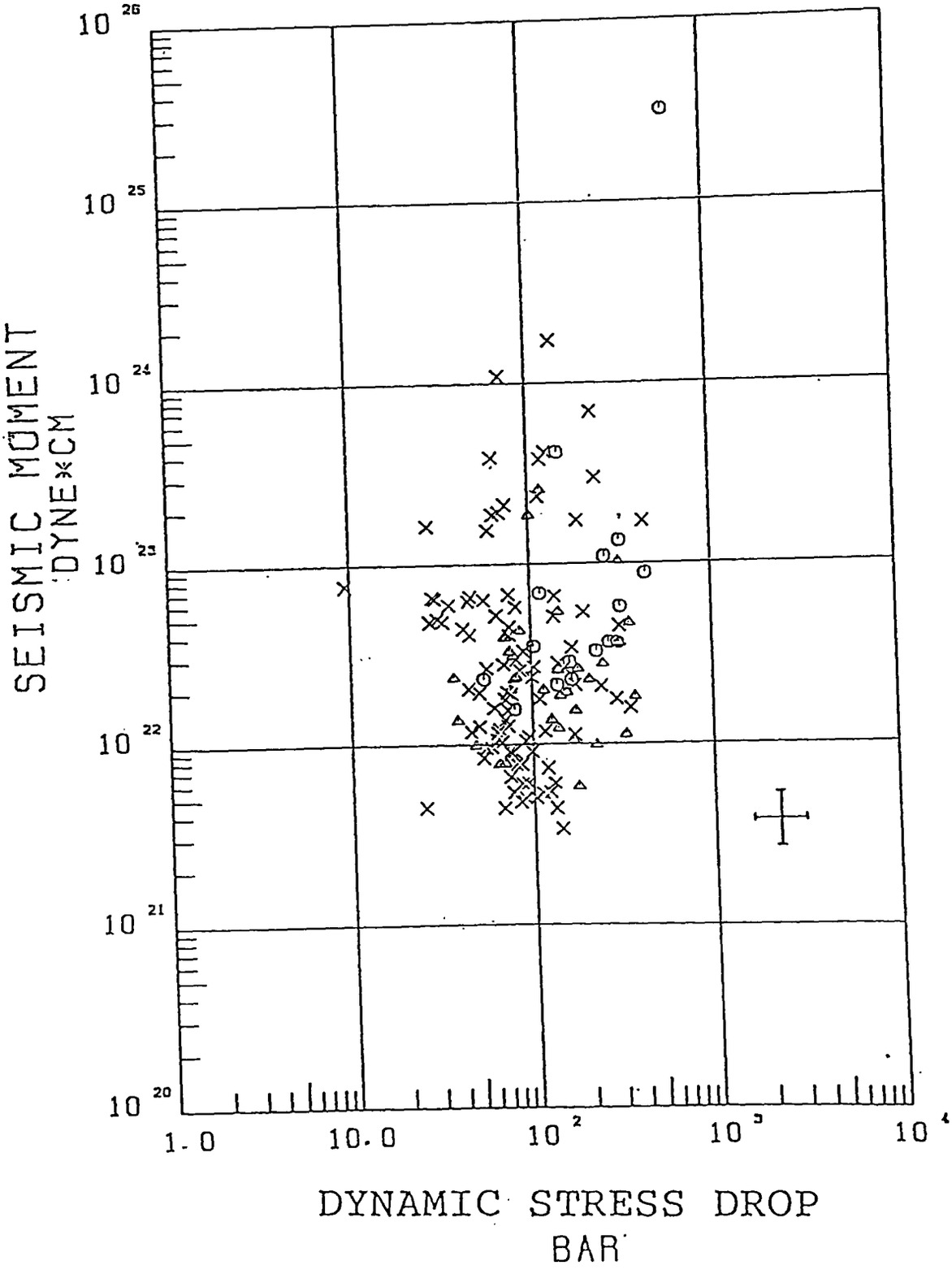
SEISMIC MOMENT
DYNE×CM
10 26
10 25
10 24
10 23
10 22
10 21
10 20
1.0
10.0
10 2
10 3
10 4
DYNAMIC STRESS DROP
BAR

Fig 12(b)

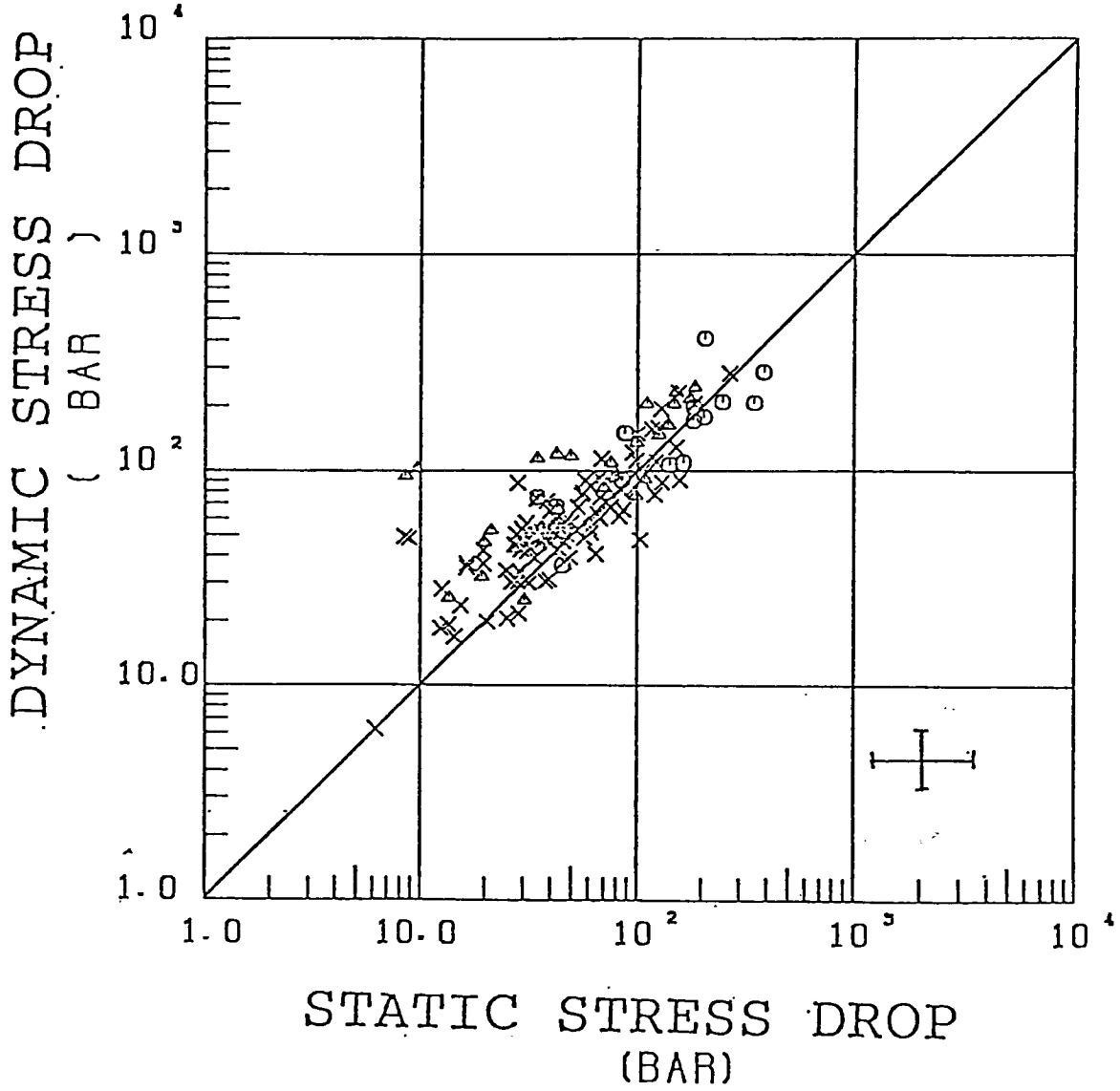

○ A region : aftershock area of M=6.1 and 6.0

△ B region : aftershock area of the main event

× C region : aftershock area of M=7.1

Fig. 13

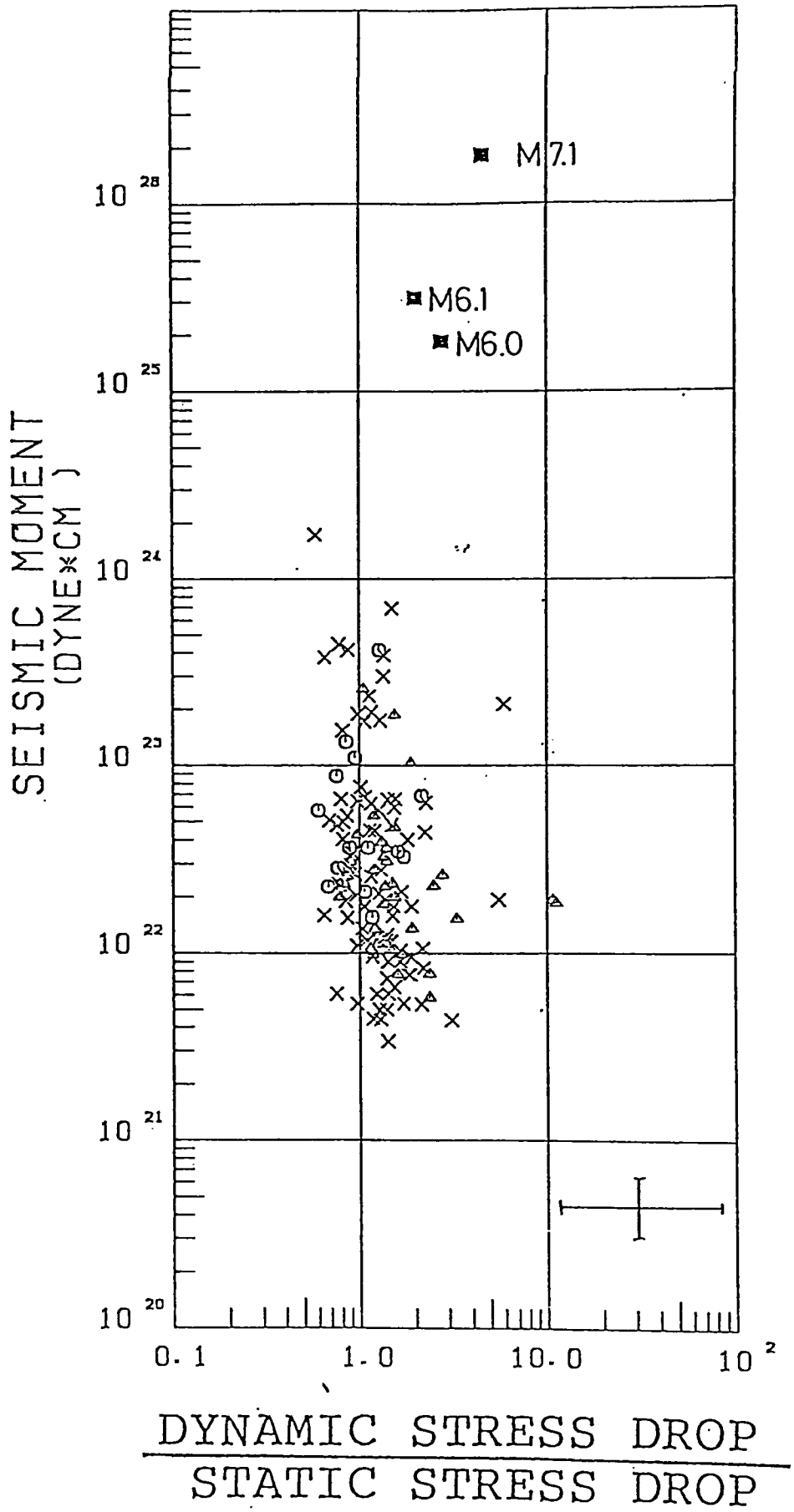

○ A region : aftershock area of M=6.1 and 6.0

△ B region : aftershock area of the main event

× C region : aftershock area of M=7.1

Fig 14

Fig. 15

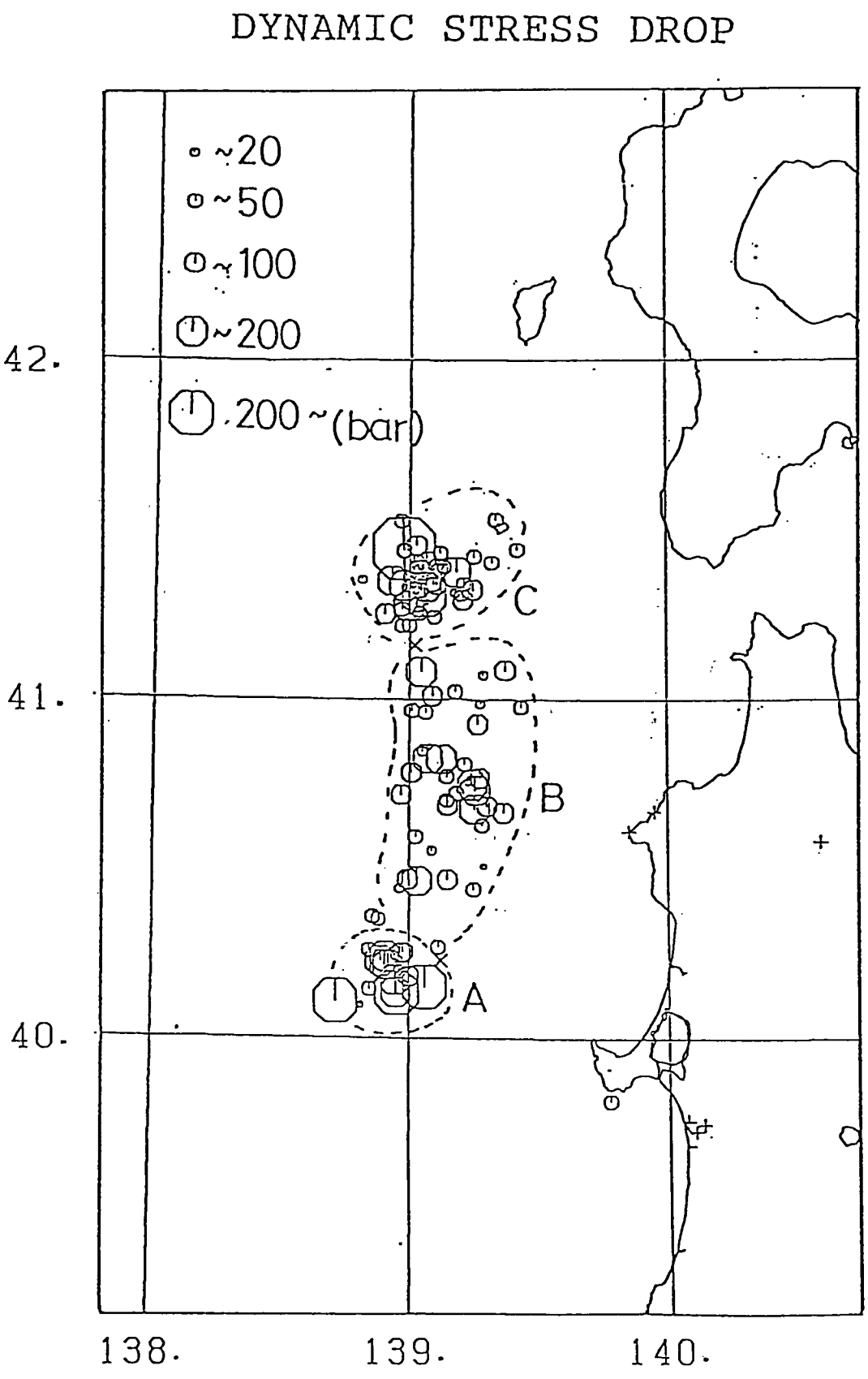
DYNAMIC STRESS DROP
~20
~50
~100
~200
200 ~(bar)
A
B
C
42.
41.
40.
138.
139.
140.

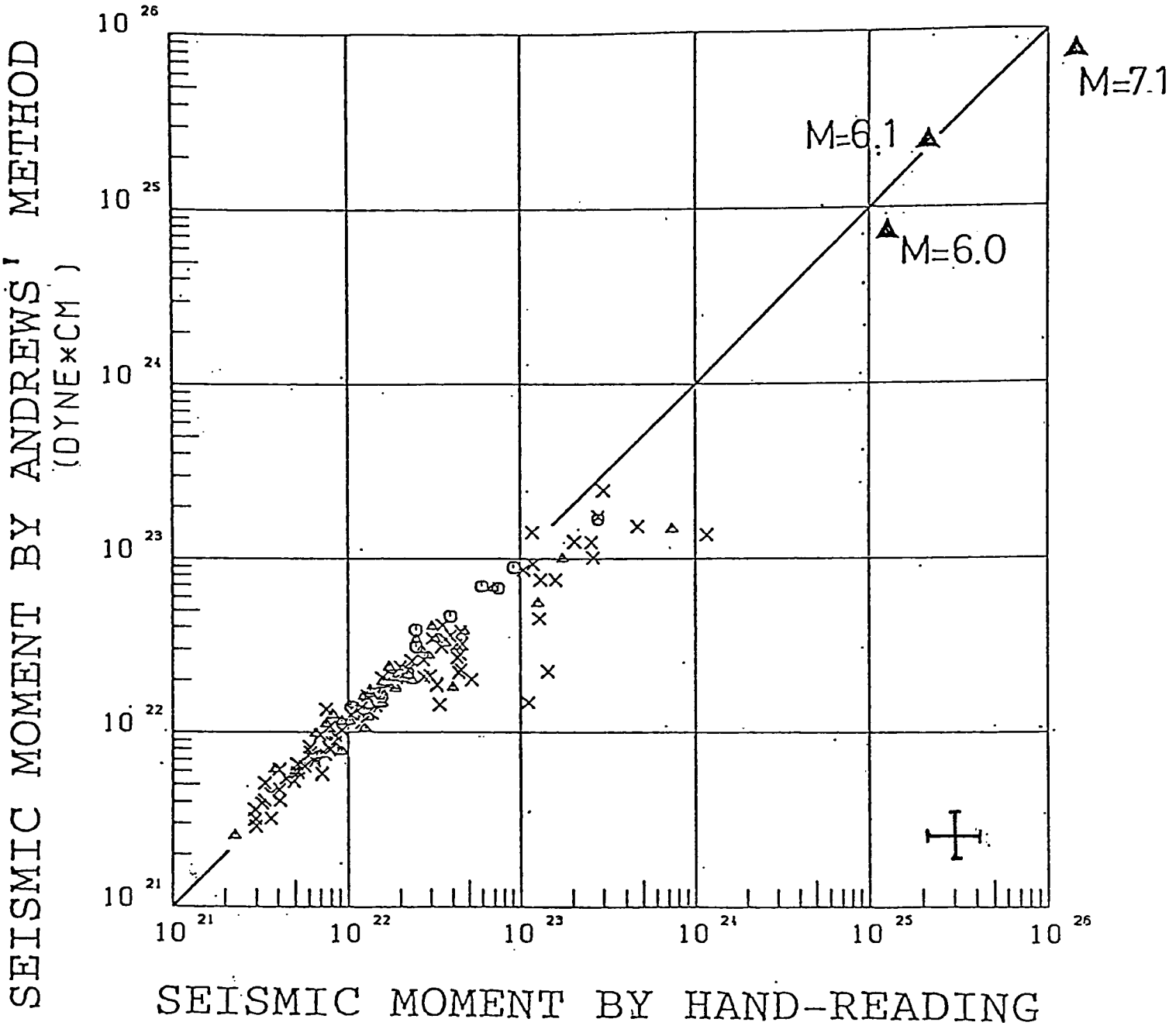

○ A region : aftershock area of M=6.1 and 6.0

△ B region : aftershock area of the main event

× C region : aftershock area of M=7.1

Fig 16(a)

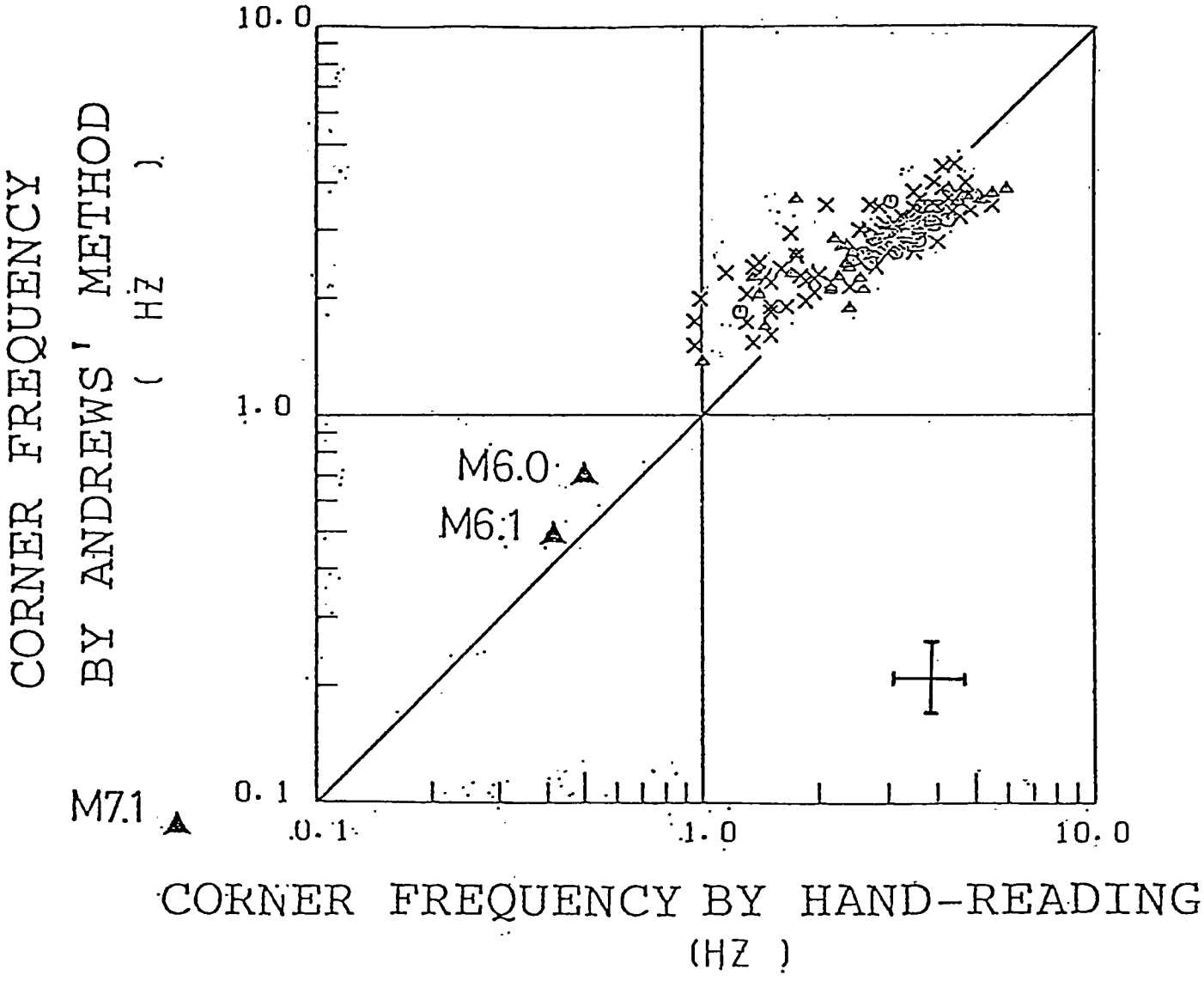

○ A region : aftershock area of M=6.1 and 6.0

△ B region : aftershock area of the main event

× C region : aftershock area of M=7.1

Fig 16 (b)

DATE ('83)	LAT. (d. m.)	LON. (d. m.)	DEP. (km)	MAG. (JMA)
5/26 11:59	40 21	139 05	14	7.7
6/21 15:25	41 16	139 00	6	7.1
6/03 17:22	40 26	138 56	54	5.0
6/04 03:03	40 41	139 18	45	4.2
6/09 13:36	40 02	138 52	35	5.1
6/09 21:49	40 13	138 54	23	6.1
6/10 16:20	40 15	138 58	57	5.0
6/11 15:14	40 02	138 54	18	4.9
6/12 07:01	40 47	139 01	0	4.7
6/12 12:00	40 09	139 04	37	4.3
6/12 14:02	40 13	139 01	42	4.0
6/29 14:11	40 22	138 52	14	5.0

FUKAURA	FKR
TEGATA	TEG
TSUCHIZAKI	TUC
MURORAN	MUR
HAKODATE	HAK
AOMORI	AOM
HIROSAKI UNIV.	HRO
FUROUFUSHI	FRF

Table1

MATERIAL CONSTANTS at TUC				
layer	density (g/cm^3)	thickness (m)	Q-value	S-velocity (km/s)
1	1.85	0.5	7	0.10
2	1.85	3.5	10	0.14
3	1.90	1.0	18	0.23
4	1.75	0.7	15	0.20
5	1.95	2.3	28	0.39
6	1.95	4.0	20	0.30
7	1.95	6.0	30	0.43
8	1.90	2×10^3	100	1.0
9	2.1	8×10^3	100	1.4
10	2.5	----	200	3.5

Table 2

Date			Seismic moment		Stress drop		Corner frequency		Stress drop ratio
	(h)	(min)	Andrews' M_0 (dyn·cm)	M_0 (dyn·cm)	$\Delta\sigma_D$ (bar)	$\Delta\sigma_S$ (bar)	Andrews' f_0 (Hz)	f_0 (Hz)	$\Delta\sigma_D/\Delta\sigma_S$
1 Jun.	17	19	0.997E+22	0.988E+22	32.2	19.2	2.59	2.75	1.681
1 Jun.	19	41	0.223E+23	0.199E+23	76.7	97.9	3.11	3.75	0.783
1 Jun.	21	06	0.781E+22	0.772E+22	43.3	27.1	2.90	3.35	1.602
1 Jun.	22	01	0.155E+23	0.152E+23	114.3	34.6	2.97	2.90	3.301
2 Jun.	00	44	0.150E+23	0.112E+23	216.8	174.0	3.73	5.50	1.246
2 Jun.	04	29	0.624E+23	0.579E+23	207.0	345.4	3.44	4.00	0.599
2 Jun.	03	26	0.545E+23	0.454E+23	205.0	181.6	2.68	3.50	1.129
2 Jun.	09	40	0.342E+23	0.345E+23	110.5	121.0	2.81	3.35	0.913
2 Jun.	10	48	0.224E+23	0.227E+23	135.6	98.8	3.00	3.60	1.373
2 Jun.	12	50	0.103E+23	0.908E+22	65.2	39.5	3.58	3.60	1.650
2 Jun.	14	31	0.317E+23	0.257E+23	91.9	107.4	2.69	3.55	0.855
3 Jun.	04	27	0.682E+22	0.501E+22	67.6	53.3	3.36	4.85	1.268
3 Jun.	08	48	0.133E+23	0.984E+22	147.2	125.3	3.59	5.15	1.175
3 Jun.	14	43	0.455E+23	0.367E+23	205.0	146.8	2.88	3.50	1.397
3 Jun.	16	23	0.263E+23	0.235E+23	54.4	36.3	2.26	2.55	1.497
3 Jun.	20	44	0.192E+23	0.229E+23	52.9	21.3	2.13	2.15	2.488
3 Jun.	23	09	0.524E+22	0.480E+22	56.1	274.9	3.48	8.50	0.204
4 Jun.	03	04	0.911E+23	0.103E+24	205.9	109.2	2.28	2.25	1.884
4 Jun.	07	19	0.805E+22	0.780E+22	46.6	19.6	2.99	3.00	2.371
4 Jun.	08	30	0.627E+22	0.606E+22	86.0	60.5	3.68	4.75	1.421
4 Jun.	11	24	0.958E+22	0.954E+22	36.9	19.5	2.40	2.80	1.891
4 Jun.	13	56	0.462E+23	0.469E+23	232.2	150.3	2.85	3.25	1.546
4 Jun.	16	17	0.252E+23	0.261E+23	118.9	42.7	3.01	2.60	2.784
4 Jun.	17	44	0.591E+22	0.537E+22	73.9	34.5	3.84	4.10	2.139
4 Jun.	22	03	0.225E+23	0.208E+23	158.3	124.4	3.43	4.00	1.273
5 Jun.	00	13	0.700E+22	0.734E+22	78.8	56.3	3.68	4.35	1.398
5 Jun.	00	57	0.825E+22	0.579E+22	116.4	49.2	3.54	4.50	2.368
5 Jun.	04	24	0.266E+23	0.349E+23	68.0	42.3	2.74	2.35	1.608
5 Jun.	07	32	0.164E+23	0.193E+23	102.5	9.7	3.61	1.75	10.614
5 Jun.	13	12	0.349E+23	0.403E+23	50.5	27.9	2.06	1.95	1.812
5 Jun.	17	59	0.291E+23	0.328E+23	150.2	86.9	3.54	3.05	1.728
6 Jun.	01	12	0.417E+23	0.367E+23	200.1	180.5	3.21	3.75	1.108
6 Jun.	07	30	0.199E+23	0.235E+23	24.8	30.3	1.88	2.40	0.821
6 Jun.	10	23	0.543E+22	0.610E+22	61.5	82.3	3.67	5.25	0.747
6 Jun.	15	33	0.246E+23	0.280E+23	163.7	137.6	3.24	3.75	1.189
6 Jun.	16	04	0.436E+23	0.541E+23	94.3	78.9	2.48	2.50	1.195
6 Jun.	20	27	0.387E+22	0.447E+22	16.8	14.3	2.89	3.25	1.174
7 Jun.	04	25	0.481E+22	0.440E+22	87.5	28.3	4.36	4.10	3.094
7 Jun.	11	25	0.186E+23	0.178E+23	194.4	127.5	3.62	4.25	1.524
7 Jun.	15	07	0.170E+23	0.122E+23	91.4	70.0	3.15	3.95	1.306
8 Jun.	04	06	0.234E+23	0.199E+23	50.6	32.6	2.11	2.60	1.550
8 Jun.	12	11	0.727E+22	0.660E+22	49.5	32.5	2.92	3.75	1.523
8 Jun.	15	22	0.186E+23	0.159E+23	231.6	154.0	3.98	4.70	1.503
9 Jun.	04	29	0.370E+23	0.431E+23	57.4	59.2	2.62	2.45	0.970
9 Jun.	06	39	0.593E+22	0.541E+22	51.5	30.0	3.97	3.90	1.718
9 Jun.	14	17	0.819E+22	0.606E+22	57.4	46.5	3.34	4.35	1.234
9 Jun.	14	18	0.400E+23	0.393E+23	48.0	36.5	2.09	2.15	1.317
9 Jun.	15	58	0.156E+23	0.136E+23	83.7	69.8	3.13	3.80	1.199
9 Jun.	22	16	0.517E+23	0.366E+23	178.4	202.5	3.09	3.90	0.881
9 Jun.	22	52	0.507E+23	0.694E+23	75.0	34.7	2.59	1.75	2.162
9 Jun.	22	59	0.282E+23	0.286E+23	107.2	140.6	3.44	3.75	0.762
9 Jun.	23	41	0.903E+23	0.110E+24	171.5	181.1	2.60	2.60	0.947
10 Jun.	03	32	0.956E+22	0.908E+22	49.3	34.8	3.10	3.45	1.418
10 Jun.	08	28	0.224E+23	0.227E+23	110.0	162.5	3.17	4.25	0.677
10 Jun.	13	34	0.541E+22	0.501E+22	59.4	42.6	3.67	4.50	1.395
10 Jun.	14	43	0.106E+23	0.118E+23	30.5	28.1	3.09	2.95	1.085
10 Jun.	16	20	0.226E+24	0.416E+24	97.0	75.9	1.84	1.25	1.279
10 Jun.	17	08	0.222E+23	0.213E+23	90.6	85.4	2.99	3.50	1.061
10 Jun.	19	59	0.785E+22	0.105E+23	60.4	42.0	3.76	3.50	1.439
12 Jun.	07	01	0.133E+24	0.260E+24	77.4	73.8	1.69	1.45	1.048
12 Jun.	12	00	0.932E+23	0.881E+23	288.9	383.5	2.82	3.60	0.753
12 Jun.	15	14	0.174E+23	0.193E+23	48.6	8.8	2.94	1.70	5.497
16 Jun.	22	54	0.153E+23	0.178E+23	72.4	38.5	3.42	2.85	1.884
17 Jun.	07	45	0.426E+22	0.444E+22	45.5	35.3	4.45	4.40	1.291
18 Jun.	21	50	0.142E+23	0.186E+23	94.6	8.5	2.31	1.70	11.126
19 Jun.	13	36	0.119E+24	0.135E+24	209.6	248.3	2.47	2.70	0.844
20 Jun.	11	43	0.197E+24	0.110E+25	47.7	102.3	1.38	1.00	0.466
11 Jun.	12	44	0.239E+23	0.278E+23	46.7	35.8	2.40	2.40	1.303
21 Jun.	16	04	0.183E+24	0.173E+25	90.6	156.5	1.99	0.99	0.579
21 Jun.	16	09	0.307E+23	0.328E+23	59.7	67.3	2.93	2.80	0.888
21 Jun.	16	10	0.274E+23	0.235E+23	66.1	86.0	2.75	3.40	0.769
21 Jun.	16	20	0.329E+24	0.447E+24	962.6	1,243.1	2.96	3.10	0.774
21 Jun.	16	24	0.180E+23	0.194E+23	34.3	25.0	2.14	2.40	1.373
21 Jun.	16	26	0.138E+23	0.136E+23	47.2	45.7	2.93	3.30	1.032
21 Jun.	16	39	0.294E+23	0.651E+23	19.8	20.5	1.84	1.50	0.966
21 Jun.	16	41	0.101E+24	0.193E+24	45.7	39.5	2.04	1.30	1.156
21 Jun.	16	44	0.190E+24	0.173E+24	284.8	267.5	2.99	2.55	1.065
21 Jun.	16	58	0.432E+23	0.682E+23	50.5	47.2	2.25	1.95	1.070
21 Jun.	17	15	0.308E+23	0.666E+23	90.0	57.5	3.46	2.10	1.565
21 Jun.	17	27	0.110E+23	0.116E+23	42.9	29.1	2.89	3.00	1.471
21 Jun.	18	12	0.605E+23	0.190E+24	42.5	43.5	2.40	1.35	0.977
21 Jun.	18	13	0.234E+24	0.416E+24	83.0	95.6	1.54	1.35	0.869
21 Jun.	18	32	0.248E+23	0.483E+23	21.7	28.5	2.22	1.85	0.761
21 Jun.	18	44	0.481E+23	0.580E+23	54.9	43.3	2.31	2.00	1.269
21 Jun.	19	16	0.167E+24	0.303E+24	155.6	115.7	2.38	1.60	1.345
21 Jun.	19	42	0.417E+23	0.513E+23	88.5	129.3	2.60	3.00	0.685
21 Jun.	20	23	0.269E+23	0.772E+23	6.3	6.2	1.51	0.95	1.016
21 Jun.	20	30	0.205E+24	0.697E+24	148.8	98.9	2.31	1.15	1.505

Table 3-1

Date			Seismic moment		Stress drop		Corner frequency		Stress drop ratio
	(h)	(min)	Andrews' M_0 (dyn·cm)	M_0 (dyn·cm)	$\Delta\sigma_D$ (bar)	$\Delta\sigma_S$ (bar)	Andrews' f_0 (Hz)	f_0 (Hz)	$\Delta\sigma_D/\Delta\sigma_S$
21 Jun.	20	39	0.254E+23	0.483E+23	18.5	12.4	2.33	1.40	1.496
21 Jun.	21	18	0.129E+23	0.103E+23	45.0	27.2	2.66	3.05	1.652
21 Jun.	21	26	0.169E+23	0.178E+23	47.2	44.9	2.81	3.00	1.053
21 Jun.	21	32	0.785E+22	0.772E+22	53.6	29.6	3.10	3.45	1.812
21 Jun.	21	34	0.192E+23	0.502E+23	20.5	25.1	2.57	1.75	0.818
21 Jun.	21	41	0.110E+23	0.907E+22	51.6	36.3	3.16	3.50	1.424
22 Jun.	00	00	0.100E+23	0.110E+23	63.0	65.6	2.79	4.00	0.959
22 Jun.	00	15	0.182E+23	0.112E+23	112.0	98.3	3.24	4.55	1.139
21 Jun.	23	32	0.216E+23	0.191E+23	51.2	61.2	2.80	3.25	0.836
23 Jun.	23	34	0.262E+23	0.257E+23	57.4	49.9	2.68	2.75	1.149
23 Jun.	23	49	0.278E+23	0.265E+23	100.0	105.9	2.98	3.50	0.945
22 Jun.	00	02	0.360E+23	0.636E+23	36.9	16.3	2.46	1.40	2.269
22 Jun.	00	20	0.283E+23	0.444E+23	28.2	12.6	2.25	1.45	2.234
22 Jun.	01	02	0.135E+24	0.389E+24	42.4	31.1	1.74	0.95	1.364
22 Jun.	01	10	0.118E+23	0.126E+23	48.8	34.9	3.04	3.10	1.397
22 Jun.	01	22	0.124E+24	0.175E+24	122.5	95.0	2.28	1.80	1.290
22 Jun.	01	34	0.199E+23	0.165E+24	18.4	51.9	2.19	1.50	0.355
22 Jun.	01	50	0.178E+23	0.160E+23	41.0	63.9	2.62	3.50	0.642
22 Jun.	02	20	0.172E+23	0.205E+23	29.9	31.6	2.48	2.55	0.944
22 Jun.	03	15	0.275E+23	0.281E+23	91.9	103.0	3.19	3.40	0.892
22 Jun.	03	26	0.170E+23	0.154E+23	48.6	56.6	2.87	3.40	0.859
22 Jun.	03	59	0.429E+23	0.628E+23	30.2	26.3	1.90	1.65	1.147
22 Jun.	06	36	0.287E+23	0.265E+23	37.9	46.1	2.55	2.65	0.822
22 Jun.	06	37	0.265E+23	0.270E+23	68.3	75.0	2.75	3.10	0.910
22 Jun.	07	35	0.187E+23	0.156E+23	53.1	45.6	2.62	3.15	1.166
22 Jun.	08	45	0.878E+22	0.772E+22	57.3	30.9	3.40	3.50	1.857
23 Jun.	19	11	0.554E+23	0.521E+23	42.9	166.9	2.72	3.25	0.257
23 Jun.	21	28	0.214E+23	0.231E+23	36.3	44.9	2.74	2.75	0.808
24 Jun.	02	04	0.128E+23	0.126E+23	34.0	28.6	2.98	2.90	1.188
24 Jun.	02	24	0.214E+23	0.184E+23	244.9	183.4	3.68	4.75	1.335
24 Jun.	05	47	0.278E+23	0.407E+23	30.7	37.7	2.19	2.15	0.815
24 Jun.	11	10	0.273E+23	0.309E+23	52.5	37.4	2.45	2.35	1.405
24 Jun.	17	29	0.318E+23	0.295E+23	54.5	60.4	2.67	2.80	0.902
24 Jun.	18	59	0.287E+23	0.328E+23	50.7	37.3	2.71	2.30	1.360
25 Jun.	00	26	0.101E+23	0.105E+23	110.0	75.4	3.84	4.25	1.459
25 Jun.	07	04	0.854E+22	0.840E+22	35.6	16.3	2.73	2.75	2.183
25 Jun.	18	20	0.115E+24	0.154E+24	39.6	48.6	1.60	1.50	0.815
26 Jun.	00	29	0.104E+23	0.136E+23	25.8	13.5	2.84	2.20	1.903
26 Jun.	03	40	0.101E+24	0.235E+24	75.0	66.9	2.29	1.45	1.121
26 Jun.	14	23	0.454E+23	0.541E+23	128.6	150.4	3.11	3.10	0.855
26 Jun.	20	48	0.377E+23	0.659E+23	19.2	13.5	1.73	1.30	1.420
26 Jun.	22	57	0.167E+24	0.379E+24	77.6	119.3	1.90	1.50	0.651
17 Jun.	05	05	0.343E+22	0.338E+22	93.7	66.3	3.83	5.95	1.412
27 Jun.	20	28	0.508E+23	0.666E+23	31.2	39.3	1.96	1.85	0.794
28 Jun.	05	21	0.767E+22	0.107E+23	42.5	19.6	3.46	2.70	2.173
29 Jun.	10	59	0.190E+23	0.213E+23	114.2	68.2	3.24	3.25	1.675
29 Jun.	13	19	0.117E+23	0.121E+23	43.6	32.0	2.83	3.05	1.364
29 Jun.	14	11	0.740E+23	0.187E+24	66.5	42.9	2.26	1.35	1.552
29 Jun.	21	11	0.463E+23	0.452E+23	50.4	41.9	2.21	2.15	1.204
30 Jun.	07	18	0.300E+23	0.213E+24	49.5	8.4	1.92	0.75	5 902
30 Jun.	13	33	0.242E+23	0.598E+23	23.6	15.3	2.04	1.40	1.543
30 Jun.	17	33	0.145E+23	0.118E+23	77.2	55.5	3.36	3.70	1.390
01 Jul.	00	11	0.912E+22	0.961E+22	39.3	33.7	3.06	3.35	1.165
01 Jul.	04	31	0.428E+22	0.541E+22	81.1	84.0	3.46	5.50	0.966
09 Jun.	21	49	0.308E+26	0.318E+26	409.8	204.5	0.49	0.41	2.004
26 May	11	59		[0 455E+28]					
9 Jun.	21	49		[0.960E+25]					
8 Jun.	22	04	0.780E+25	0.150E+26	460	170	0.75	0.52	3 0
21 Jun.	15	25	0.873E+26	[0.187E+27]	300	60	0.09	0 07	5 0

Table 3-2

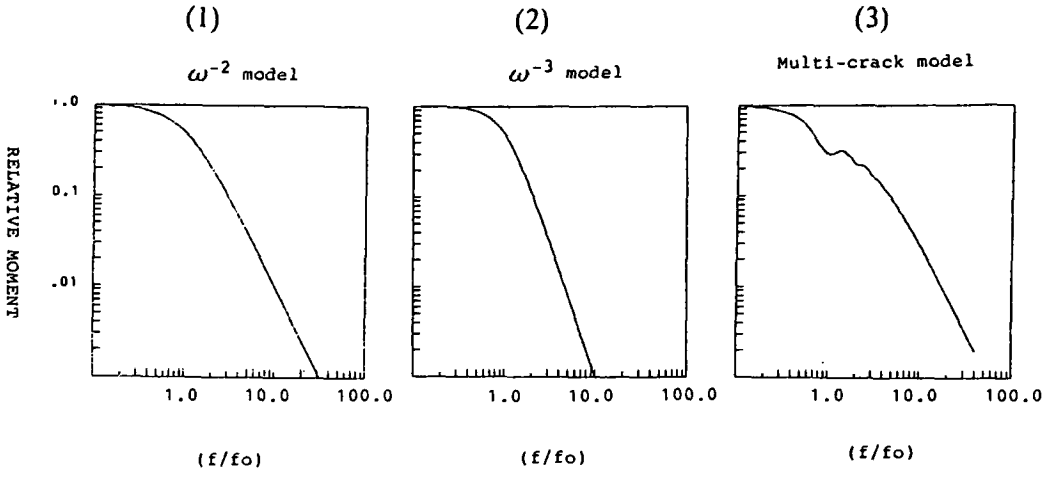

Fig A 1

	(1) ω^{-2} model	(2) ω^{-3} model	(3) multi-crack model
Relative seismic moment	0.96	1.20	0.63
Relative corner frequency	1.02	0.66	1.95

Table A 1

Chapter 2

Reconstruction of Slip Velocity Distribution on Fault Plane Using High-Frequency Seismic Waves

1. INTRODUCTION

Several approaches are available to reconstruct complex rupture processes on the fault plane during large earthquakes. One is a waveform inversion method, in which the model parameters such as the time-space distributions of moment-rate function and/or the spatial distribution of rupture velocities on the fault plane during earthquakes are so determined that synthetic seismograms using a theoretical Green's function method (for example, Heaton and Helmberger,1979; Kikuchi and Kanamori,1982; Takeo,1987,1988; Hartzell and Heaton,1983) or using a semi-empirical Green's function method (Fukuyama and Irikura, 1986,1988) agree well with the observed ones. Another approach is presented by Ruff(1984,1987) who reconstructs the moment rate density function from source time functions at many stations in connection with the Radon transform. He replaced the inverse Radon transform with an iterative filtering method to determine the time-space moment rate function. Using seismograms observed at longer periods than 1 sec, they gave interesting results of heterogeneous faulting during large earthquakes.

On the other hand, although the mechanism of shorter period (<1 sec) wave generation have drawn much interest to both seismologists, who wish to construct physically reliable models of faulting, and engineering seismologists, who wish to predict strong ground motions during large earthquakes, the waveform inversion methods have not been able to be applied because of the insufficient knowledge of deterministic path effects for representing the Green's function in the high-frequency range. Several trials to infer the source process using high-frequency

seismic waves have been performed. Nagamune(1969) for the 1968 Tokati-Oki earthquake and the 1963 Etorofu-Oki earthquake; Mori and Shimazaki(1984) for the 1968 Tokati-Oki earthquake; Mori(1984) for the 1965 Rat Islands earthquake; Fujino et al.(1984) for the 1979 Imperial Valley, California, earthquake; all of them picked out distinct phases from the strong ground motion records and/or short-period seismograms and determined relative positions of subevents on the represented faults which emitted high-frequency seismic waves. In particular, Mori and Shimazaki(1984) determined not only the positions of subevents but their high dynamic-stress drop values from the slope of the corresponding velocity pulse in strong ground motion records to show the local heterogeneous faulting of large earthquakes. Their method is useful for seismic records with distinct phases.

Recently, Madariaga(1983), and Bernard and Madariaga(1984) developed an asymptotic calculation method of high-frequency ground motions near a fault based on the ray theory and the idea of the isochrone, which is a closed curve on the fault plane and is so called because disturbances reach an observation point simultaneously from points densely distributed along it. An asymptotic approximation to near-source velocity and acceleration at a moment is obtained that involves a simple line integration along an isochrone for every time step. It is shown that wave front discontinuities are radiated every time an isochrone becomes contact with to a barrier. This result is compared with discrete wavenumber synthetics obtained by Bouchon(1982) for the Gilroy 6 recording of the 1979 Coyote Lake, California,

earthquake. The agreement between the result of the asymptotic and the full numerical method is extremely good. Spudich and Frazer(1984) also show a calculation method of high-frequency ground accelerations which are represented by the space-time change of slip velocity and the isochrone velocity. They suggested a possible method for inverting ground motions for both slip velocity and rupture velocity over the fault.

Moreover, Beroza and Spudich(1988) performed a linearized inversion for slip intensity and rupture time by iteratively perturbing an assumed starting time. The inverse problem for the model perturbation is solved by using a tomographic back projection method. They applied the technique to recordings of the 1984 Morgan Hill, California, earthquake.

In this study, based on the dynamic crack model and the idea of the isochrone, we demonstrate first that the observed source time function can be represented by a Radon transform of slip velocity on the fault plane. Next, to recover slip velocity distribution on the fault plane directly, we show an inverse Radon transform method which uses the back-projection with a windowing procedure. We apply this method to the acceleration seismograms from the 1980 Izu-Hanto-Toho-Oki earthquake with M_{JMA}=6.7. We compare the results of our analysis with those of other waveform inversion, using longer period seismic waves and discuss the difference of the fault heterogeneities depending on the period range of the seismic waves generated by the source region.

2. METHOD

2-1 Formulation for the reconstruction of heterogeneous faulting related to high-frequency seismic waves

The far-field ground displacement U(x,t) is described by

$$U(x,t) = \iint_{\Sigma} \Delta\dot{u}(\xi,t) * G(\xi;x,t)\, d\Sigma \qquad (1)$$

where $\Delta\dot{u}(\xi,t)$ is the slip velocity function, $G(\xi;x,t)$ is the Green's function from the point ξ on the fault plane to the observation point x, and * denotes convolution (Aki and Richards,1980). By high-frequency radiation, we mean that the wavelengths in which we are interested are all shorter than the shortest distance from the source to the observation point. In this case, the far-field term of the radiation from point dislocation source is appropriate to the Green's function. We assume that the Green's function varies smoothly with position ξ compared with $\Delta\dot{u}(\xi,t)$. Hence, the Green's function can be taken outside the fault integral. Deconvolving the Green's function from the observed seismograms by an adequate method, we can estimate the source time function S(x,t) for each station. The obtained source time function for the point x is

$$S(x,t) \sim \iint_{\Sigma} \Delta\dot{u}(\xi,t)\, d\Sigma \qquad (2)$$

Following Spudich and Frazer(1984), we take slip velocity function as

$$\Delta\dot{u}(x,t) = f(t-t_r(\xi))\, S_r(\xi) \qquad (3)$$

where $f(t-t_r(\xi))$ is the time dependence of slip velocity and

$s_r(\xi)$ is a weight function of slip velocity which depend only on position ξ. We say the point ξ on the fault plane ruptures at $t_r(\xi)$ with the time dependence $f(t-t_r(\xi))$.

A physical model of earthquake rupture is the crack model. There is a square-root singularity in the slip velocity time function at rupture time t_r which is theoretically obtained to satisfy the boundary conditions for a expanding self-similar crack (Kostrov,1964). In Kostrov's analytical model, the dislocation rate function (the slip velocity time function) $\dot{d}(t)$ was approximated by

$$\dot{d}(t)=\frac{\sigma_e C}{\mu}\left(\frac{V_r r}{2}\right)^{\frac{1}{2}}\frac{H(t-t_r)}{\sqrt{t-t_r}} \qquad (4)$$

where r is the distance from the hypocenter, σ_e is stress drop, V_r is rupture velocity, and $t_r=r/V_r$, and C is the function of V_r/V_S, where V_S is S-wave velocity (Dahlen,1974). In this case, we choose

$$f(t-t_r(\xi))=(t-t_r)^{-1/2}H(t-t_r),$$

$$\text{and } s_r(\xi)=\frac{\sigma_e C}{\mu}\left(\frac{V_r r}{2}\right)^{\frac{1}{2}} \qquad (5)$$

Here $s_r(\xi)$ is proportional to slip velocity or stress drop.

A more physically realistic model of earthquake rupture than the Kostrov's analytical model is that obtained from the numerical simulations of spontaneous rupture in three-dimensional models including the stopping process of crack (e.g. Day,1982). Day's calculation result(1982) of slip velocity time function is shown by the thin line in Fig.1(a). In the simulation, although

the time dependence of slip velocity f(t) cannot be expressed in closed form, the shape of f(t) was obtained to be very similar to $t^{-1/2}H(t)$.

The crack models above mentioned possess physically unrealistic stress and slip velocity singularities at the crack tip. Actually, the square-root singularity of the source time function can be eliminated by assuming the cohesive zone introduced by Barenblatt(1959) by means of the realistic condition. Ohnaka and Yamamoto(1984) measured the slip velocity near the slipping zone for a stick-slip instability model in the laboratory experiment. A typical example of the measured slip velocity with time is shown in Fig.1(b). The shape of time dependence of the slip velocity was also similar to be $t^{-1/2}H(t)$. So, using the $f(t)=t^{-1/2}H(t)$ based on the crack models, we need to analyze the seismograms recorded in the high-frequency range with high accuracy.

Substituting formula (3) into (2), the source time function is approximately represented by

$$S(x,t) \sim \iint_{\Sigma} f(t-t_r) S_r(\xi) d\Sigma = f(t) * \iint_{\Sigma} \delta(t-t_r) S_r(\xi) d\Sigma \quad (6)$$

The time dependence of slip velocity is removed by a deconvolution technique. We call Y(x,t) "deconvolved source time function" by removing f(t) from the source time function S(x,t).

We can change the integral variables $d\Sigma$ to $V_L(\xi)dTdL$, where v_L is isochrone velocity, T is time, and $L=L(x,\xi,T)$ is the isochrone (Madariaga,1983; Bernard and Madariaga,1984). Then the deconvolved source time function is represented by

$$Y(x,t)=\iint_{\Sigma}\delta(t-t_r)S_r(\xi)d\Sigma=\int_{L}S_r(L)V_L(L)dL \qquad (7)$$

This deconvolved source time function is approximated to the integration of the product of the weighting function $s_r(L)$ and the isochrone velocity along the isochrone. The shape of the isochrone on the fault plane depends on the fault-observation point geometry, the rupture velocity on the fault plane, and the wave velocity. Spudich and Frazer(1984) called that $s_r(\xi)$ is "slip velocity intensity factor" by analogy with the stress drop intensity factor in dynamic crack propagation problems (Aki and Richards,1980,p.857). Hereafter we call $s_r(\xi)$ "slip velocity intensity (SVI)".

Formula (7) is the Radon-transform. Unlike previous inversion studies of earthquake rupture process we don't require the a priori assumption of the faulting area. For inverting transform (7), we use a back-projection method with a windowing procedure. The window size is determined mainly from the distribution of observed points. Assuming that the rupture and S-wave velocities are constant, the isochrone velocity $V_L(\xi)$ can be determined. Finally, removing the isochrone velocity after performing the inverse Radon transform, we can obtain the SVI distribution over the fault plane. We show this procedure applied to a model simulation in the case of the fault-observation-point geometry for the 1980 Izu-Hanto-Toho-Oki earthquake with M_{JMA}=6.7. Fig. 2 shows the map of the locations of the 5 observation stations (triangles) used in this study, the epicenter (closed square), and the inferred fault plane of this earthquake with strike direction N15°W, dip angle 90°, fault

length 15km and fault width 7.5km. The focal depth of this earthquake is assumed to be 12km (Imoto et al.,1981; Matsu'ura,1983).

In Fig. 3, we show the flow-chart of the reconstruction method. A simple example of the source process reconstruction is shown in which non-zero slip velocity function exists at two points on the fault plane. Fig.3 (a) shows the distribution of slip velocity function on the virtual plane including the inferred fault plane. In our bird's-eye pictures, the X- and Y-axes correspond to the north-south, and the bottom-top directions, respectively. The region enclosed by dotted lines shows the inferred fault plane corresponding to the 1980 Izu-Hanto-Toho-Oki earthquake. In this case, the rupture smoothly propagates from the center (indicated by an arrow) with constant rupture velocity of 3.0 km/s. The slip velocity is given to be zero except the two points over the fault plane. Generally each slip velocity may have an arbitrary time dependence function. Here, we assume the same time dependence function at the two points as f(t) for obtaining the deconvolved source time function. We call this model MODEL I. Fig.3(b) shows the deconvolved source time functions at NBK and KWN, respectively from the SVI distribution shown in Fig.3(a) with the S-wave velocity of 3.5km/s. In this case, deconvolved source time function Y(x,t) has zero value except for the two impulses contributed from the two points with non-zero slip velocity. Fig.3(c) shows the projection of Y(x,t) at each station onto the virtual plane. Fig.3(d) shows the back-projection reconstruction using Y(x,t) at 5 stations. This figure does not reproduce the

distribution of SVI (in Fig.3(a)) well. Therefore we design the scheme of a windowing procedure for improving the result of the reconstruction. We divide the virtual plane into pixels, 0.4km square. The lower limit of the pixel size ($\Delta\chi$) is determined from the highest frequency of signals (f_{max}), the rupture velocity (V_r) and the extent of projection angle related to the station distribution (θ), i.e. $\Delta\chi=\frac{V_r}{f_{max}}\cdot\frac{1}{\sin\theta}$. For each station, we search for the pixels through which the isochrone corresponding to the non-zero value of the deconvolved source time function [Y(x,t)] passes on the virtual plane. We give those pixels flags. Then we can estimate a flag map on the fault plane for each station. We take the logical product of those flag maps, and then we find the (discrete) spatial window function [W(x,y)] of the virtual plane as shown in Fig.3(e). Fig.3(f) shows the windowed back-projection reconstruction. This is produced from the back-projection reconstruction(in Fig.3(d)) which is windowed by W(x,y) (in Fig.3(e)). This figure well recovers the SVI distribution on the fault plane (Fig.3(a)). Before applying this procedure to our data set, we test the applicability of this procedure for some simulation models.

2-2 Test of applicability of the procedure

We applied this procedure to the following three cases, MODEL II, III, and IV.

In MODEL II, the slip velocity time function is given a truncated $t^{-1/2}H(t)$ dependence following the Day's proposal (1982) shown by the thick line in Fig.1(a),

$H(t-t_r)[1-H(t-t_h)]t^{-1/2}$ (8)

i.e. the slip velocity function has not only a rupture initiation but also a healing with the time t_h. The fault-observation geometry, the rupture velocity, the S-wave velocity, the rupture initiation point and the SVI distribution are the same as in MODEL I. Fig.4(a) shows the SVI distribution on the virtual plane for model II. There is non-zero slip velocity at two points and each slip velocity has a rise time of 0.5s (t_h-t_r=0.5s). We do not use function (8) but delta(t) as f(t) for obtaining the deconvolved source time function [Y(x,t)] (formula (6)). In Fig.4(b), we show the reconstruction result of the SVI distribution. On the reconstruction, there are side lobes near the pixels with non-zero SVI. Because we don't consider the healing effect in obtaining the deconvolved source time function, the abrupt change of slip velocity on the healing effect generates a false SVI distribution. Using an inappropriate slip velocity time dependence for obtaining deconvolved source time function causes the false spatial distribution of SVI.

MODEL III: In Fig.5(a), we show the SVI distribution on the fault plane for MODEL III. The non-zero slip velocity functions are located on a line segment in the virtual plane. Each slip velocity time function and the model parameters are the same as in MODEL I. Fig.5(b) shows the reconstruction result of the SVI distribution. Although the places of the pixels with non-zero SVI are well reconstructed, the reconstructed values of SVI show a slight fluctuation.

MODEL IV: In this case, 18 assumed stations with hypocentral distance 20km are arranged at 20° intervals in a

circle shown in Fig.6(a). The SVI distribution on the virtual plane is shown in Fig.6(b). The non-zero slip velocity functions are located on all sides of the inferred fault plane of the 1980 Izu-Hanto-Toho-Oki earthquake. The model parameters are the same as in MODEL I. In Fig.6(c), we show the reconstruction of the SVI distribution. Although the spatial resolution in the horizontal direction is good, that in the vertical direction is not good. This false reconstruction in the vertical direction is caused by the narrow range of the emergent angles from source to stations, while the azimuthal angle are taken to be wide.

Throughout these model simulations, good reconstruction results are demonstrated by a back-projection method with a windowing whose size is determined from the distribution of observation stations.

3. Application to the 1980 Izu-Hanto-Toho-Oki earthquake

In 2-2, we examined the applicability of our procedure for some simulation models and showed that it can well recover the distribution of SVI on the fault plane. Here, we apply our procedure to the data set of the target earthquake, the 1980 Izu-Hanto-Toho-Oki earthquake. We assumed the virtual source plane with 20km square and divided the plane into pixels 0.4km square same as in the model simulations.

To estimate the deconvolved source time function, we deconvolved observed seismograms with the path effect using the records from a small event as an empirical Green's function with the Winner filtering technique (Robinson,1967). In Fig.7, we show an example of observed seismic traces and the design scheme of Wiener filtering for predicting the deconvolved source time function. Fig.7(a) shows the accelerogram of a small event with M_{JMA}=4.9 recorded at KWN. The trace shows the NS component record from the onset of S-waves. Added to the record is noise with zero-mean and 1% standard deviation of the maximum signal amplitude for stabilizing to predict a filter series. This trace corresponds to the input trace for the filtering. Fig.7(b) shows the NS component accelerogram record from the onset of S-waves from the mainshock at KWN. This trace corresponds to desired output of the filtering. Fig.7(c) is the estimated filter coefficient series and Fig.7(d) is the estimated actual output for this deconvolution procedure. The obtained filter series in Fig.7(c) corresponds to the source time function S(x,t) in formula(2). Next, we assume that f(t) is given to be $t^{-1/2}H(t)$ from Kostrov's solution(1964) for the dynamic crack model. We

deconvolve the filter series with f(t). The deconvolved source time function Y(x,t) is shown in Fig.7(e). Although the source time function should be a non-negative function without assuming a physically unacceptable reverse dislocation, our result in Fig.7(e) is not a non-negative value.

One problem is that we have used only one empirical Green's function for each station taking the Green's function outside the fault integral in formula(1). Actually, the Green's function changes from pixel to pixel because of the differences of the propagation path and the radiation pattern from each pixel to the observation point. Such spatial fluctuation of the Green's function is treated as an random noise in this analysis. Therefore, we consider that the obtained Y(t) is represented as a time function contaminated with the random noises originated from the uncertainty of the Green's function. We assume that the true (deconvolved) source time function $F_{true}(t)$ is represented by

$$F_{true}(t) = Re\{ g(t) e^{i\theta(t)} \} \qquad (9)$$

where g(t) is a non-negative time dependent amplitude (i.e. envelope) and $\theta(t)$ is a time dependent phase (Taner et al,1979). As g(t) is a non-negative time function, $g(t) = |F_{true}(t)| = F_{true}(t)$ ($F_{true}(t)$ is also a non-negative time function). In contrast to this, our obtained filter coefficient series F(t) is

$$F(t) = Re\left[\{ g(t) + n_a(t) \} e^{i\{\theta(t) + n_p(t)\}} \right] \qquad (10)$$

being contaminated by a random error

$$n(t) = \mathrm{Re}\{n_a(t) e^{i n_p(t)}\} \qquad (11)$$

where $n_a(t)$ and $n_p(t)$ correspond to the time dependent amplitude and phase of noise with assuming that $g(t) >> n_a(t)$ and $g(t)$ does not correlate with $n_a(t)$. Then, we obtain the envelope $F(t)$ in the following form

$$|F(t)| = |g(t) + n_a(t)| \sim |g(t)| = F_{true}(t) \qquad (12)$$

In this formula, the effect of the random noise due to uncertainty of the Green's function on the filter coefficient series can be small in the analysis. In Fig.7(f) we show the envelope of the filter coefficient series corresponding to the deconvolved source time function in Fig.7(e).

The other problem is that the record from a small event is not exactly a true Green's function because even a small event does not originate from a point but from a finite source area. The fault area of the small event source gives the spatial resolution of heterogeneity obtained in the present study. We use the records from a foreshock as Green's functions, whose fault plane solution is almost the same as that of the mainshock (Imoto et al.,1981). The corner frequency of this event is about 1Hz obtained from the observed seismic spectra. Therefore, in Fig.7(g) we show the smoothed envelope with the bell-shaped time window of the length of 1 sec considering the finite source duration of the small event. If we can use the records from an even smaller event, we can choose the shorter time window that corresponds approximately to the corner frequency of that event, and consequently, a higher spatial resolution on the fault plane

can be expected than in the present analysis. Finally, we regard the time series in Fig.7(g) as the deconvolved source time function Y(x,t) at KWN. In this case, we determined only the relative magnitude of deconvolved source time function, because we cannot determine the scaling relation between the main shock(M_{JMA}=6.7) and the small shock(M_{JMA}=4.9) in the high-frequency range. If we obtain the source parameters such as stress drop of the small shock with some adequate methods (e.g. Iwata and Irikura,1988), we can determine the absolute values of the deconvolved source time functions.

Fig.8 shows the map of the observation stations (Fig.2 again) and the deconvolved source time functions obtained at 5 stations. We reconstruct the distribution of SVI on the fault plane using the 5 deconvolved source time functions. Fig.9 shows the contour map of the SVI distribution plotted together with the hypocentral distribution of the 1980 Izu-Hanto-Toho-Oki earthquake and its aftershocks(M>2.9) occurring within 10 hours after the mainshock occurred (Matsu'ura,1983,Fig.11) in the vertical section in parallel with the direction N20^{o}W. The rectangle with dotted lines shows the frame of the inferred fault plane from the aftershock distribution. The relative amplitude of SVI is displayed with shading. The cross indicates the hypocenter of the mainshock. Following Kostrov(1964), the SVI corresponds to the stress drop. Therefore our result shows the heterogeneous stress drop on the fault plane. It is interesting that the area in which high SVI is generated seems to correspond to the area with less aftershocks.

4. DISCUSSION

In Fig.9 there are SVI with higher amplitude in the central part to the north on the fault plane inferred from the aftershock distribution but with lower amplitude in the southern part. This result suggests that the rupture process in the central part to the north mainly contributed to the high-frequency radiation. The distribution of SVI oozes out of the inferred fault plane at the bottom.

Several studies of the rupture process have been performed with the waveform inversion for the 1980 Izu-Hanto-Toho-Oki earthquake. Takeo(1988) obtained the distribution of the dislocation and the rupture starting time on the fault plane from the waveform inversion with the JMA strong ground motion displacement records. Fig.10(a) shows the isograms of the dislocation distribution of the mainshock on the fault plane (Takeo,1988,Fig.12). The errors of estimated dislocations are in the range of 0.1-0.4m. He assumed a larger fault than the inferred fault from the aftershock distribution. Takeo's result shows that large dislocations are distributed on the central and south parts of the fault plane. Combining our result with the Takeo's result, we deduce that the rupture in the center of the fault occurred with large dislocation and high SVI. On the contrary, the rupture in the south area was smooth because though the dislocation was also large, the SVI was small. The north area in the Takeo's result with a small dislocation has low SVI in our result.

Using the integrated acceleration (i.e. velocity) strong motion records, Fukuyama and Irikura (1988) obtained the stress

drop distribution of the mainshock from the waveform inversion. Fig.10(b) shows the obtained stress drop on the fault plane. Except for the highest stress drop around the northern edge of the fault plane, our SVI distribution corresponds well to their stress drop distribution.

To examine the validity of the estimated SVI distribution obtained here, we calculate the synthetic seismograms for the heterogeneous slip velocity model based on our result as well as those for the uniform slip velocity model using the Irikura's method (1986,1988). The rise time in this calculation is taken to be a constant value for the case of the uniform slip velocity model. That for the case of heterogeneous slip velocity model is taken to be variable as a function of the position on the fault plane following the so-called crack-like model proposed by Yomogida(1988). The synthetic results are illustrated for the mainshock accelerations at KWN, the nearest observation station from the hypocenter in Fig.11 together with the observed seismograms. The observed accelerograms of NS (the left panels) and EW (the right panels) components from the mainshock at KWN is shown in the top of Fig.11. In the middle and the bottom of Fig.11 are shown the synthetic seismograms for the uniform slip velocity model and those for the heterogeneous SVI model. The synthetic acceleration of the EW component for the heterogeneous slip velocity model shows considerable improvements in envelope and maximum amplitude value over that for the uniform slip velocity model and also that of the NS component is a little improved.

5. CONCLUSIONS

We propose an inverse Radon-transform method to reconstruct the distribution of slip velocity intensity (SVI) on the fault plane of a large earthquake by using high-frequency strong ground motions near the fault. The direct back-projection method with a windowing procedure used here has the advantage of not requiring a priori assumption of faulting area over previous source process inversion studies. This method has been applied to the records of the 1980 Izu-Hanto-Toho-Oki earthquake and the heterogeneous SVI distribution over the fault plane are obtained. Relatively large values of SVI are found in the center area to the north on the fault plane, which corresponds to the zone with less aftershock occurrence. This suggests that the heterogeneous rupture effectively emitting high-frequency seismic waves is restricted to a small region of the fault plane inferred from the aftershock distribution. Combining the SVI distribution from short-period ($<$ 1 sec) seismic waves with the dislocation distribution from long-period ($>$ 1 sec) seismic waves, we can understand the detailed faulting process of this earthquake. In the center of the fault, there occur a large dislocation and a high slip velocity due to abrupt jump in rupture velocity or stress drop. On the other hand, in the southern part, there occur a large dislocation but a low slip velocity, i.e. low stress drop, and in the northern part, a small dislocation and a low slip velocity, suggesting that the rupture is smooth in these regions.

ACKNOWLEDGMENTS

We would like to thank Dr. K. Kudo of the Earthquake Research Institute, University of Tokyo and Dr. K. Ishida of the Central Research Institute of the Electric Power Industry, Japan for providing the digital accelerograms. We also thank Profs. T. Mikumo, K. Kobayashi and J. Akamatsu of Kyoto University for their critical reading for revising the manuscript. This study was supported partly by a Grant-in Aid for Research on Natural Disasters from the Ministry of Education, Science and Culture of Japan (No.62601004,Organizer T. Hirasawa).

FIGURE CAPTIONS

Fig. 1 (a): Sketch of the slip velocity function obtained by Day(1982,Fig.14) with three-dimensional finite difference simulation of fault dynamics. The thin line shows the numerical solution with spontaneous rupture propagation and the thick line shows the approximated time function with truncated $t^{-1/2}H(t)$ time dependence. (b): An experimental result of the slip velocity and displacement with time measured by Ohnaka and Yamamoto(1984) in the stick slip instability model. Thick lines show the measured displacement and thin lines show the slip velocity from the derivative of the measured displacement.

Fig. 2 Map of observation stations (triangles) and location of epicenter (closed square) and fault plane with 15km x 7.5km of the 1980 Izu-Hanto-Toho-Oki earthquake.

Fig. 3 Flow-chart of reconstruction method. An example is shown for MODEL I. (a): SVI (slip velocity intensity) distribution on the virtual plane including the fault plane. The region enclosed by the dotted line shows the inferred fault plane. In the bird's-eye pictures, the X- and Y-axes correspond to the north-south, and bottom-top directions, respectively. The rupture smoothly propagates from the center of the 20km square (indicated by an arrow) with a constant rupture velocity of 3.0km/s. The slip velocity is given to be non-zero at only two points. We use the same time dependence function as f(t) for obtaining the deconvolved source time function. (b): Two traces correspond to the deconvolved source time functions [Y(x,t)] from the slip

velocity distribution in Fig.3(a) at NBK and KWN, respectively. (c): Projection of Y(x,t) at NBK and KWN onto the fault plane, respectively. (d): Back-projection reconstructions using the deconvolved source time functions at 5 stations. This figure does not reproduce well the given slip velocity distribution (see Fig.3(a)). (e): Spatial window function [W(x,y)] of the virtual plane. (f): Windowed back-projection reconstruction. This reconstruction result recovers well the given distribution of SVI (see Fig.3(a)).

Fig. 4 (a): SVI distribution on virtual plane for MODEL II. It is the same as in MODEL I. (c): Reconstruction result of SVI. On the reconstruction, there are some side lobes near the pixels which have the non-zero SVI caused by the healing effect.

Fig. 5 (a): SVI distribution on virtual plane for MODEL III. The non-zero slip velocity functions are located on a line segment in the virtual plane. (b): Reconstruction result of the SVI. Although the places of the pixels with non-zero SVI are well reconstructed, the reconstructed values of SVI show a slight scatter.

Fig.6 (a) Distribution of 18 assumed stations with focal distance 20km. (b): SVI distribution on the virtual plane. The non-zero slip velocity functions are located on all sides of the inferred fault plane of the 1980 Izu-Hanto-Toho-Oki earthquake. The model parameters are the same as in MODEL I. (c): Reconstruction

distribution of the SVI.

Fig. 7 An example of seismic traces and design of the Wiener filter to estimate deconvolved source time function. (a) Accelerogram of a small shock(M_{JMA}=4.9) recorded at KWN. The trace shows NS component record from the onset of S-waves. Added to the record is noise with zero-mean and 1% standard deviation of the maximum signal amplitude for stabilizing the solution. (b): Accelerogram of the mainshock recorded at KWN. This trace also shows the NS component record from the onset of S-waves. This trace is the desired output for the filtering. (c): Estimated filter coefficient series. (d): Actual output series for this deconvolution. (e): Deconvolved filter coefficient series with the $t^{-1/2}H(t)$ time dependence from (c). (f): Envelope of (e). (g): Smoothed envelope of (f) with bell-shaped time window of 1 sec. We regard this time series as the inferred source time function at KWN.

Fig. 8 Deconvolved source time functions at five stations. Each trace is normalized with the maximum amplitude of each trace.

Fig. 9 Contour map of SVI distribution on hypocentral distribution of the 1980 Izu-Hanto-Toho-Oki earthquake and its aftershocks(M>2.9) occurring within 10 hours after the mainshock (Matsu'ura,1983,Fig.11) in vertical section parallel to the direction N20^{o}W. The rectangle with dotted lines shows the frame of the inferred fault plane. The relative amplitude of SVI is displayed with shading. The cross indicates the starting point of

the mainshock. The area in which high SVI was generated seems to correspond to the area with less aftershock occurrence.

Fig. 10 Some results of waveform inversion for the 1980 Izu-Hanto-Toho-Oki earthquake. (a): Isograms of the dislocation distribution of the mainshock on the fault plane inferred from the waveform inversion by Takeo(1988,Fig.12) using the JMA strong motion displacement records. (b): Obtained stress drop distribution of the mainshock from the waveform inversion by Fukuyama and Irikura (1988) using velocity records.

Fig. 11 Observed accelerogram from the mainshock at KWN and synthetic seismograms. The synthetics are performed by the empirical Green's function method (Irikura,1986). The left panels show the NS-components and the right panels, the EW-components. From top to bottom, the observed accelerograms, the synthetic accelerograms using uniform slip velocity distribution model and those using the heterogeneous slip velocity distribution obtained in this study.

REFERENCES

AKI, K. and P. G. RICHARDS, Quantitative Seismology : Theory and methods, W.H.Freeman, San Francisco, California., , , 1980.

ANDREWS, D. J., Rupture velocity of plane-strain shear cracks, J. Geophys. Res., **81**, 5679-5687, 1976.

BARENBLATT, G. I., The formation of equilibrium cracks during brittle fracture. General ideas and hypotheses, J. Appl. Math. and Mechanics, **23**, 622-636, 1959.

BEROZA, G. C. and P. SPUDICH, Linearized inversion for fault rupture behavior: Application to the 1984 Morgan Hill, California, earthquake, J. Geophys. Res., **93**, 6275-6296, 1988.

BERNARD, P. and R. MADARIAGA, A new asymptotic method for the modeling of near field accelerograms, Bull. Seismol. Soc. Am., **74**, 539-558, 1984.

DAY, S.M., Three-dimensional finite difference simulation of fault dynamics : Rectangular faults with fixed rupture velocity, Bull. Seismol. Soc. Am., **72**, 705-727, 1982.

DAHLEN,F.A., On the ration of P-wave to S-wave corner frequencies for shallow earthquake sources, Bull. Seismol. Soc. Am., **64**, 1159-1180, 1974.

FUJINO, Y., Y. YOKOTA, Y. HAMAZAKI and R. INOUE, Multiple event analysis of 1979 Imperial Valley earthquake using distinct phases in near-field accelerograms, Proc. JSCE, **344**, 127-147, 1984.

FUKUYAMA, E. and K. IRIKURA, Rupture process of the 1983 Japan Sea (Akita-Oki) earthquake using waveform inversion method, Bull. Seismol. Soc. Am., **76**, 1623-1640, 1986.

FUKUYAMA, E. and K. IRIKURA, Heterogeneity of the 1980 Izu-Hanto-Toho-Oki earthquake rupture process, submitted to Geophys. J. Roy. Astron. Soc., , , 1988.

HARTZELL,S.H. and T.H. HEATON, Inversion of strong ground motion and teleseismic waveform data for the fault rupture history of the 1979 Imperial Valley, California, earthquake, Bull. Seismol. Soc. Am., **73**, 1553-1583, 1983.

HEATON, T.H. and D.V. HELMBERGER, Generalized ray models of the San Fernando earthquake, Bull. Seismol. Soc. Am., **69**, 1311-1341, 1979.

IMOTO, S., I.KARAKAMA, R.S.MATSU'URA, F.YAMAZAKI, A.YOSHIDA and K.ISHIBASHI, Focal mechanisms of the 1980 earthquake swarm off the east coast of the Izu Peninsula, Japan, Zisin II, **34**, 481-493, 1981 (in Japanese).

IRIKURA, K., Prediction of strong acceleration motions using empirical Green's function, Proc. 7th Japan Earthquake

Engineering, , 151-156, 1986.

IRIKURA, K., Estimation of near-field ground motion using empirical Green's function, Proc. 9th World Conference on Earthquake Engineering, , , 1988.

IWATA, T. and K. IRIKURA, Source parameters of the 1983 Japan Sea earthquake, J. Phys. Earth, 37, 171-200, 1988.

KIKUCHI, M. and H. KANAMORI, Inversion of complex body waves, Bull. Seismol. Soc. Am., 72, 491-506, 1982.

KOSTROV, B., Self-similar problems of propagation of shear cracks, J. APPL. Math. Mech., 28, 1077-1087, 1964.

LAY, T. and H.KANAMORI, An asperity model for great earthquake sequences, Earthquake prediction -An International Review, Maurice Ewing Series, edited by D.W.Simpson and P.G.Richards, Am. Geophys. Union, Washington,D.C., 4, 579-592, 1981.

MADARIAGA, R., High frequency radiation from dynamic earthquake fault models, Ann. Geophys., 1, 17-23, 1983.

MATSU'URA, S.R., Detailed study of the earthquake sequence in 1980 off the east coast of Izu peninsula, Japan, J. Phys. Earth, 31, 65-101, 1983.

MORI, J., Short- and long-period subevents of the 4 February 1965 Rat Islands earthquake, Bull. Seismol. Soc. Am., 74, 1331-1347, 1984.

MORI, J. and K. SHIMAZAKI, High stress drops of short-period subevents from the 1968 Tokati-Oki earthquake as observed on strong-motion records, Bull. Seismol. Soc. Am., 74, 1529-1544, 1984.

NAGAMUNE, T., Process in the source region for a great earthquake (The Tokachi-Oki earthquake, 1968 and the Etorofu-Oki earthquake, 1963), Zisin II, 22, 104-114, 1969 (in Japanese).

OHNAKA, M. and K.YAMAMOTO, Experimental studies of failure nucleation and propagation along simulated faults in rock. Study on short-period behavior in fault motion and estimation of input seismic motion, Final Technical Report(Organizer R.Sato), A-59-3, 11-46, 1984 (in Japanese).

ROBINSON, E.A., Multichannel time series analysis with digital computer programs, Holden-Day, San Francisco, , , 1967.

RUFF, L. J., Tomographic imaging of the earthquake rupture process, Geophys. Res. Lett., 11, 629-632, 1984.

RUFF, L. J., Tomographic imaging of seismic sources in Seismic Tomography (edited by G. Nolet), D.Reidel Publishing Company, , , 1987.

SPUDICH, P. and L.N. FRAZER, Use of ray theory to calculate high-frequency radiation from earthquake sources having spatially variable rupture velocity and stress drop, Bull. Seismol. Soc. Am., **74**, 2061-2082, 1984.

TAKEO, M., An inversion method to analyze the rupture processes of earthquakes using near-field seismograms, Bull. Seismol. Soc. Am., **77**, 490-513, 1987.

TAKEO, M., Rupture process of the 1980 Izu-Hanto-Toho-Oki earthquake deduced from strong motion seismograms, Bull. Seismol. Soc. Am., **78**, 1074-1091, 1988.

YOMOGIDA, K., Crack-like rupture process observed in near-fault strong motion data, Geophys. Res. Lett., **15**, 1223-1226, 1988.

WIENER, N., The extrapolation, interpolation, and smoothing of stationary time series with engineering applications, M.I.T. Press, Cambridge, Mass, , , 1942.

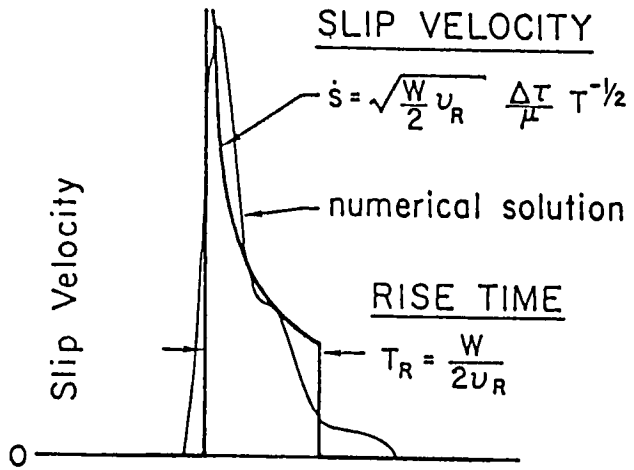
SLIP VELOCITY
$\dot{s} = \sqrt{\frac{W}{2}\upsilon_R}\ \frac{\Delta\tau}{\mu}\ T^{-1/2}$
numerical solution
RISE TIME
$T_R = \frac{W}{2\upsilon_R}$
Slip Velocity
0

(a)

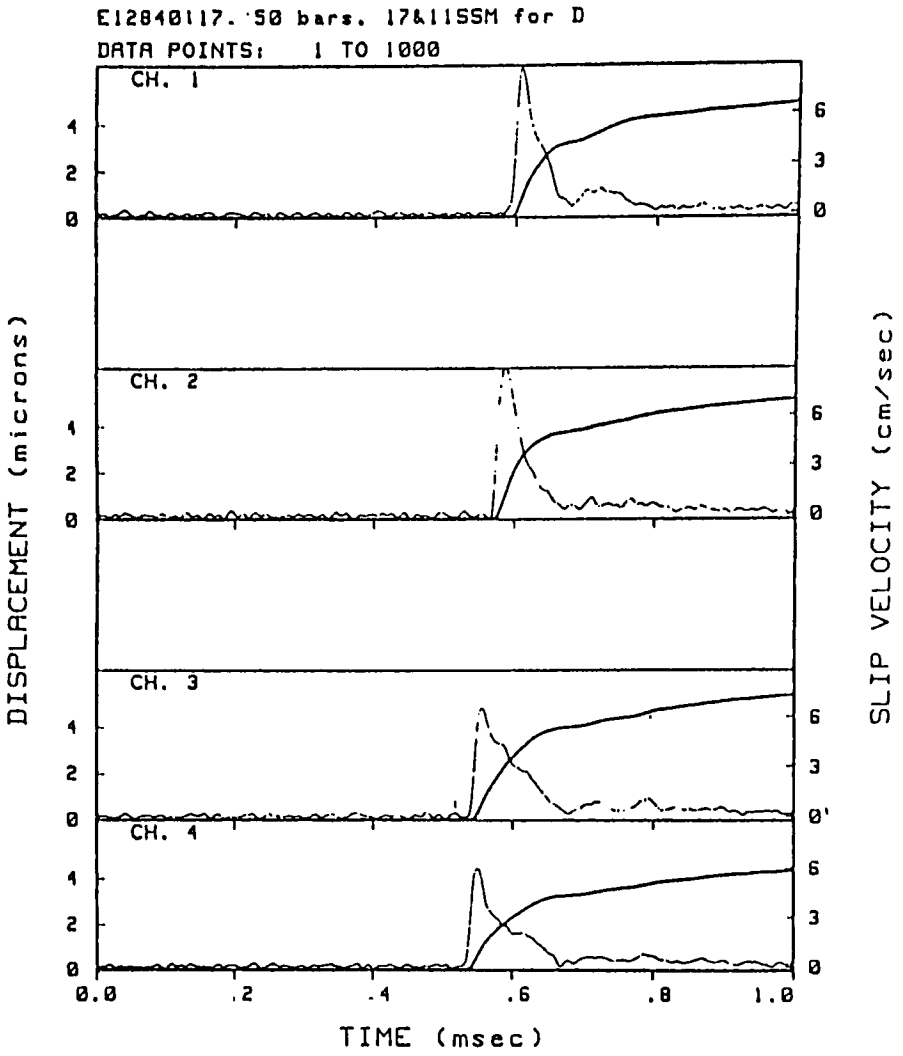
E12840117. 50 bars. 17&11SSM for D
DATA POINTS: 1 TO 1000
CH. 1
CH. 2
CH. 3
CH. 4
DISPLACEMENT (microns)
SLIP VELOCITY (cm/sec)
TIME (msec)
0.0
.2
.4
.6
.8
1.0

(b)

Fig 1

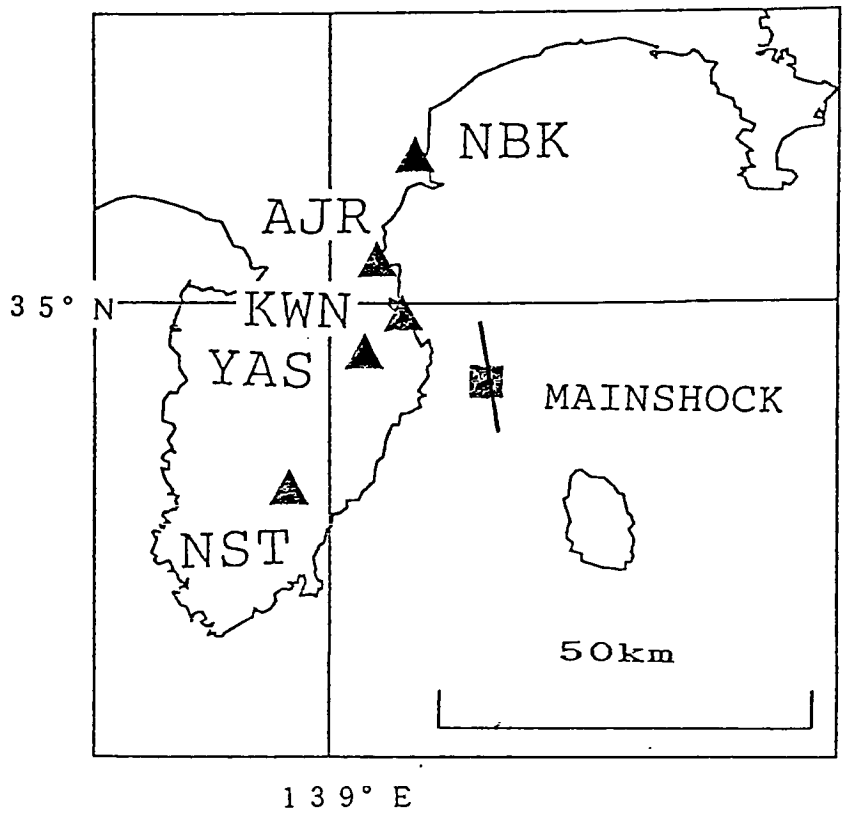

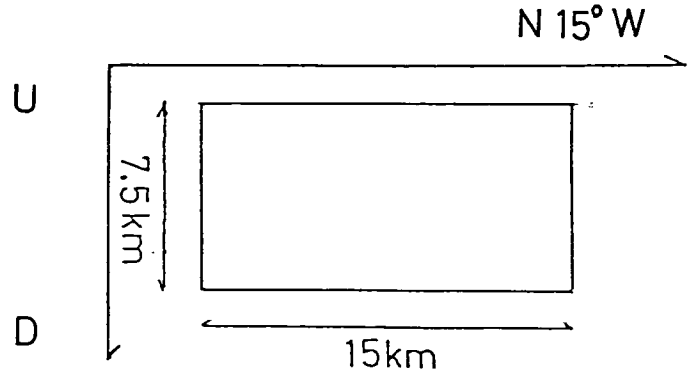

Fig.2

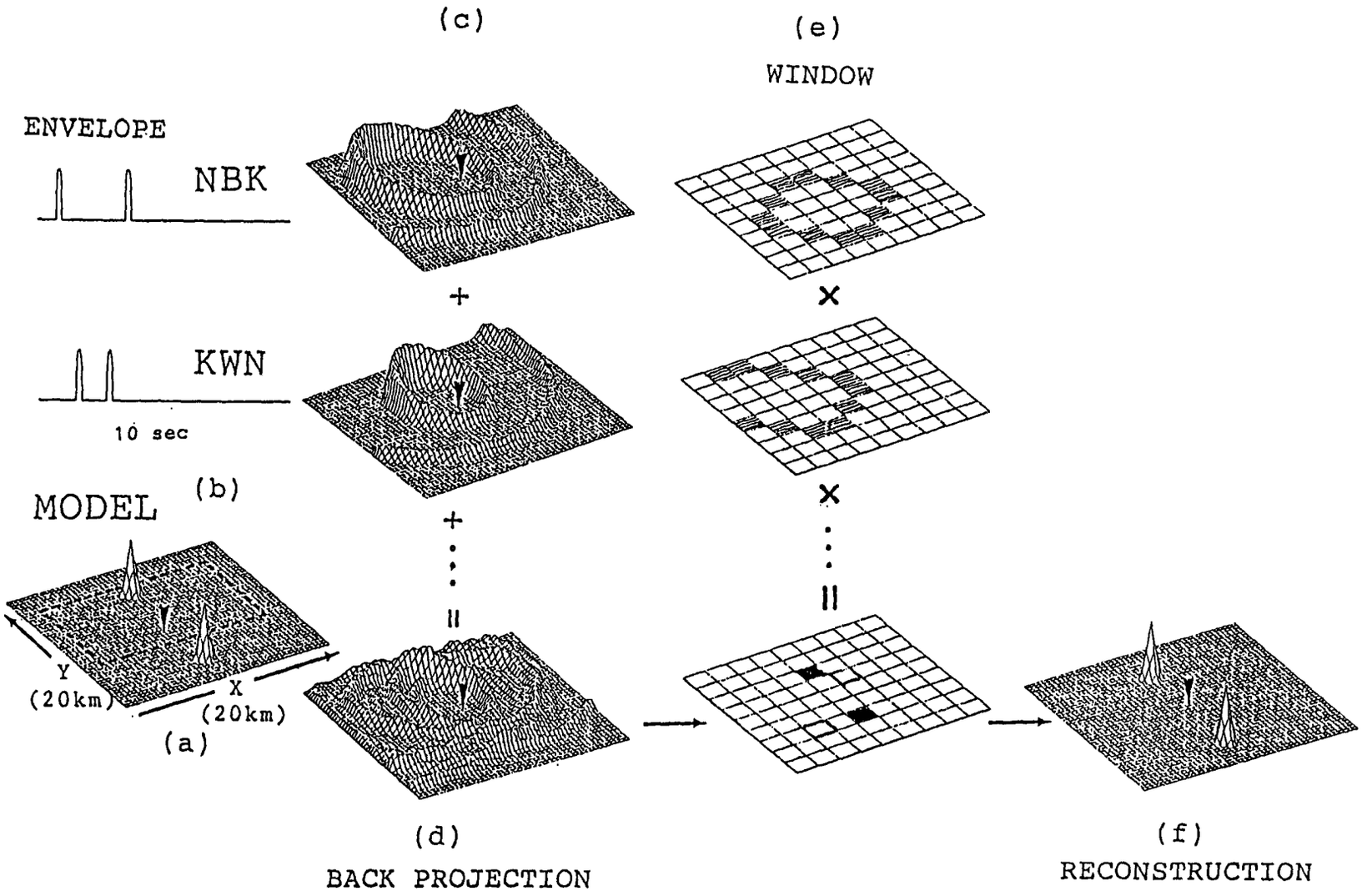
(c)
(e)
WINDOW
ENVELOPE
NBK
KWN
10 sec
MODEL
(b)
Y
(20km)
X
(20km)
(a)
(d)
BACK PROJECTION
(f)
RECONSTRUCTION

Fig.3

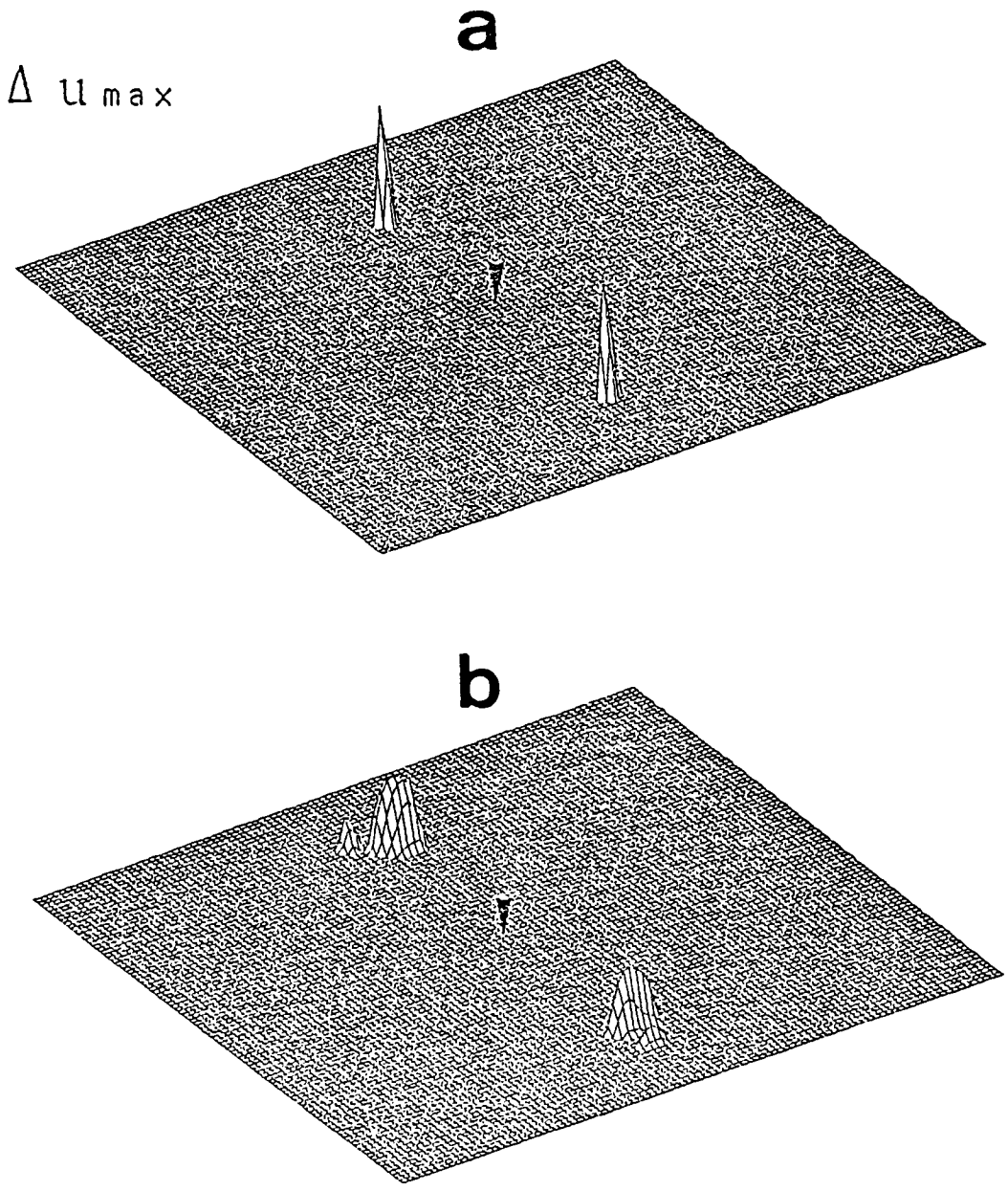

Fig 4

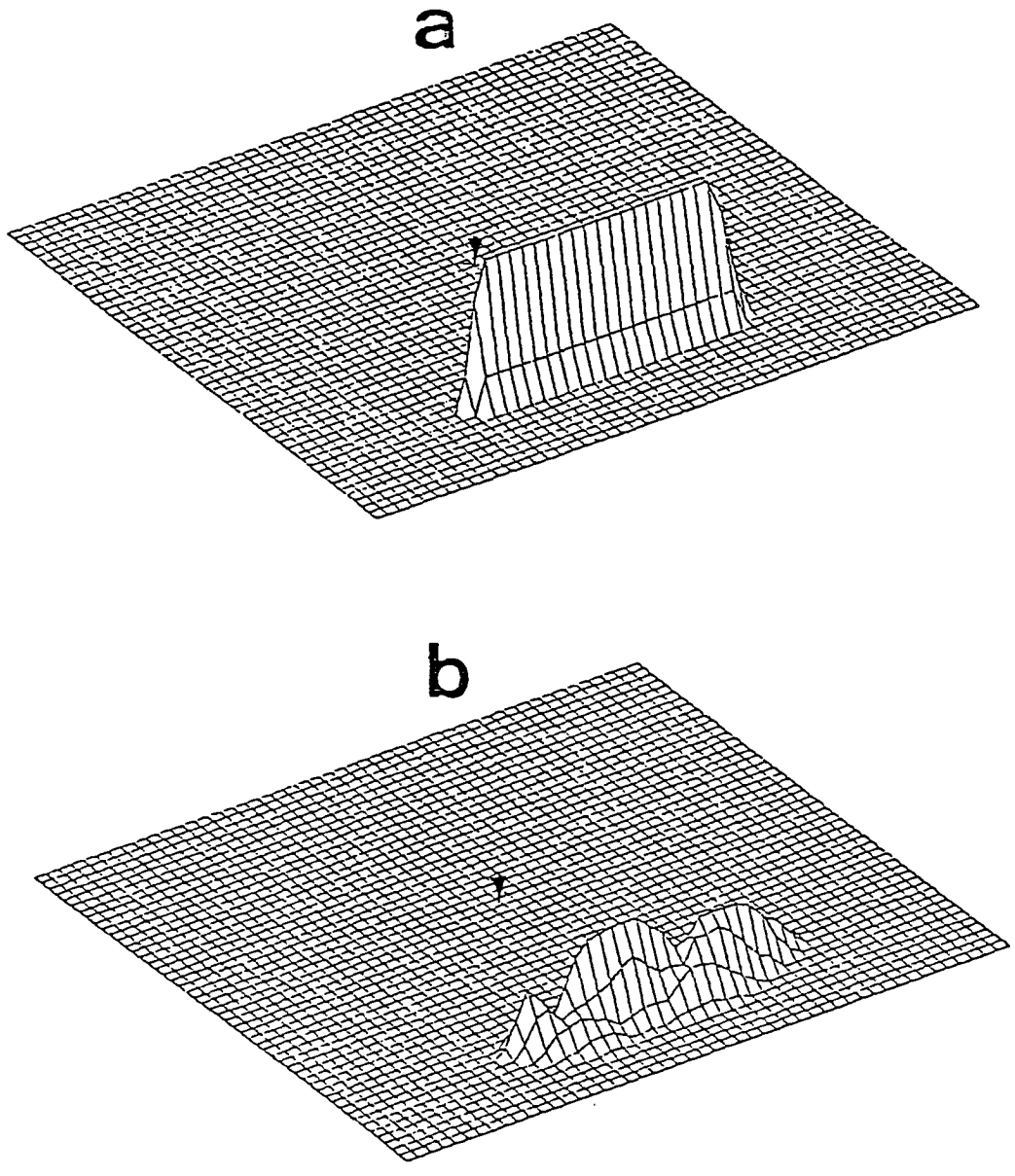

Fig,5

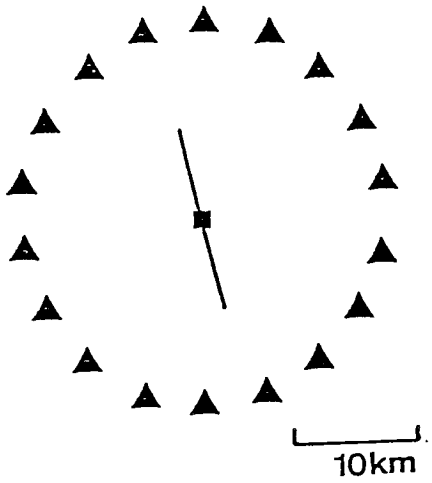

Fig 6(a)

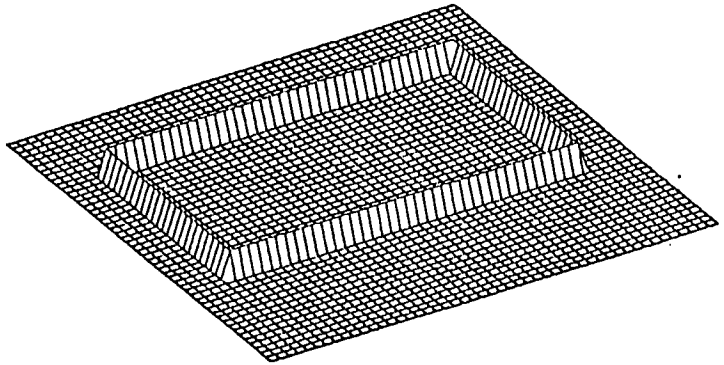

(b)

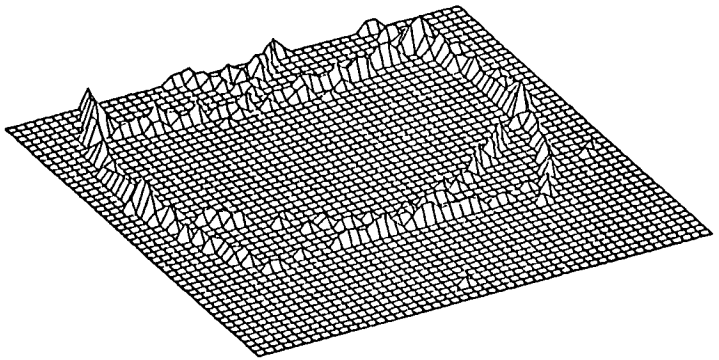

(c)

Fig 6

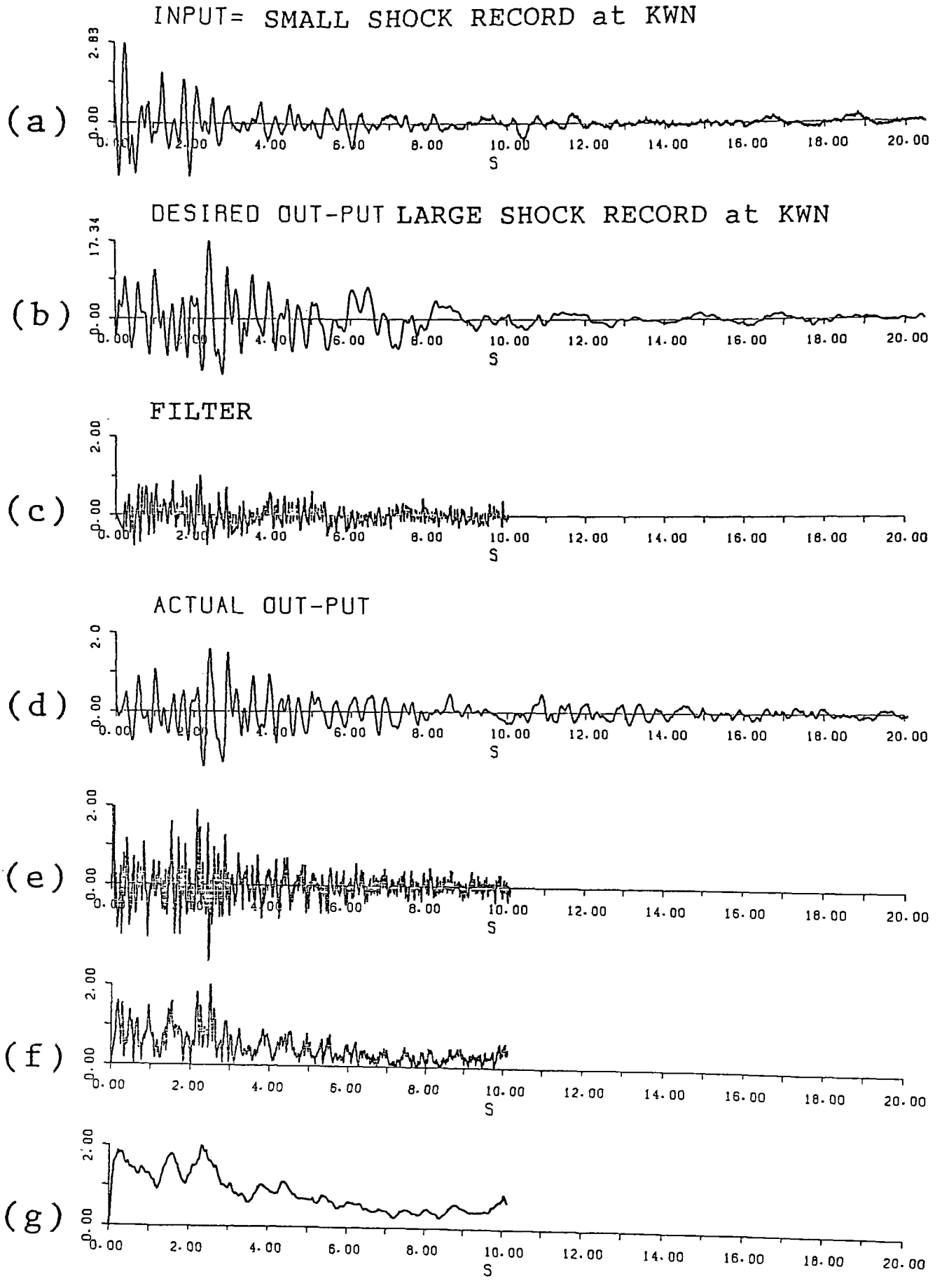
INPUT= SMALL SHOCK RECORD at KWN
(a)
2.83
0.00
0.00
2.00
4.00
6.00
8.00
10.00
12.00
14.00
16.00
18.00
20.00
S
DESIRED OUT-PUT LARGE SHOCK RECORD at KWN
(b)
17.34
0.00
0.00
2.00
4.00
6.00
8.00
10.00
12.00
14.00
16.00
18.00
20.00
S
FILTER
(c)
2.00
0.00
0.00
2.00
4.00
6.00
8.00
10.00
12.00
14.00
16.00
18.00
20.00
S
ACTUAL OUT-PUT
(d)
2.0
0.00
0.00
2.00
4.00
6.00
8.00
10.00
12.00
14.00
16.00
18.00
20.00
S
(e)
2.00
0.00
0.00
2.00
4.00
6.00
8.00
10.00
12.00
14.00
16.00
18.00
20.00
S
(f)
2.00
0.00
0.00
2.00
4.00
6.00
8.00
10.00
12.00
14.00
16.00
18.00
20.00
S
(g)
2.00
0.00
0.00
2.00
4.00
6.00
8.00
10.00
12.00
14.00
16.00
18.00
20.00
S

Fig.7

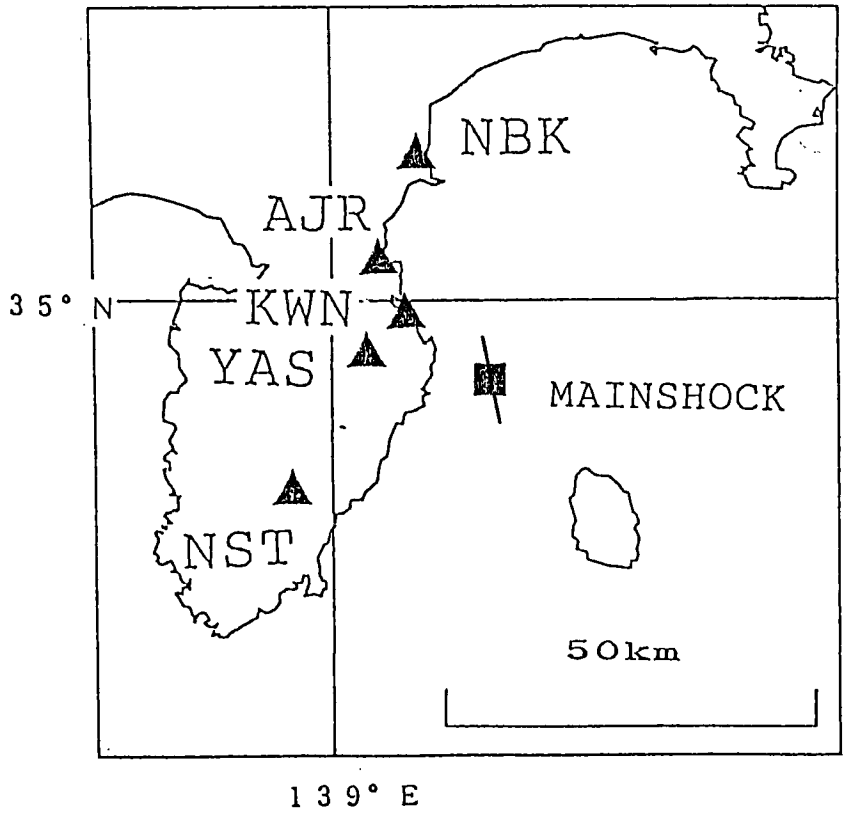

Source Time Function

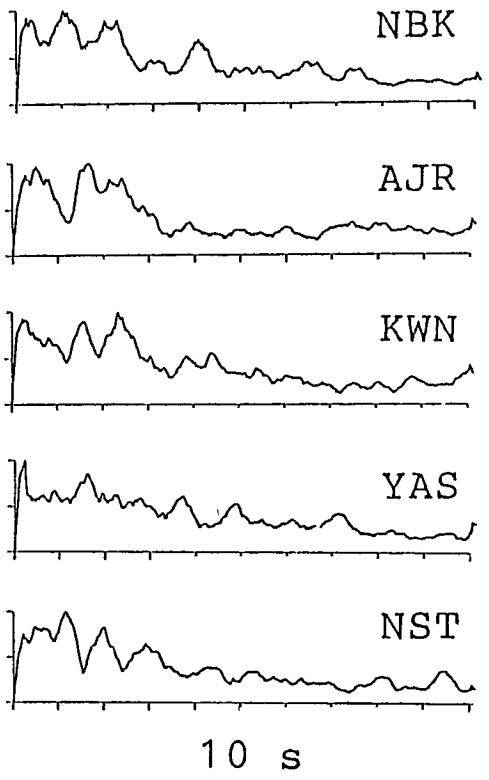

Fig. 8

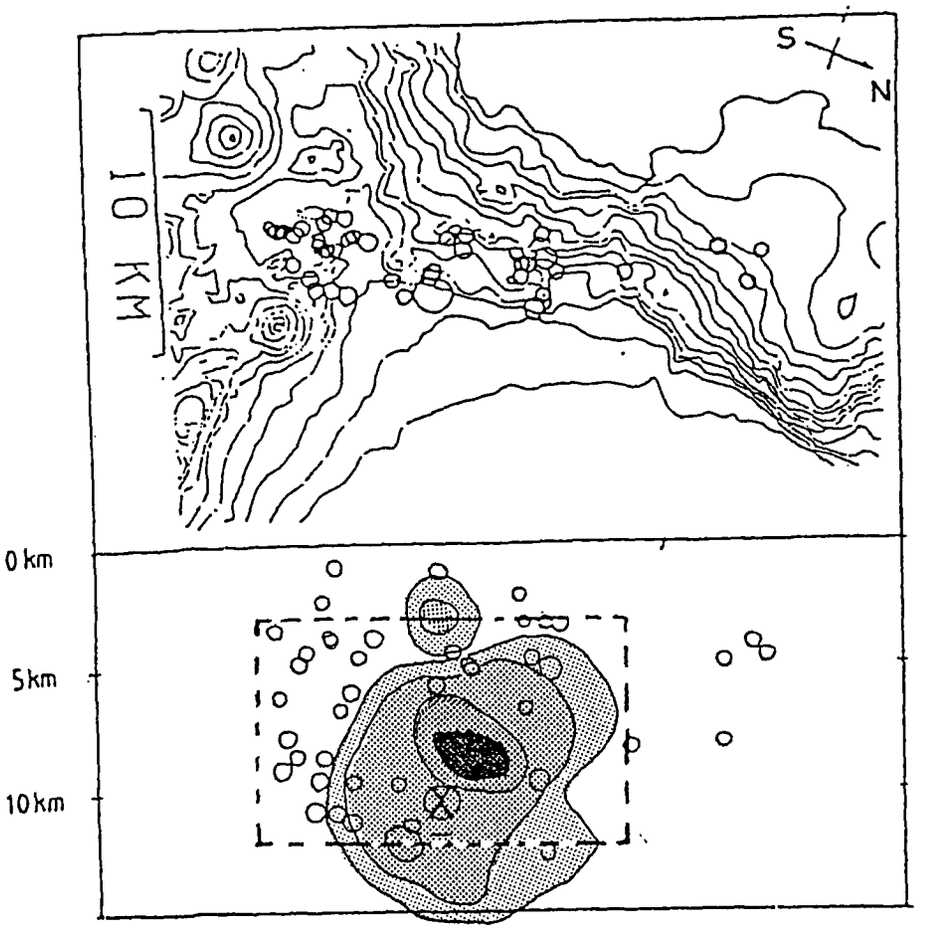

SLIP VELOCITY INTENSITY (%)

20 40 60 80

Fig.9

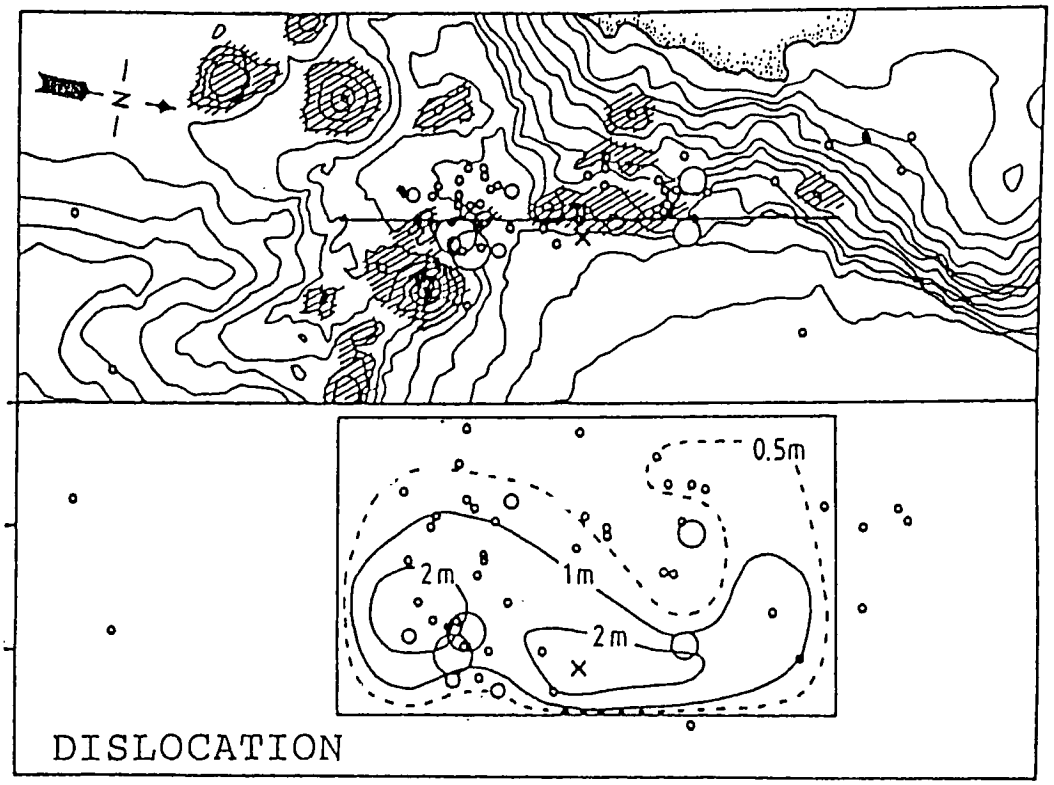

○ 5.0 > M ≥ 4.5 ○ 4.5 > M ≥ 4.0 ○ 4.0 > M ≥ 3.5 ○ 3.5 > M

after Takeo(1988)

(a)

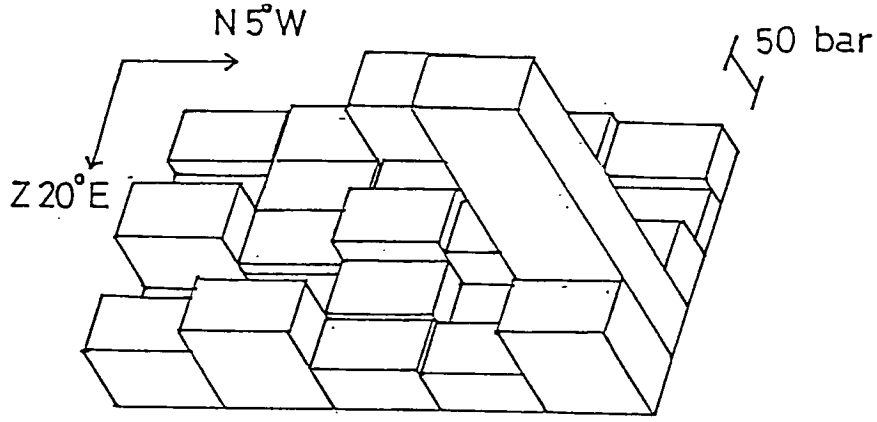

STRESS DROP

after Fukuyama and Irikura(1987)

(b)

Fig,10

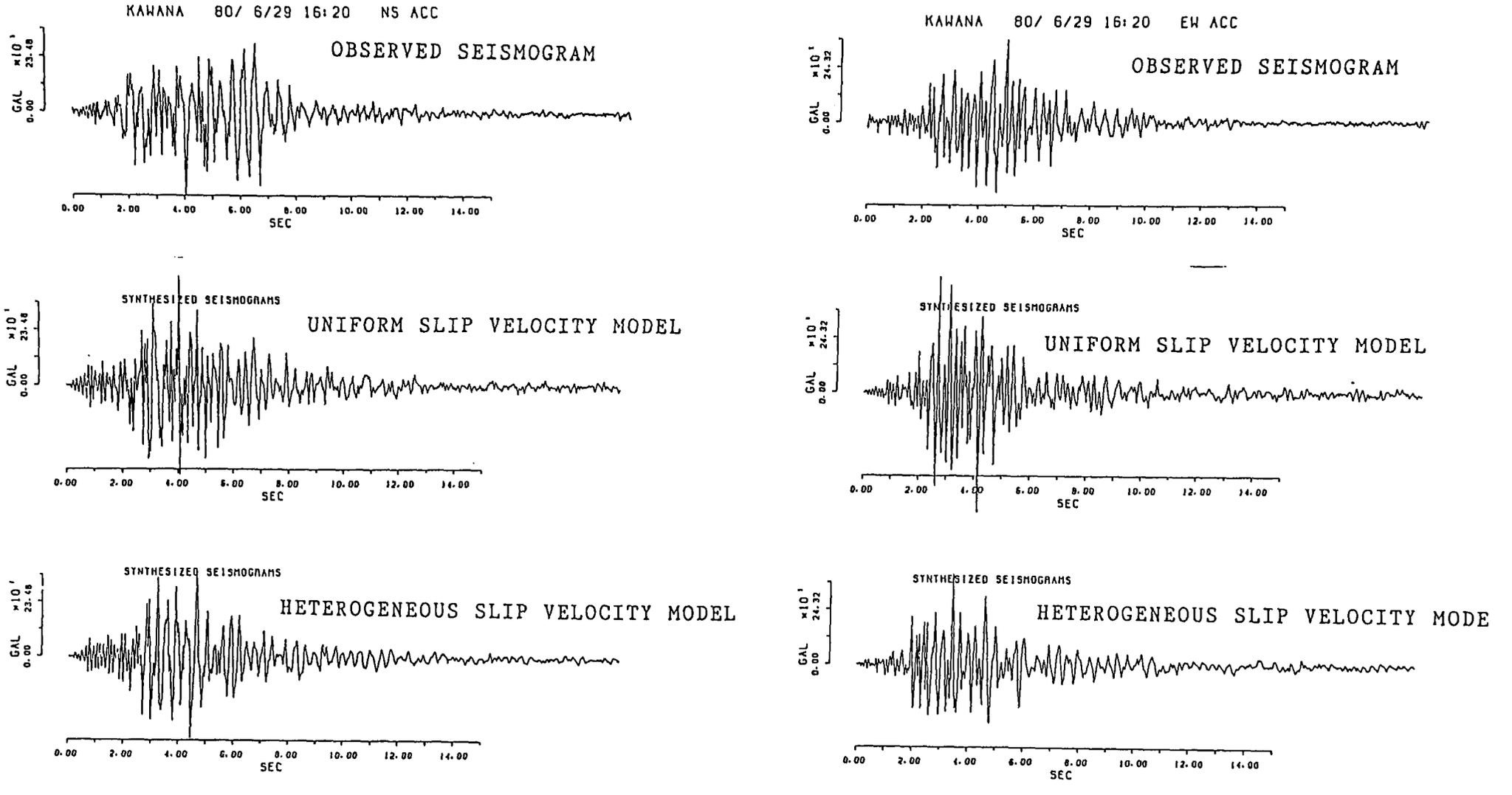
KAWANA 80/ 6/29 16:20 NS ACC
OBSERVED SEISMOGRAM
GAL ×10¹ 23.48 0.00
0.00 2.00 4.00 6.00 8.00 10.00 12.00 14.00
SEC
SYNTHESIZED SEISMOGRAMS
UNIFORM SLIP VELOCITY MODEL
GAL ×10¹ 23.48 0.00
0.00 2.00 4.00 6.00 8.00 10.00 12.00 14.00
SEC
SYNTHESIZED SEISMOGRAMS
HETEROGENEOUS SLIP VELOCITY MODEL
GAL ×10¹ 23.48 0.00
0.00 2.00 4.00 6.00 8.00 10.00 12.00 14.00
SEC
KAWANA 80/ 6/29 16:20 EW ACC
OBSERVED SEISMOGRAM
GAL ×10¹ 24.32 0.00
0.00 2.00 4.00 6.00 8.00 10.00 12.00 14.00
SEC
SYNTHESIZED SEISMOGRAMS
UNIFORM SLIP VELOCITY MODEL
GAL ×10¹ 24.32 0.00
0.00 2.00 4.00 6.00 8.00 10.00 12.00 14.00
SEC
SYNTHESIZED SEISMOGRAMS
HETEROGENEOUS SLIP VELOCITY MODE
GAL ×10¹ 24.32 0.00
0.00 2.00 4.00 6.00 8.00 10.00 12.00 14.00
SEC

Fig 11

Concluding Remarks

In this study, I determined source characteristics relevant to generate high-frequency (>1Hz) strong ground motions.

The points of my originality in this study are the following: In Chapter 1, I examined the source spectral scaling between events occurring in an earthquake sequence and discussed source spectral models in the high-frequency range.

(1) To separate the source spectra, the propagation-path effects, and the local site effects from the observed spectra, I constructed the simultaneous equations with the unknown parameters such as the source spectra, Q-value and the local site effects. To solve these equations by applying a linear inversion method, I introduced the criterion that the local site effects have a factor of more than 2 due to the free surface amplification.

(2)I introduced two methods to test the applicability of the ω^{-2} model to the source spectra with considering the estimated error from the inversion. The first method is to compare the static stress drop with the dynamic stress drop and the second is to compare the seismic moment and the corner frequency determined from Andrews' automated objective method based on the ω^{-2} model to those from the hand-reading method.

In Chapter 2, I estimated the spatial heterogeneity of faulting (slip velocity intensity = SVI) during a large earthquake using high-frequency seismic waves (>1Hz) with an inversion scheme.

(3) I demonstrated thet the reconstruction of slip velocity on

the fault plane is accomplished by the inverse Radon transform. Here I introduced a direct back-projection method with a windowing procedure for inverting the Radon transform. Our method has the advantage of not requiring a priori assumption of faulting area over the previous inversion studies of seismic source processes.

The present method have given the source processes relevant to high-frequency seismic radiations during large earthquakes through the analyses of spectral source characteristics of events and spatial distributions of faulting. Unfortunately, in this study, the analyses of spectral characteristics and those of spatial characteristics are done by using the seismic records from the different earthquakes. During the (large) earthquake, the spatial distributions of aftershocks and their source characteristics on the fault plane will be relevant to the faulting of the mainshock (e.g. Kuroiso et al.,1984; Sato,1985). Thus, it is important to determine the source spectral scaling during an earthquake sequence and the spatial distribution of faulting.

Throughout this study, improvements of the formulations, discussion and check of results of analyses have been done with Prof. Kojiro Irikura.